Aus dem Mannheimer Institut für Intelligente Systeme in der Medizin (MIISM)
der Medizinischen Fakultät Mannheim
(Gründungsdirektoren: Prof. Neumaier, Prof. Schad, Prof. Stallkamp)

Determining the Influence of Environment
and
Minimizing Residual Roughness
in Laser Corneal Refractive Surgery

Inauguraldissertation
zur Erlangung des des Doctor scientiarum humanarum (Dr. sc. hum.)
der
Medizinischen Fakultät Mannheim
der Ruprecht-Karls-Universität
zu
Heidelberg

vorgelegt von
Shwetabh Verma

aus
Delhi, India
2019

Dekan: Prof. Dr. med. Sergij Goerdt
Referent: Prof. Dr. rer. nat. Jürgen W. Hesser

DEDICATION

This dissertation is lovingly dedicated to...

...my omnipresent God, for giving me the inspiration, strength, will, opportunities and conditions to reach this important milestone of my life!

...To Maa, Smt. Mithilesh Verma; Papa, Sh. Shyam Raghubir Verma and

Dii, Niharika Verma. This work is much more a result of your hard work and sacrifices than mine. Your blessings, encouragement, support and constant love have sustained me throughout my life!

...To my loving wife, and partner for life Shalini Kapoor Verma. We both share this achievement, like we share our beautiful life. I Love you!

....To my mentor, friend, guide and Spanish family member, Samuel Arba Mosquera. I could have not done this without you by my side supporting and guiding me. You inspire me...and you rock!

I am grateful for the countless and showering blessings of my teachers, elders and loved ones; I hope to improve each moment of my life to deserve them!

ॐ शिव शिव शिव
उठ बांध कमर क्या डरता है
फिर देख खुदा क्या करता है ।

- श्री राणा खरैती लाल (आपके लिए)

TABLE OF CONTENTS

1   INTRODUCTION

1.1   General Introduction to the topic

The development of science and technology in the field of eye surgery has been rewarding. Laser vision correction procedures have seen several advancements in past decades, either due to the improvements in the clinical techniques being utilized or due to the technical advancements in the Laser systems. Modern Laser systems are much more sophisticated and offer sub-micron precision to successfully treat higher order aberrations by etching complex shapes on the cornea.

Achieving accurate clinical outcomes and reducing the likelihood of a retreatment procedure are major goals of refractive surgery. The credit of the ongoing growth in this field also partly goes to the patient expectation in today's modern age of connectivity, where the patients educate themselves well regarding the risks and benefits of any medical procedure. The patients nowadays demand new and more sophisticated therapeutic strategies with high success rates and predictable outcomes, particularly in Laser corneal refractive surgery, to maximize their visual performance.

Despite being a worldwide accepted surgery procedure with predicable and safe outcomes, it is not a risk free technique, with existing open challenges. Topics like centration reference in refractive procedures, role and preservation of bilateral symmetry in vision, relevance of laser system calibration, importance of aspheric ablation profiles and customized treatments, are only few of the many research fields that are being extensively pursued by the research community in collaboration with commercial institutions.

The technical performance of the laser systems is very much dependent on their calibration routine. Ablating plastic model corneas not affected by biomechanical or other biological effects, with clinical lasers, allows to directly measure the actual ablation pattern provided by the laser, avoiding the approximations and assumptions used in theoretical models. However, plastic models are not intended to mimic the response of the cornea but rather used to characterize the laser systems. The relationship between calibration material and the cornea, and the underlying mechanism behind the response of the cornea to excimer laser ablation, warrants further research.

Several parameters characterizing the laser beam are critical for an accurate and safe refractive surgery and can influence the laser ablation process as well as its outcome. Minimizing the post ablation roughness of the cornea and the applied laser energy on the cornea, can only benefit in minimizing the risks of the surgery and reducing the post-operative recovery time, potentially also improving the visual quality compared to the state of the art procedures. Another important aspect for consideration in post-operative refractive outcomes, is the epithelial masking that will finish the smoothing process after the corneal ablation.

In the recent years, the application of femto-second lasers in the realm of refractive surgery have paved the way for minimally invasive refractive techniques, however due to the expanse of excimer laser systems and the related clinical procedures vastly

performed throughout the world, the research interests in the application of excimer Laser technology still remains strong. At the light of the existing unresolved issues, it is pertinent and justified to attempt to address them using the scientific method and engineering tools.

1.2   Motivation and Hypothesis of this Thesis

Despite continuous growth in this field of medical application, Laser refractive surgery yet presents unresolved problems and optimization avenues. Being accepted globally, refractive surgery procedures are being performed worldwide. Although, Operation Theater conditions are relatively standardized, local climatic conditions may still affect anatomy and physiology of the cornea tissue of the patients and furthermore influence the working environment of the laser system itself.

Corneal excimer laser ablations result in increases in surface roughness and leads to stromal morphologic changes. Such surface changes are an important factor in any laser refractive correction procedure, where smoother ablated surfaces show more efficient refractive correction, induce less scatter postoperatively, and present a more regular optical surface for a faster healing. Postoperatively seen stromal roughness can be simply expressed as sequences of stromal peaks and troughs. In the natural healing process of the cornea, the epithelium would need to fill up the troughs to the level of the peaks to eliminate roughness and regularize the corneal surface.

These challenges acted as the main motivation for this work. A research work to approach these issues may help reducing the complications and occurrence of adverse events during and after refractive surgery, improving the short term and long term postoperative quality of vision, reduce the time of postoperative recovery, as well as reduce the ratio of retreatments and reoperations.

The starting hypothesis for this thesis is that is possible to quantify the influence of environment conditions on refractive procedures. Furthermore, if the influence of environment conditions could be developed into a feasible mathematical model, ablation strategies and calibration routines could be developed for laser platforms, for efficiently compromising the variations and potentially delivering more predictable results in various geographical conditions and patient demographics.

Furthermore, it is possible to quantify the influence of post-ablation roughness on vision and perception, and optimize refractive procedures for a minimum post-operative roughness. A theoretically modelled optimized laser beam profile and placement strategy to place the laser spots on corneal volume, could be empirically tested for improvements in terms of surface roughness, by ablating material of known and standard ablation properties. These improvements could be developed into new algorithms and engineered in new generations of laser systems.

The intention of this dissertation is to describe in detail the theoretical framework and experimental procedures undertaken to pursue the research goals, and describe and discuss the obtained results and their implications in detail. The results and improvements derived out of this work can be directly applied to the laser systems for corneal refractive surgery.

1.3 Laser Refractive Surgery

For a patients suffering from refractive errors, such as nearsightedness (myopia), farsightedness (hyperopia[1]), astigmatism or presbyopia[2], refractive surgery is a method for correcting or improving their vision.

For people who are nearsighted, refractive surgery techniques reduce the curvature of the cornea to make it flatter, in order to reduce the focusing power of the eye. The result is that the images that were focused in front of the retina, due to a longer eye or steep corneal curvature, are pushed closer to or directly onto the retina following surgery. Similarly, for farsighted people refractive surgery procedures aim to achieve a steeper cornea to increase the eye's focusing power so that the images that are focused beyond the retina, due to a short eye or flat cornea, are pulled closer to or directly onto the retina after surgery. Refractive surgery techniques can also selectively reshape portions of an irregular cornea in order to make it smooth and symmetrical, correcting astigmatism.

With the introduction of the laser technologies[3,4] for refractive surgery[5], the change of the corneal curvature to compensate in a controlled manner for refractive errors of the eye[6] is more accurate than ever. Standard ablation profiles based on the removal of convex-concave tissue lenticules with sphero-cylindrical surfaces have proved to be effective in the compensating primary refractive errors. The procedure is nowadays arguably a successful technique, due to its sub micrometric precision and the high predictability and repeatability of corneal ablation[7] accompanied by minimal side effects[8].

1.3.1 Laser Tissue Interactions

When photons strike the surface of the tissue, because of the refractive index change, a portion of the photons are reflected according to the angle of incidence. Photons penetrating the surface are refracted, obeying the law of Snellius, which states that photons entering a medium with a higher refractive index are refracted towards the normal to the surface. In the tissue, the photons may be scattered, changing their direction of flight according to the probability function expressed as the anisotropy factor, or absorbed, exciting the absorbing molecule by an electronic transition[9].

The first systematic presentation of the reaction mechanisms of lasers with tissue was given by Boulnois in 1986[10] (*Figure 1*). Another important finding was the "selective photothermolysis" by Anderson and Parish in 1983[11]. It is the damage confined to the specific tissue structures by selection of laser wavelength, regulation of pulse duration, and repetition rate.
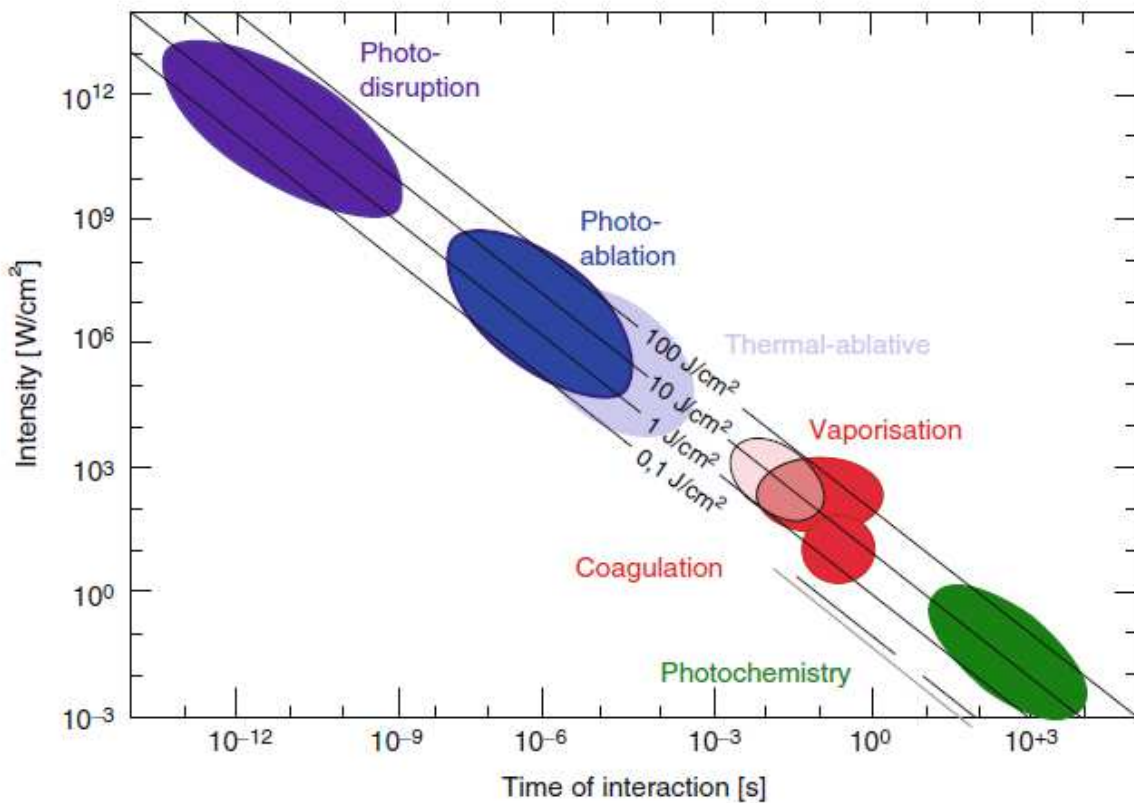
Figure 1. Plot of laser-tissue interaction mechanisms over time of interaction. Modified from Boulnois JL. Photophysical processes in recent medical laser developments: a review. Lasers Med Sci. 1986;1:47–66 [3][9,10]

Photochemical interactions include chemical effects and reactions with macromolecules or tissues induced by exposure to laser radiation of low power densities (upto 50 W/cm^2). This reaction mechanism is used in medical applications like Biostimulation and Photodynamic therapy.

The energy of laser irradiation is transferred into heat due to the absorption of the photons by tissue components, namely DNA/RNA, chromophores, proteins, enzymes, and water. The laser irradiation that is absorbed by the tissue, heats the tissue, leading to an increase in temperature. Thermal diffusion is responsible for heat flow into the tissue. If the exposure time with a laser pulse, is short compared to the diffusion time, this leads to *"thermal confinement"* and the pulse energy is converted into heat in a tissue volume determined by the inverse absorption coefficient, and the spot size. Depending on the increase in temperature, various effects are observed in the tissue, like coagulation (60°C), vaporization (100°C), carbonization (>100°C) and melting (>300°C).

The preconditions for tissue ablation are high absorption and very short laser pulses. Analogous to the *thermal confinement,* one can define a *stress confinement* when tissue is heated up so fast that the pulse duration is shorter than the propagation time, of the stress wave through the heated volume. When the stress wave cannot leave the heated volume during the laser pulse, then it is removed with the ablation of the material and the surrounding tissue is not damaged. This reaction mechanism is applied in popular refractive surgery methods like LASIK. For the photoablation process, a simple model has been derived to calculate the ablation depth called the

"Lambert-Beer" model. According to this model, to ablate tissue, an ablation threshold must be surmounted. Below this threshold, no material is removed and laser energy results in thermal effects only. This is presented in more details in 1.3.5.

Plasma induced ablation involves well-defined removal of tissue by optical breakdown without evidence of thermal or mechanical damage, with laser pulses of very high power densities ($10^{11} - 10^{13}$ W/cm^2) and very short pulse durations (pico-second to femto-second pulses). At even higher power densities, Photodisruption is observed, involving a multi-cause cascade effect starting with optical breakdown followed by shock wave generation, cavitation and jet formation. *Figure 2* presents the relation between the pulse duration and corresponding depth of penetration in biological tissue for different laser types. Areas are marked for normal thermal reactions, thermal confinement (the pulse duration is shorter than the thermal diffusion length or thermal relaxation time) and stress confinement for ultrashort laser pulses[9].
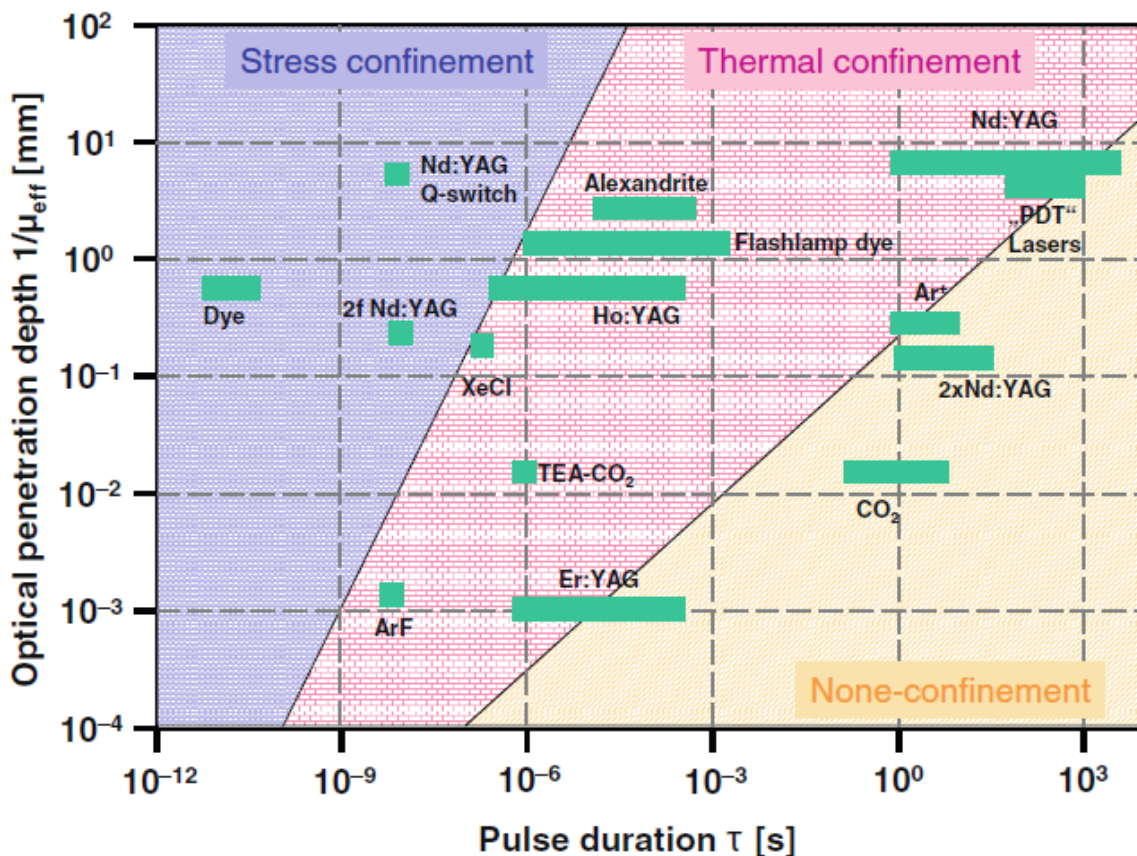
Figure 2. Schematic of laser types, the corresponding tissue reactions, pulse duration, and optical penetration depth[9]

1.3.2 The Origins of Refractive Surgery

Ophthalmologic laser surgery was first conceived when a team of three IBM Corporation workers were trying to estimate new uses for the Excimer laser. They wondered if the laser could make such clean cuts in human or animal tissue like it could already perform in polymer materials. The first tissue they ablated was bone, cartilage and meat from the turkey one of them had for dinner the previous Thanksgiving day[12]. When cutting some patterns on the tissue, they observed that only

the spot focused by the laser was affected, while the surrounding tissue had no evidence of damage.

This story happened in 1981. Two years later, the first excimer lasers for surgical treatments were performing radial keratotomies on human eyes[13]. Late in the 80's Photo-Refractive Keratectomy[14] (PRK) was performed with broad beam lasers, mechanical debridement, small optical zones (5 mm), without transition zones, and the surgery used to be unilateral; around the same time, excimer laser keratomileusis[15] was performed with thick free caps, ablated on the underside of the flap and then sutured in place. In the early 90's, Laser-Assisted in Situ Keratomileusis[16] (LASIK) was developed, by creating a hinged flap; ablating on the stromal surface, where no suture was needed. In the mid 90's the first scanning lasers were used[17], and the ablation zones were increased up to 7 mm, moreover alcohol debridement was slowly replacing mechanical debridement in the surfaces treatments. Late in the 90's laser systems were enhanced by adapting Eye-Tracking technologies[18]. In the early 2000's, Laser-Assisted Sub-Epithelial Keratectomy[19] (LASEK) was introduced by creating epithelial flaps, and the laser technology improved introducing flying spot patterns[20]. Over the years, Laser corneal refractive surgery has become a revolution in ophthalmology, allowing surgeons to correct precisely and safely refractive defects in a stable manner. Until the introduction of laser corneal refractive surgery, these refractive defects could only be corrected by ophthalmic prostheses such as spectacles or contact lenses, or they could be approached by a restricted elite of pioneer surgeons in the form mechanical keratomileusis or intraocular surgery with all the complications and risks that these techniques imply.

Since the introduction of the excimer laser surgery of the cornea by Trokel[13] in 1983, more than 70 million treatments (or 35 million patients) have been successfully performed. As the prevalence of myopic defects in western societies is about 30%[21] and of above 50% in Asian countries, the potential of the surgical techniques reaches more than 1 billion people (without consideration of their economic means). With time, new procedures have been developed, more reliable and for a wider spectrum of cases. These have been assorted by their chronological appearance and briefly explained in the following section.

1.3.3 Different Modalities in Refractive Surgery

Radial keratotomy[22] (RK)

This was the first refractive surgical procedure. It can correct myopia and astigmatism and consists of a series of (radial) incisions on the cornea in a pattern that emulates the spokes of a wheel.

Photorefractive keratectomy[6] (PRK)

This procedure is more advanced. The epithelium is first removed mechanically and the stromal bed is exposed. Subsequently an ablation is made on the stroma in order to correct the eye's ametropia. After the procedure, the epithelium is allowed to regrow naturally.

Phototherapeutic keratectomy[23] (PTK)

The PTK involves removing tissue from the eye, in order to remove any irregularities that may be present. The difference with any other treatment is that its aim is to ablate the same depth at every point of the treatment zone, making a flat treatment.

LASER in situ Keratomileusis[24] (LASIK)

The goal of this procedure is the same as PRK, which is to correct any ametropia that may be present in the eye, although the method is differently applied as the aim of this procedure is to retain the epithelium as undamaged as possible. For this procedure, a flap is mechanically created and the stroma is exposed; the laser ablation is applied directly on the stroma. After the procedure, the flap is repositioned and allowed to heal naturally.

Transepithelial PRK[25] (TransPRK)

This procedure is basically the combination of a PTK and a PRK. The epithelium is first removed by a PTK treatment and then the PRK is performed. This procedure allows the surgeon to handle the cornea solely with the laser, without any major mechanical actions involved. This feature renders TransPRK procedures their industry jargon of "No-Touch technology".

Subepithelial keratectomy[19] (LASEK)

This procedure is born from the LASIK technology, but instead of creating a stromal flap, only an epithelium flap is taken off using an alcoholic solution. The difference to the PRK procedures is that the epithelial flap is put back on the eye after the stromal ablation for naturally healing, instead of allowing a new epithelial layer to naturally regrow as featured in PRK. This procedure might be suitable for people who have a thin cornea, where a LASIK procedure might be too risky.

Femtosecond assisted LASIK[26] (FemtoLASIK)

The only difference between this procedure and regular LASIK is the technique for making the corneal flap. Instead of applying mechanical ways, the corneal flap is made with a femtosecond laser. This feature renders FemtoLASIK procedures their industry jargon of "Bladeless technology".

Epipolis LASIK[27] (EpiLASIK)

This procedure is a combination of LASIK and LASEK, the only difference to LASEK is the method of removing the epithelium. Instead of using an alcoholic solution, a blade is used to create the epithelial flap. At the end of the surgery the epithelium is put back on the eye for naturally healing.

SubBowman Keratomileusis[28] (SBK)

This procedure is essentially similar to LASIK, only featuring a thinner flap created right under the Bowman's layer.

Epipolis LASEK[29] (EpiLASEK)

This procedure is essentially similar to EpiLASIK but features application of an alcohol solution to reduce post-operative pain.

Small Incision Lenticule Extraction[30] (SMILE)

A relatively new refractive procedure was developed starting in 2007, when an intrastromal lenticule method was reintroduced as an alternative to LASIK called Femtosecond Lenticule Extraction (FLEx) intended for patients with extreme myopia. Following the implementation of FLEx, ReLEx®SMILE was developed. A ReLEx® SMILE Laser Eye Surgery is a one-step procedure compared to LASIK which is a two-step procedure. During a SMILE procedure, the femtosecond laser is used to cut a small corneal lenticule (precise lens-shaped disc within the cornea) and then it is removed via a small keyhole incision.

1.3.4 Wavefront Aberrations of the eye and their Zernike representation

The optical quality of an eye is significantly determined through its wavefront aberration. The wavefront is defined as the multidimensional surface of the points with equal phase. The difference from each of the points having length units to a wavefront reference surface (typically either a planar wavefront surface or a spherical wavefront surface) determines the wavefront aberration (*Figure 3*).
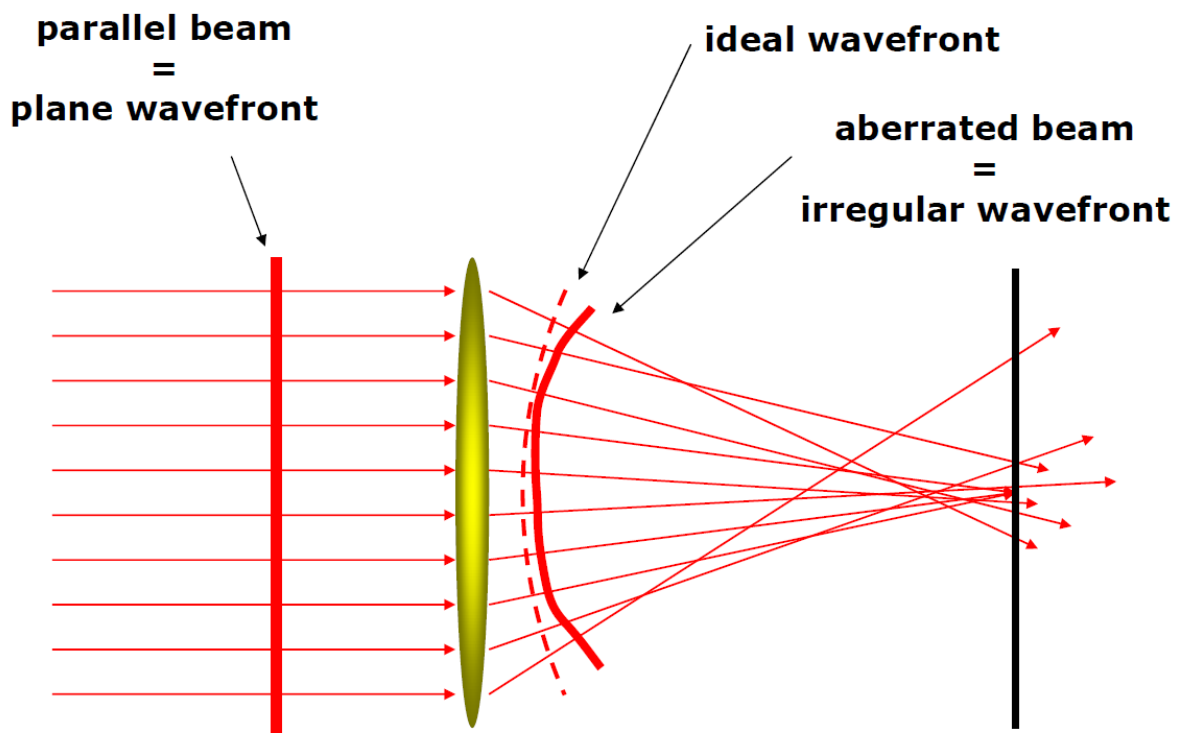
Figure 3. The wavefront aberration. For the ideal wavefront, the light shall converge into a single point after passing through the optical system. However, for an irregular wavefront affected by aberrations a single image point is not observed. Courtesy of Prof. Austin Roorda.

The wavefront aberrations always define an optical error, regardless of whether it is corneal wavefront aberration (wavefront aberrations limited to only the corneal surface obtained by using corneal topography-derived wavefront analyses[31,32]) or ocular wavefront aberration (wavefront aberrations of the complete eye obtained by Scheiner aberroscopes[33], Tscherning aberroscopes[34,35], Hartmann screens[36,37], Slit skiascopic refractometer[38], Hartmann-Shack[39] or other type of wavefront sensors[40,41]). Similarly, for correcting aberrations, one can focus on two aspects, the correction of corneal aberrations exclusively (Corneal wavefront guided treatments), or the correction of total eye aberrations (Ocular wavefront guided treatments).

A wavefront aberration expressed as expansion in series of Zernike polynomials takes the form:

$$WA\left(\rho,\theta\right) = \sum_{n=0}^{\infty} \sum_{m=-n}^{+n} C_n^m Z_n^m\left(\rho,\theta\right)$$

Equation 1

Where WA is the wavefront aberration described in polar coordinates, Z[n,m] are the Zernike polynomials (*Figure 4*) in polar coordinates and C[n,m] are weight coefficients for the Zernike polynomials.
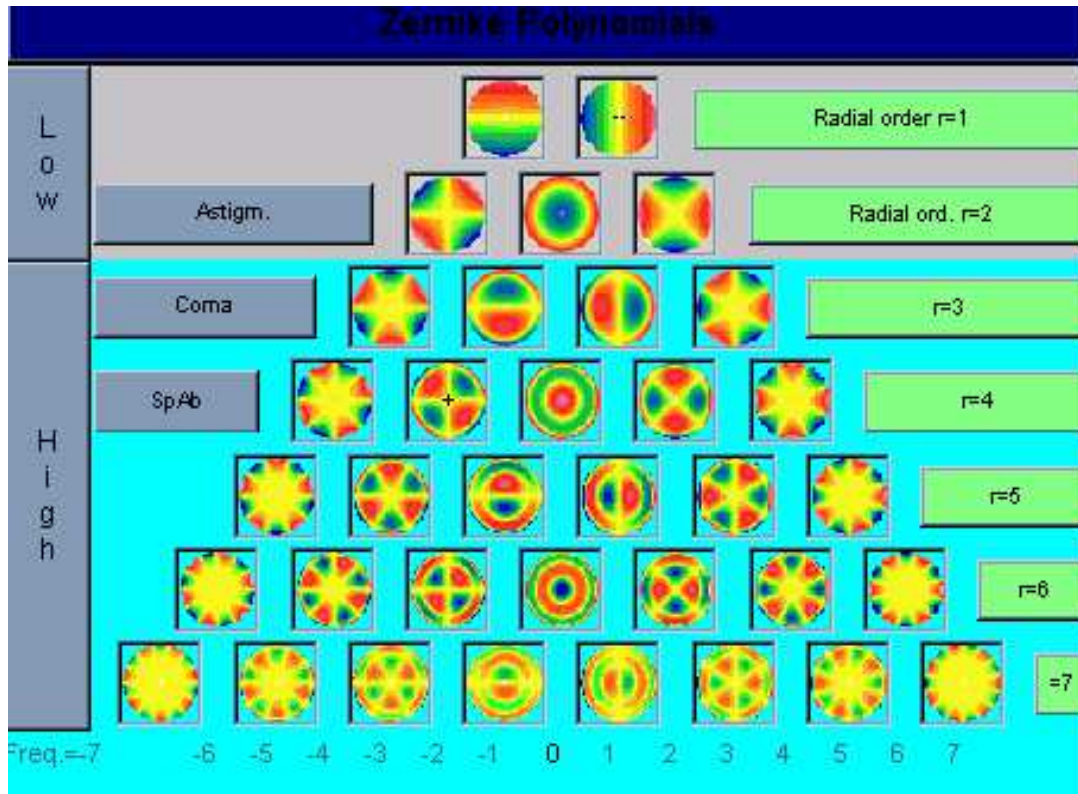
Figure 4.Zernike pyramid showing the Zernike terms up to 7th order and distinguishing the lower and higher order aberrations.

As the C[n,m] are just weight coefficients, they are non-dimensional, and the Z[n,m] are the Zernike polynomials described in units of length. Therefore, the wavefront error is described in units of length. Aberrations can be divided into two groups, the low order, which is best known as the spherical (myopia and hyperopia) and astigmatic defects, and a second group of high-order aberrations. Among the high-order aberrations, the spherical and comatic aberrations have the greatest importance. These optical errors described by the Zernike polynomials and the coefficients of the Optical Society of America (OSA) standard are used to design the wavefront guided treatment plan.

1.3.5 Theoretical Aberration Profiles

Commercially available laser systems used in refractive surgery employ different morphological features, superficial dimensions and contours of the ablations, to induce a defined optical change in a feasible manner[42]. The interaction of excimer laser radiation and corneal tissue is a complex process, involving both ultraviolet photochemistry and rapid thermal decomposition. With the flying-spot laser system, the corneal ablation behavior is mainly governed by the relationship between the per-pulse tissue ablation depth and the fluence (energy per illuminated area) of the incident laser radiation.

Many parameters have to be considered in designing an efficient laser ablation. One is the selection of the appropriate wavelength (193.3±0.8 nm for ArF) with optimum depth of absorption in tissue, which results in a high-energy deposition in a small volume for a speedy and complete ablation. The second parameter is a short pulse

duration to maximize peak power and minimize thermal conductivity to the adjacent tissue (ArF excimer based τ<20 ns).

The radiant exposure is a measure of the density of energy that governs the amount of corneal tissue removed by a single pulse. The depth of a single impact relates to the fluence, and also the thermal load per pulse increases with increasing fluence. Knowing the fluence and details of the energy profile of the beam (size, profile, and symmetry), we can estimate the depth, diameter and volume of the ablation impact[43]. Assuming a super Gaussian beam profile, the following equation applies:

$$I\left(r\right) = I_0 e^{-2\left(r/R_0\right)^{2N}}$$

Equation 2

where I is the radiant exposure at a radial distance r of the axis of the laser beam, I_0 is the peak radiant exposure (at the axis of the laser beam), R_0 is the beam size when the radiant exposure falls to $1/e^2$ its peak value, and N is the super-Gaussian order of the beam profile (where N=1 represents a pure Gaussian beam profile, and N→∞ represents a flat-top beam profile). For human corneal tissue irradiated with nanosecond pulses at 193nm, the ablation threshold takes values of about 40-50 mJ/cm^2 [44,45], and the absorption coefficient is about 3.33-3.99 µm^{-1}. Fisher and Hahn also described a global ablation model that incorporates a dynamically changing tissue absorption coefficient that substantially deviates from a static Lambert- Beer model.

The ablated volume of a single spot is much smaller than the total ablation volume. Due to this, multiple laser pulses are sequentially delivered on to the cornea. Each laser pulse locally ablates a small amount of corneal tissue. The global process is an integral effect of the local process of each individual laser pulse. Thus, the ablation profile must be deconvolved into a series of shot positions, often requiring more than 10,000 shots for the surgery. A higher spot profile gives a higher ablation volume but a lower resolution. On the other hand, a lower spot profile increases the resolution at the cost of increasing the ablation time and the thermal effects due to increased number of laser pulses invested in ablating the same volume. Additionally, using laser pulses with a very low spot profile close to the threshold of the material would mean only imparting thermal effects instead of making any real ablation. All these factors make the energy selection a sensitive criterion. While selecting the optimum energy, a delicate balance needs to be accounted for, between the material thresholds, resolution of the laser pulses, thermal effects of the material and the total ablation time required.

1.3.6 Customized Laser Vision Correction

Customized laser vision ablation was first introduced in 2001, using ocular wavefront aberration data[46]. This novel technique was made possible thanks to Liang and coworkers[39] who could, for the first time, measure ocular high order aberrations (HOAs) in the human eye using a Hartmann Shack aberrometer.

It is still not known precisely whether an "optically perfect eye" after surgery is better than preserving the aberrations that the eye had before surgery. Although the optical quality of the eye can be described in terms of the aberration of its wavefront, healthy individuals with a certain degree of "super vision" have been found to have a measurable degree of aberration in their wavefront[47]. Moreover, it has also been observed that the individuals with smaller wavefront aberration are not always the ones scoring the best visual qualities. Thus, the optical quality of the human eye estimated through the wavefront aberrations does not determine its visual quality in a univocal way. However, the induction of aberrations, such as spherical aberrations and coma, has been related to a loss of visual acuity[48], accommodative deterioration[49], or visual quality degradation.

Awwad et al.[50] defined "customization" as: "The planning of the most optimum ablation pattern for each individual eye based on its clinical diagnosis and visual demands". Individuals with specific wavefront patterns and optical demands deserve individualized treatment solutions. It is often the case that the best approach for planning an ablation is a sophisticated pattern, which can still be simply described in terms of sphere, cylinder, and orientation (axis).

Wavefront correction can be achieved by applying the reverse wavefront. Because a refractive surgery laser system can only remove the tissue rather than add the tissue, the wavefront correction must also consider shifting the ablation profile from negative values to positive values only. Furthermore, the correction is performed by modifying the anterior front surface of the cornea by photoablation. Thus, the change in the refractive index of air (n=1) and the cornea (n=1.376) boundary must be included. Applying these considerations, the ablation at a given point takes the form:

$$Abl(\rho,\theta) = \frac{WA(\rho,\theta) - \min\left[WA(\rho,\theta)\right]}{n_{Cornea} - n_{Air}}$$

Equation 3

Where, Abl(ρ,θ) is the ablation at a given point (in polar coordinates), WA the wave aberration, and n_{Cornea} and n_{Air} the refractive indices of the cornea and the air, respectively.

1.4   State of the Art in refractive surgery

1.4.1   Bilateral symmetry in vision

The role of bilateral symmetry and summation (or fusion) in forming the visual ability in humans, has been pursued since centuries. The binocular visual system in humans possesses a cardinal feature to unify two separate monocular views to render a cyclopean view of the surroundings. In both the eyes, the visual axis is symmetric to the nose-chin axis towards the nasal visual field, representing bilateral symmetry (enantiomorphism). The binocular visual system also makes stereopsis possible[51]. The parallax provided by the different positions of the two eyes in the head, gives humans a precise sense of depth perception[52]. Binocular viewing of a scene creates two slightly different images of the scene. These differences, referred to as binocular disparity, provide information that the brain can use to calculate depth in the visual scene, providing a major means of depth perception[53].

Other important features of binocular vision include utrocular discrimination (the ability to tell which of two eyes has been stimulated by light)[54], eye dominance (the habit of using one eye when aiming something, even if both eyes are open)[55], allelotropia (the averaging of the visual direction of objects viewed by each eye when both eyes are open)[56], binocular fusion or singleness of vision (seeing one object with both eyes despite each eye's having its own image of the object), and binocular rivalry (seeing one eye's image alternating randomly with the other when each eye views images that are so different they cannot be fused)[57]. Arba-Mosquera and Verma[58] analyzed the role of bilateral symmetry in enhancing binocular visual ability in human eyes, and further explored how efficiently bilateral symmetry is preserved in different ocular surgical procedures.

The bilateral symmetry (enantiomorphism) in human eyes with respect to the nose-chin axis enables a much wider horizontal field of view than vertical field of view. Humans have a maximum horizontal field of view of ~190 degrees with two eyes, ~120 degrees of which makes up the binocular field of view flanked by two uniocular fields of ~40 degrees each. Further to this, both eyes show many interrelated symmetries and can influence each other in several ways. Light falling in one eye affects the diameter of the pupils in both eyes. If one eye is open and the other closed, the closed eye follows the accommodation of the opened eye. The state of adaptation of one eye can have a small effect on the state of light adaptation of the other. Li Y. et al.[59] evaluated the symmetry between the right and left eye of 397 subjects in 14 biometric parameters. They found a potentially clinically important inter-ocular symmetry in spherical equivalent, best corrected visual acuity (BCVA), average corneal curvature, Jackson crossed cylinder power of corneal astigmatism (CJ0 and CJ45), intraocular pressure, central corneal thickness, axial length, anterior chamber depth, lens thickness and vitreous chamber depth. However, for keratoconic patients a greater inter-ocular asymmetry in pachymetry and posterior corneal elevation variables has been reported[60,61]. Based on inter-ocular symmetry, many diagnostic methods have been presented to discriminate between normal and keratoconic cornea[62,63,64].

Studies have verified the correlation of aberrations from the left and right eyes indicating the presence of significant bilateral symmetry[65,66]. In addition to the aberrations in the ocular optics, cone directionality (Stiles-Crawford effect) also controls the retinal image quality sampled by the photoreceptor array. Marcos et al.[67]

investigated in twelve subjects the symmetry between the right and left eyes for wavefront aberration (measured using a spatially resolved refractometer) and cone directionality (measured using an imaging reflectometric technique). Although they found that the pattern of aberrations is in general non-symmetric, suggesting that the development of aberrations follows independent paths in many right and left eye pairs, but cone directionality is in most cases mirror-symmetric (with one case of direct symmetry), suggesting some systematic process underlying cone orientation.

Strong inter-ocular disparity detrimentally affects the binocular summation[68,69,70], severely affecting vision, leading to conditions like Amblyopia (for eg. strabismic, anisometropic and form vision deprivation amblyopia)[71,72,73] and Nystagmus (when the visual axes of the two eyes are far apart)[74,75]. All these relationships clearly point to the critical importance of maintaining (and at best improving) the existing bilateral symmetry of eyes, after an ocular surgical procedure. Very few studies in the literature have addressed the issue of analyzing the symmetry of aberrations between eyes after corneal laser refractive surgery. Refractive surgical procedures are mostly performed monocularly. It is significant to evaluate how a monocularly performed refractive procedure influences the inter-ocular symmetry.

Jiménez et al.[68] analyzed the binocular visual function after LASIK. They evaluated visual performance, monocular and binocular contrast sensitivity function in 68 patients (136 eyes). They found that inter-ocular differences above 0.4µm of the Root-Mean-Square (RMS) for a 5-mm analysis diameter, lead to a decrease of more than 20% in binocular summation. They concluded that the binocular function deteriorates more than monocular function after LASIK. This deterioration increases as the inter-ocular differences in aberrations and corneal shape increase. Similar findings were reported by Villa C et al.[76]. Another important aspect in maintaining the bilateral symmetry is the morphology of the LASIK flaps, where LASIK flaps created with a femtosecond laser have shown to preserve the symmetry and regularity in flap morphology with a more regular planar shape in comparison to a meniscus shape in the flaps created with a mechanical microkeratome[77,78]. Arbelaez et al.[79] compared the preoperative and postoperative bilateral symmetry between OD and OS eyes that have undergone femto-LASIK using Aberration-neutral ablation profiles. They concluded that the treatment maintained the global bilateral symmetry, as well as the bilateral symmetry between corresponding Zernike terms contributing to the bilateral summation.

Limited number studies have evaluated the after effect of refractive surgery on bilateral symmetry. Furthermore, for the studies focusing on this topic[79,67],the method to determine whether or not symmetry is maintained consist of comparing individual terms in a variety of ad hoc ways both before and after the refractive surgery, ignoring the fact that retinal image quality for any given individual is based on the sum of all terms. The analysis of bilateral symmetry should be related to the patients' binocular vision status[80]. The role of aberrations has not been evaluated precisely in relation to the visual ability. A patient with a high level of aberrations can have an excellent visual acuity and vice versa, additionally a patient may not have good stereopsis but may show good aberration symmetry. Furthermore, these relationships have been majorly studied monocularly; evaluating them for binocular vision poses new challenges[58].

1.4.2   Choosing the treatment centration in Refractive Surgery

The human eye is an optical system comprising mainly four non coaxial optical elements (anterior and posterior corneal and lens surfaces), an aperture stop (pupil) and an imaging film in the form of a light sensitive tissue layer called the retina, but conforming a robust aplanatic design compensating the spherical aberrations and coma through a non-planar geometry. Each optical element has its own optical (axis containing the center of curvatures of the optical surfaces of the eye) and neural axes (axis of receptors and retinal neurons peaking at the foveola and declining monotonically with increasing eccentricity). Although, the optical surfaces are aligned almost co-axially, the deviations from a perfect optical alignment results in a range of optical and neural axes and their inter relationships. The sharpest vision of a target is realized when it is in line with the fixation target and the fovea of the retina (visual axis). Displacing the pupil or the target object from this axis, results in reducing the optical and visual properties of the system. Arba-Mosquera et al.[81], summarized the optical and neural axes of the eye along with their interrelationships and presented a perspective on the difference between the on and off axis performance of the eye in terms of the optical and neural image quality. These metrics significantly affect the performance and outcomes of popular laser based refractive surgeries[82]. Many axes of the eye have been described with conflicting and confusing definitions, in the history of physiological optics, while a comprehensive and widely used representation has been presented by Thibos et. al.[83] (Figure 5[84]).
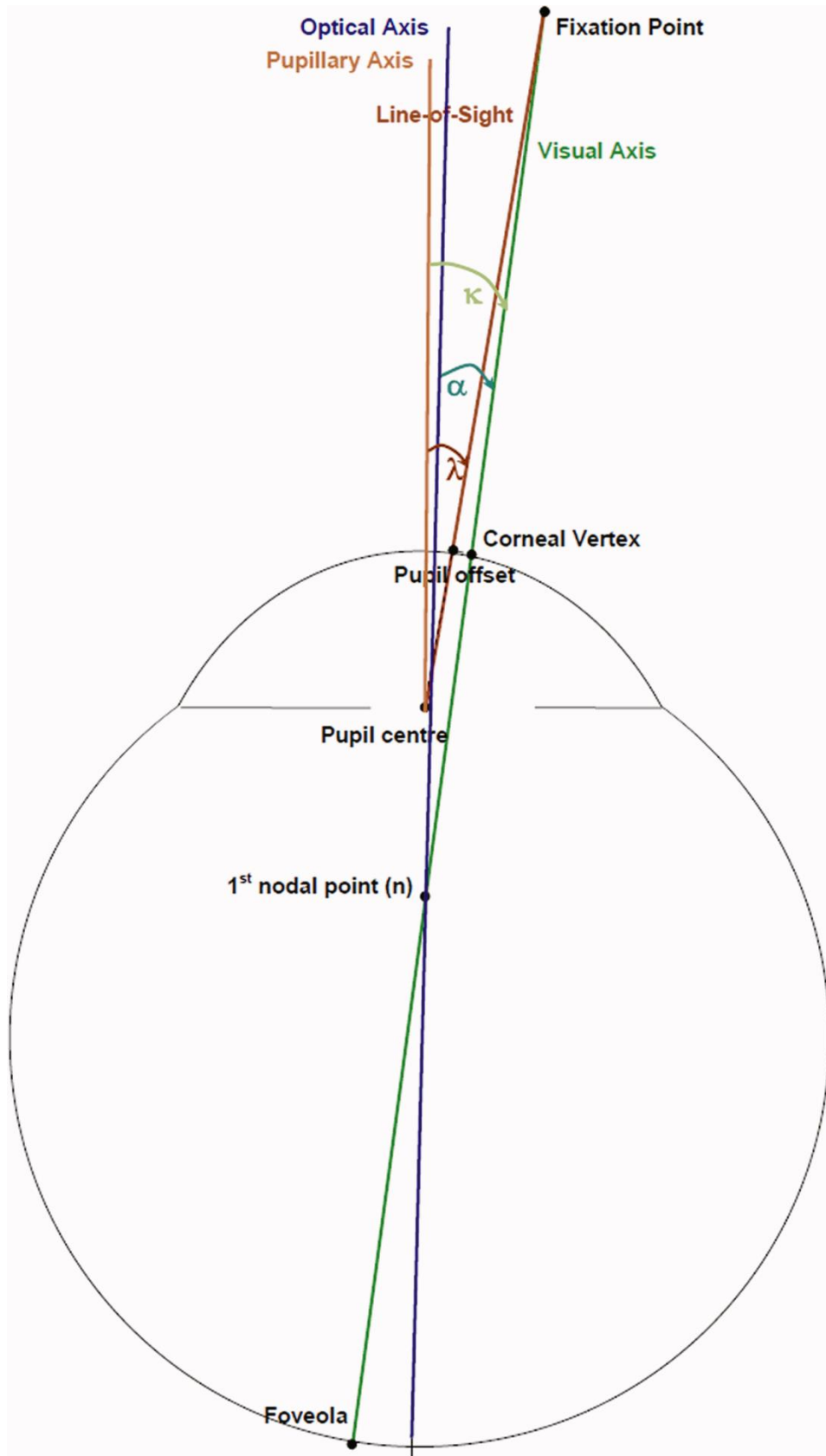
Figure 5. Representative axes of the human eye[84]

The centration of ablation in refractive surgery has been extensively studied. Different centration approaches are applied by commercial laser systems used in refractive surgery (*Table 1*).

S.No.	Company	Device	Technique	Applied	Type
1	Alcon	LadarVision 6000	Semi-Automated based on on-screen identification of CSCLR	Under the laser	The whole ablation is shifted
2	Bausch&Lomb	217 Zyoptix	Manually based CLR (but not truly CS)	Under the laser	The whole ablation is shifted
3	Bausch&Lomb	317 Teneo	Manually based CLR (but not truly CS)	Under the laser	The whole ablation is shifted
4	CustomVis	Pulzar Z1	Fully-Automated based on limbus registration	Under the laser	The whole ablation is shifted
5	iVIS	iRES	Fully-Automated based on iris registration	Under the laser	The whole ablation is shifted
6	KATANA	LaserSoft	Manually based CLR (but not truly CS)	Under the laser	The whole ablation is shifted
7	KERA	IsoBeam	Manually based CLR (but not truly CS)	Under the laser	The whole ablation is shifted
8	LaserSight	AstraScan	Manually based CLR (but not truly CS)	Under the laser	The whole ablation is shifted
9	Nidek	Quest	Manually based CLR (but not truly CS)	Under the laser	The whole ablation is shifted
10	Novatec	LightBlade	Manually based CLR (but not truly CS)	Under the laser	The whole ablation is shifted
11	SCHWIND	ESIRIS	Manually based on Corneal Vertex (numerically taken from diagnosis)	Under the laser	The whole ablation is shifted
12	SCHWIND	AMARIS AMARIS 750S AMARIS 500E AMARIS 1050S	Manually based on Corneal Vertex (numerically taken from diagnosis)	During treatment planning	Only the optical axis is shifted (even for customized treatments), but the whole ablation remains concentric to the pupil boundaries
16	VISX	Star S4 IR	Fully-Automated based on iris registration	Under the laser	Only pupil centration is possible
17	WaveLight	Allegretto Allegretto-Eye-Q EX500 Concept1000	Manually based CLR (but not truly CS), for large offsets or angles (alpha, kappa, lambda) "in between"	Under the laser	The whole ablation is shifted
18	ZEiSS-Meditec	MEL80 MEL90	Manually based CLR (but not truly CS), considering contralateral viewing eye to reduce parallax	Under the laser	The whole ablation is shifted

Table 1. A summary of the centration techniques applied by various commercial laser refractive systems. Here CS is coaxially sighted, CLR is corneal light reflex and CSCLR is coaxially sighted corneal light reflex. It is worth noting that iVIS iRES, KATANA LaserSoft, KERA IsoBeam, LaserSight AstraScan, Nidek Quest, SCHWIND AMARIS,

WaveLight Allegretto and EX500, and ZEiSS-Meditec MEL80 and MEL90 use a video based eye-tracker from the same supplier in slightly different versions.[81]

Controversy remains regarding optimal centration in corneal refractive procedures. The ideal location to maximize visual outcome is yet to be determined. Pupil center considered for a patient who fixates properly defines the Line of Sight in refractive procedures. Pupil Center may be the most extensively used centration method for several reasons. First, the pupil boundaries are the standard references observed by the eye-tracking devices. Moreover, the entrance pupil can be well represented by a circular or oval aperture, similar to the most common ablation areas. Centering on the pupil offers the opportunity to minimize the Optical Zone size (and hence ablation depth and volume). However, Pupil Center is not necessarily the reference for which the patient is actually driving the visual axis during manifest refraction. Moreover, variations in the pupil center in changing light conditions can dramatically affect the centration during ablation. Since the pupil center is a non-stable target, a morphological reference is more advisable in refractive surgery.

De Ortueta et. al.[85] proposed the use of the corneal vertex measured by a videokeratoscope as a morphological reference to center corneal refractive procedures. If the human optical system were truly coaxial, corneal vertex (defined as the point of maximum elevation) would represent the corneal intercept of the optical axis. Ray tracing indicates that the optical axis is the ideal centering reference. The corneal light reflex is formed by the reflection of light from the anterior corneal surface; in other words the virtual image of the light source also called as the first Purkinje Sanson image. Many researchers have postulated that the coaxial light reflex from the cornea lies closer to the corneal intercept of the visual axis than the pupil center and thus recommended the corneal coaxial light reflex as the center in refractive surgery[86]. The entrance pupil is a virtual image formed by the light reflex from the real pupil refracted by the cornea. The corneal light reflex can be considered as non-constant but dependent on the direction of gaze of the eye with respect to the light source. An examiner behind the light source can observe the deviation in corneal light reflex as the direction of gaze changes. Furthermore, due to the parallax between the entrance pupil and the corneal light reflex, the exact projection of the corneal light reflex on to the patient entrance pupil depends on the position of the examiners eye behind the light source. The Coaxially Sighted Corneal Light Reflex[86] will be seen differently depending on surgeon's eye dominance, surgeon's eye balance, or the stereopsis angle of the microscope. In order to avoid these complications other centration approaches are also preferred by some researchers[81].

Hybrid centration approaches have also been advocated, combining the information of acquired from different measurements like three-dimensional corneal with peripheral elevation data[87], or considering pupil center and corneal vertex information simultaneously[88]. Another approach for ablation centration could be to focus on the presumed photoreceptor axis. Since the photoreceptors are aimed at the center of the pupil, light passing through the center of the normal pupil is more effective in simulating the photoreceptors. This argument reinforces the use of pupil centration as reference. However, referencing the photoreceptor axes directly or indirectly has not been studied clinically.

Active eye tracking during the refractive procedure and transformation algorithms aid the transformation of Zernike eye aberration coefficients for scaling, rotation and translation in the pupil[89,90,91]. An eye tracker makes the laser beam follow the eye movements and helps avoid severe decentration, however, studies show that an active eye-tracking system alone cannot ensure good centration[92]. Patient cooperation and fixation are important. Cyclotorsion in the seated and the supine patient has been measured in many studies. Statistical significance of cyclotorsion on the visual outcomes after refractive surgery has been argued in the past[93,94]. The rotational movement of the eye can influence any centration reference to a certain degree. Furthermore, the relationship between the vertex and pupil centration can also vary during rotation. This can affect the ablations designed by converting the axis centration reference in comparison to the reference followed in the diagnostic devices. Assuming that the cyclotorsion angle can be estimated and compensated for with a certain level of uncertainty introduced by the components involved in the measurement, a function was proposed to modify the wavefront error in order to minimize the residual aberration magnitudes due to this uncertainty in cyclotorsion measurement[95]. The results suggested that in a perfectly performing laser system, an "overplanned" treatment will never minimize residual wavefront aberration, independent of the cyclotorsion uncertainty. An "underplanned" treatment calculated will minimize the residual aberration magnitude imposed by the higher order Zernike terms, and will reduce its relative orientation to the original aberration pattern. These results concur with the findings of Shi et al.[96], who developed a stochastic parallel gradient descent (SPGD) - based algorithm to optimize the wavefront-guided correction based on measured scleral contact lens movements for three keratoconus eyes, and found adjustment factors in the same range.

Arba-Mosquera et. al.[97] analyzed the theoretical impact of decentered ablations in inducing coma. They found theoretically, that "aberration-free^TM" profiles should be centered referred to corneal apex, whereas customized treatments should be centered according to the diagnosis reference (since the aberrations maps are described for a reference system in the entrance pupil center). Arba-Mosquera and Verma[98] proposed a simple and inexpensive numerical (nonwavefront-guided) algorithm to recenter the optical zone and to correct the refractive error with minimal tissue removal. Based on the reconstruction of ablation achieved in the first surgical procedure, they calculated a target ablation (by manipulating the achieved Optical Zone) with adequate centration and an Optical Zone sufficient enough to envelope the achieved ablation. The results of their simulations suggest minimal tissue removal with Optical Zone centration and expansion. Enlarging the Optical Zone implied correcting spherical aberrations, whereas inducing centration implied correcting coma.

Defining the optimum center for laser ablation is difficult with many available approaches, each of them claiming to provide good results. The problem comes from the fact that the real cornea is not a rotationally symmetrical volume, and the human eye is an asymmetrical optical system[99]. In theory, even under the consideration of the Stiles-Crawford effect and wide-field vision (as opposed to on axis foveal vision), an ideal optical zone covering the widest entrance pupil is imperative to avoid glare and has shown to result in improved clinical outcomes; this may be as important as the centration reference. The reduction in potential optical side effects of axis misalignment with a wider total treatment zone is at the cost of increased tissue consumption, however, low and moderate corrections usually present with enough tissue to remain within safety limits[81].

1.4.3 Choosing the Appropriate Treatment for a Given Patient

Ocular Wavefront Guided treatments aim at eliminating or reducing the total aberrations of the eye, and have the advantage of being based on objective refraction of the complete optical system of the human eye. The main critics of this approach have argued that aberrations, especially the ones of the crystalline lens, change significantly with accommodation and with age. Hence, the goal "zero aberration" would be inconsistent throughout the day and throughout the years, not to mention the changes in aberration due to the tear film[50].

In many instances, performing Corneal Wavefront Guided treatments offers several unique advantages over ablations based on the total Ocular Wavefront. The ability to translate a topography to a wavefront map, and decompose the latter into individual aberrations with the ability to select and deselect them allows for a slimmer ablation profile, with less risks of postoperative refractive surprises, and less corneal biomechanical impact and subsequent remodeling. The defects are also corrected exactly at their origin – the anterior corneal surface. Additionally, the treatment planning is not limited by the pupil size, as the topographic coverage is normally larger than the pupil size, allowing larger optical zones[50]. However, the repeatability/accuracy of devices when measuring living tissue, introduces some variability. Topography is measured under bright light conditions which might cause pupil constriction and also pupil center shift relative to that in normal photopic levels.

It is vital to evaluate both corneal and internal aberrations (in a non-accommodated state), to determine if corneal and ocular aberrations are being balanced out by one another, and whether a particular type of aberration is better to be removed or to be left as is. Aberration Neutral (aspheric) or Wavefront Optimized approach aims at leaving the eye as it was before the treatment, in terms of Higher Order Aberrations. These have the advantage of saving tissue and time, and due to their relative simplicity, offer very high predictability[1].

Wavefront customized treatments can only be successful if the pre-existing aberrations are greater than the repeatability and the biological noise. These are not always the "gold standard", and different treatment methods offer different benefits and have their respective shortcomings. Therefore, the treatment should be tailor made and customized for each individual eye based on its clinical diagnosis and visual demands. Figure 6 showcases a detailed decision tree process, the decision assistant wizard, which helps choose the best treatment modality for a given eye or patient, and which has been published using the SCHWIND AMARIS laser[100]. While the general principles of this decision tree-based planning can be applied to any other laser platform offering aspheric and Wavefront Guided profiles, some specific aspects concerning both diagnosis and treatments may depend on other manufacturers' specifications.

The decision process starts by estimating the global optical impairment resulting from the measured wave aberrations. This is done by objectively determining the actual clinical relevance of single terms in a Zernike expansion of the wave aberration. In general, for the same magnitude of aberration, the optical blur produced by high order aberrations increases with increasing radial order and decreases with increasing angular frequencies. Based on this, the dioptric equivalent (DEq) is used. If the global optical blur for both corneal and ocular wave-aberrations are below 0.25DEq for both

eyes, then the aspheric aberration neutral treatment should be applied. If the global optical blur for any corneal or ocular wave-aberrations is between 0.25DEq and 0.50DEq for any eye, the CDVA achieved during the Manifest Refraction tests should be checked. If it is better than 20/20 for both eyes, then the patient should be asked about complaints regarding night vision or, in general, quality of vision. If no complaints are reported, then the treatment to be applied is aspheric aberration neutral treatment[50].
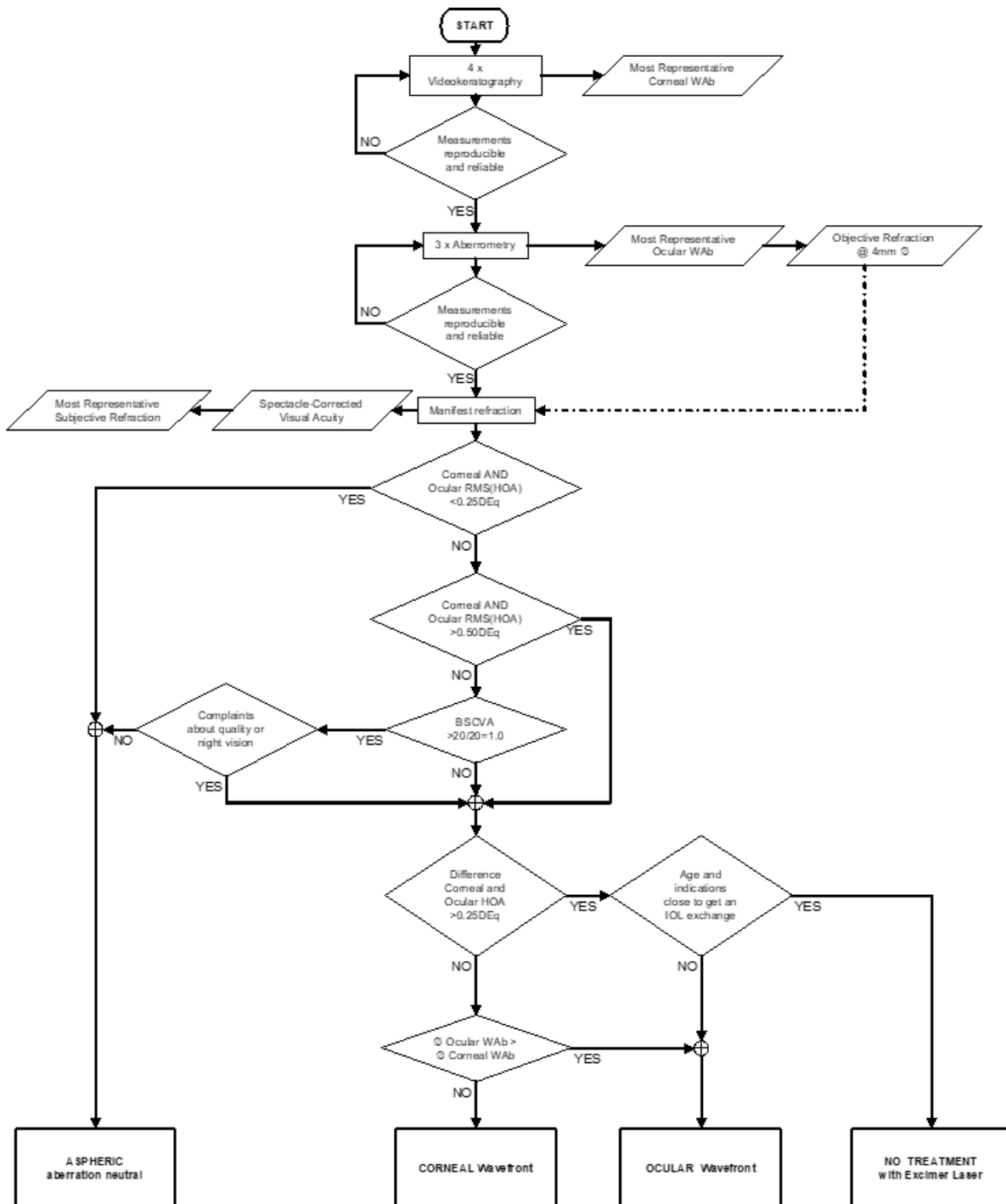

Figure 6. Decision-Tree for selecting the treatment mode (Aspheric aberration neutral, Corneal Wavefront Guided, or Ocular Wavefront Guided)

If the patient reports complaints regarding quality of vision, the CDVA is worse than 20/20 for any eye, or the global optical blur for both corneal and ocular wave-aberrations are above 0.50DEq for both eyes, then corneal and ocular wave-aberrations are to be compared. For this, one shall calculate the differential aberration (Corneal Wavefront aberrations – Ocular Wavefront aberrations, both centred at the line-of-sight) in terms of the Zernike expansion, and estimate the global optical difference. If the global optical difference between corneal and ocular wave-aberrations is below 0.25DEq for both eyes, both corneal and ocular wave-aberrations are considered equivalent. In this case, the treatment to be applied depends on the available diameter of the wavefront maps and the scotopic pupil size. Usually the size of the Ocular Wavefront aberration maps is similar to the size of the scotopic pupils, whereas Corneal Wavefront aberration maps are wider (up to 10 mm in diameter). If the diameter of the Ocular Wavefront or Corneal Wavefront aberration map (the one providing the largest diameter) is at least as large as the scotopic pupil size (in natural dark conditions) reduced in 0.25mm, then Ocular Wavefront Guided or Corneal Wavefront Guided ablation is preferred (the one providing the largest diameter), otherwise aspheric aberration neutral ablation is chosen[50].

If the global optical difference between corneal and ocular wave aberrations is above 0.25DEq for any eye, then the internal wave aberration is relevant. In that case, the treatment to be applied is Ocular Wavefront Guided, unless the patient's age or crystalline lens status would suggest a lens exchange procedure[50].

Considering the above-mentioned selection criteria and normal patient population for laser refractive surgery, aberration neutral and Corneal Wavefront Guided treatments cover the majority of cases, compared to Ocular Wavefront Guided treatments suiting a minority of the patient population[50].

Particularly the treatment of astigmatism in laser based vision correction procedures is commonly done using two different planning strategies; one based on the ocular refraction of the eye and the other based on the shape of the cornea. The two treatment planning strategies originate since the refractive and topographic astigmatism do not always coincide precisely. Their differences can be precisely described by Ocular Residual Astigmatism (ORA), defined as the vectorial difference between corneal astigmatism and the refractive cylinder at the corneal plane expressed in diopters (D) and degrees[101,102]. In normal eyes treated for myopic astigmatism, the ORA typically ranges from 0.73 to 0.81 diopter (D)[101,102]. In one study[101], the ORA exceeded 1.00 D in 34% of eyes; in addition, 7% of eyes treated with manifest refraction alone exceeded the preoperative magnitude of topographic astigmatism. The ORA can be even higher in more irregular corneas such as in cases of keratoconus (1.34 D)[103,104,105].

The influence of ORA on the post-operative status also depends on the goals of the refractive procedure. If the goal is only to eliminate the need of spectacles, laser ablations based only on manifest refraction can suffice. However, ignoring the ORA and sculpting the cornea based only on the manifest refraction has the penalty that the entire ORA remains as the post-operative surgical residual astigmatism, also resulting in induction of spherical aberrations in some cases[101]. This conflict between the two treatment planning strategies for astigmatism correction can be resolved in a balanced manner, following the Vector Planning method, which incorporates both the measured corneal and refractive astigmatism data across the whole ablation profile[101,106,107,108].

1.4.4 Calibration systems in Refractive Surgery

After selecting the appropriate treatment for a patient, and the most suitable reference for centering the laser ablation, the onus of etching the ablation profile on the cornea with high precision and fidelity, lies on the technical solutions build within the laser systems. Therefore, it is imperative to calibrate and maintain the Laser systems used in refractive surgery to repeatedly deliver the same standards of performance over their entire life cycle. This also makes the development of equally precise calibration systems a challenging task for the Laser device manufacturers. A recent extensive review article presented an account of the published literature on the technological advancements in calibration systems, and explored the clinical impact of the error introduced due to the roughness in ablation and its corresponding effect on system calibration[109].

Figure 7 presents an overview of the cycle of calibration normally followed in Laser systems for Laser vision correction. A Laser system sends regular feedback to the calibration device, which measures the deviation with respect to the expected signal. This regular feedback can be laser pulses directed on to the calibration device (for example in case of Energy measurement) at regular intervals, or simply a prompt to use the calibration device and perform a system calibration (for example in case of plastic ablations requiring user interaction). The deviation of the achieved signal from the expected signal acts as calibration data, which is interpreted either objectively or subjectively. The resulting adjustment factor is fed to the Laser system for calibrating the system performance closer to the expectation. This cycle is repeated at different intervals depending on the frequency of the regular feedback, with different methods[109].
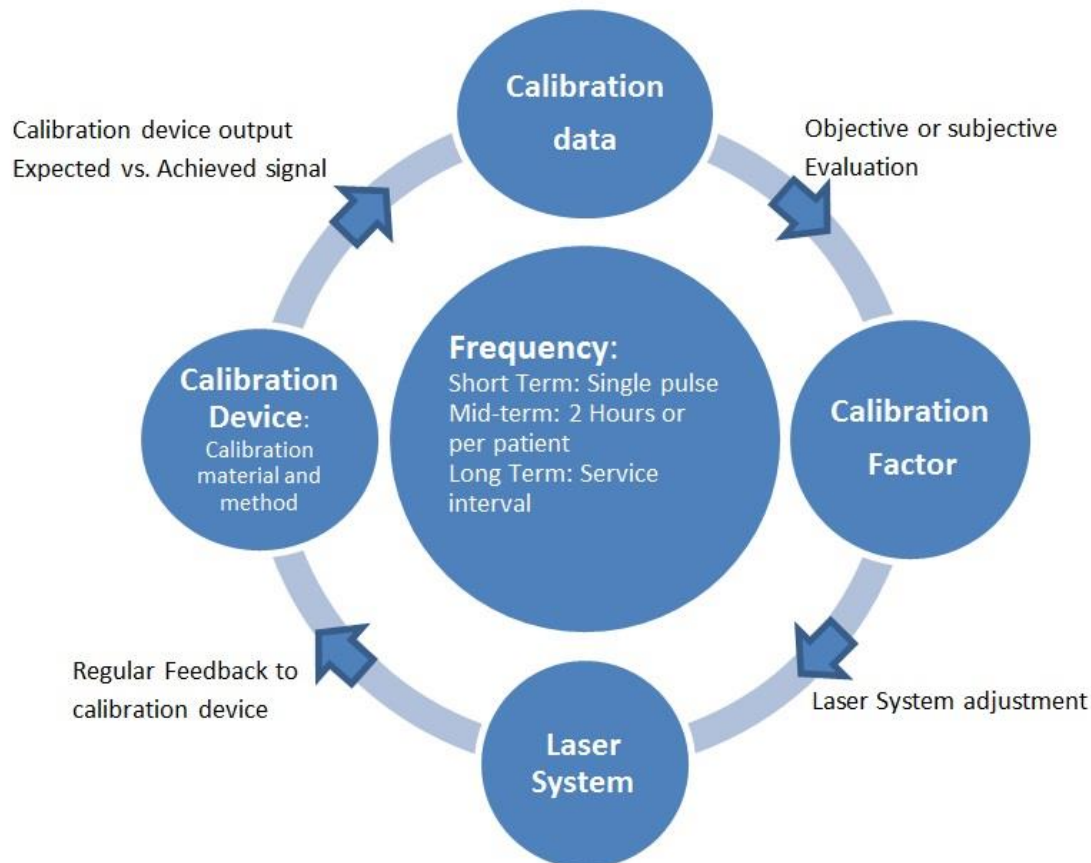
Figure 7. Cycle of calibration followed in Laser systems for Laser vision correction.

A comparison of the different methods to calibrate the commercially available Laser systems is presented in Table 2. Different ablation profiles are employed by different Laser systems available commercially, for example, Bausch and Lomb Laser platforms use a single point ablation profile, Wavelight and ZEiSS meditec platforms use Photo therapeutic keratectomy (PTK) like ablation profiles, while SCHWIND, NIDEK and Kera Laser platforms rely on the refractive ablation profiles. Statistically the standard error in a measurement process is inversely proportional to the square root of the number of measurements. Therefore, as a measure to reduce the error in calibration, multiple ablations and measurements are often designed in calibration tests[109].

Most commercial Laser systems used in refractive surgery follow different calibration steps at different time intervals. These can be broadly classified as short term, mid-term and long term calibration (Table 2). Short term calibration is performed in SCHWIND AMARIS, Wavelight, Nidek and ZEiSS Meditec MEL90 Laser systems where every Laser pulse delivered during the treatment is calibrated to a constant energy. This is followed by a cumulative energy control after every treatment in SCHWIND Laser systems, energy control after every treatment in Wavelight and Nidek Laser systems, and mean energy control after every treatment in MEL90 and Kera Laser systems. Mid-term calibration is done with a fluence test performed every two hours in SCHWIND AMARIS and after every patient in ZEiSS Meditec MEL90 and Kera Laser systems. Wavelight and Nidek Laser systems use daily PMMA ablation tests for mid-term calibration of the systems. Long term calibration is performed with a

PMMA ablation test in SCHWIND AMARIS, ZEiSS Meditec MEL90 and Kera Laser systems at every technical service of the Laser system[109].

During a laser refractive correction procedure, the desired refractive change is translated to a volume that is removed from the cornea using a multitude of laser pulses. For a single point ablation, measuring the achieved ablation depth at a location makes for a technically sound method of calibration. However, for a multi-point ablation, several and varying ablation depths are achieved at different locations in the ablated profile. Therefore, Laser systems could be calibrated based on the maximum ablation depth at a particular location, average ablation depth of all the locations or the average ablation depth within a region of interest on the ablated profile. Additionally, the conversion rates between the ablation depth and refractive power varies across materials and is highly dependent on the surrounding conditions, substantiating the need for a customized complex modelling of the ablation process for an individualized condition[110]. Another important aspect is the interpretation of the calibration data and accordingly the adjustment of the laser systems, by objective or subjective means. Standards of technical training followed in the medical Laser industry is certainly very high, however subjective misinterpretation of the data cannot be ignored. On the other hand, objective calibrations need to incorporate plausibility tests, and protection means against malfunctioning, since they do not have a human interface to validate how valuable the data is (e.g. bad spots in a Hartmann Shack device).

The initial temperature of the ablated material influences the measurement and subsequently the calibration of the Laser systems. This was shown with an experimental argon fluoride excimer Laser with a repetition rate of 1050 Hz, a radiant exposure of 500 mJ/cm², and single pulse energy of 2.1 mJ, which was used for photoablation of PMMA plates.[111] The initial plate temperature varied from 10.1°C to 75.7°C. The initial temperature was measured with an infrared camera and the central ablation depth of a myopic ablation of -9.00 diopters (D) with an optical zone of 6.5 mm was measured by means of a surface profiling system. The ablation depth increased linearly from 73.9 to 96.3 µm within a temperature increase from 10.1°C to 75.7°C (increase rate of 0.32 µm/K). Based on these results and assuming a standard room temperature of 20°C, optimal plate temperature was calculated to be 15°C to 25°C to maintain an ablation within 0.25 D. Therefore, the temperature of PMMA plates for clinical Laser calibration should be controlled ideally within a range of approximately ±5°C, to avoid visually significant refractive error due to calibration error.

The influence of parameters characterizing the laser beam, on the surface roughness of ablation materials and corneal tissue is introduced in detail in the following sections. For a better calibration of the Laser system, a higher fidelity is also needed in measuring the ablated material. Surface roughness plays an important role in accurate measurement of ablation performance. Therefore, along with improvements in calibration systems, smoother ablations shall also be targeted for improving the fidelity and minimizing the measurement error during the calibration process. In a comparative study, Thomas et al. ablated the VISX calibration plastic and porcine cornea with standard -3.00-D, -6.00-D, and -9.00-D settings using four different excimer Lasers.[112] Electron microscopy and Laser interferometry were used for qualitative evaluation of the ablated surfaces. Corneal ablation surface smoothness was graded by ten independent observers. Calibration plastic ablated surfaces were evaluated quantitatively for smoothness by Laser interferometry. In comparing ablation smoothness among various refractive powers (-9.00 D, -6.00 D, and -3.00 D), a trend

was observed that indicated a correlation of higher refractive settings with decreasing surface smoothness. However, this trend was not statistically significant. The quantitative Laser interferometry measurements supported the independent observer ranking of the autonomous flying small spot ablation profile as the smoothest. However, there were differences between the Laser interferometry smoothness rankings and independent observer smoothness rankings.

Few recommendations regarding the laser system calibration can be made from the clinical standpoint. The calibration of the pulse energy is more critical than ablation depth as the energy can be technically manipulated with more accuracy whereas calibration of ablation depth always depends on the calibration material and evaluation method, and further involves conversion factors to estimate the performance on the human cornea. Due to the strong influence of environmental factors like the number of people in the operation room, temperature, humidity, dust, lighting etc., it is recommended to perform system calibration in conditions as close to the final environmental conditions seen in the operating room[109].

Company	Model	Short Term Calibration						Mid Term Calibration						Long Term Calibration					
		Material	Device	Method	Evaluation	Number of Samples	Time Interval	Material	Device	Method	Evaluation	Number of Samples	Time Interval	Material	Device	Method	Evaluation	Number of Samples	Time Interval
Alcon/ Wavelight	EX500	Energy	Energy Meter	Constant Energy	Objective	Every Pulse	Every Treatment	PMMA	Stylus Profilometer	PTK ablation	Subjective	1	Every Day	PMMA	?	?	?	?	?
AMO/VISX	Star S4 IR	?	?	?	?	?	?	Filofocon	HS	Refractive ablation	Objective	1	Every Day	?	?	?	?	?	?
B&L	Teneo	Energy	Energy Meter	Constant Energy	Objective	Every Pulse	Every Treatment	PET	Visual	Single Spot	Subjective	1	Every Patient	?	?	?	?	?	?
Kera	Isobeam	Energy	Energy Meter	Mean Energy	Objective	Every Pulse	Every Treatment	PET	Visual	Refractive ablation	Subjective	1	Every Patient	PMMA	Stylus Profilometer / Lensmeter	Refractive Ablation	Subjective	4	Every Service
Nidek	Quest	?	?	?	?	?	?	PMMA	Lens Meter	Refractive ablation	Subjective	1	Every Day	PMMA	Lens Meter	Refractive ablation	Subjective	?	?
SCHWIND	AMARIS	Energy	Energy Meter	Cumulative Energy	Objective	Every Pulse	Every Treatment	Fluence Foil	Energy Meter	PTK ablation	Objective	2	Every 2 hours	PMMA	Laser Scanning Deflectometer	Refractive Ablation	Objective	12	Every Service
ZEiSS Meditec	MEL90	Energy	Energy Meter	Mean Energy	Objective	Every Pulse	Every Treatment	PET	Visual	PTK ablation	Subjective	1	Every Patient	PMMA	Lensmeter	Refractive Ablation	Objective	1	Every Service

Table 2. Comparison of calibration materials, devices, methods, evaluation methods and frequency of calibration in commercially available Laser systems for Laser vision correction. The question marks in the table represent no data available[109].

1.4.5 Pursuit of ablation smoothness in Refractive Surgery

The human eye is a sophisticated optical system where the state of visual optics defines many important aspects of visual performance, such as acuity and contrast sensitivity. The retinal image formed by the eye is the basis of the human vision, which is later perceived by the brain to complete the vision process. In order to qualitatively and quantitatively analyze the performance of the eye, one must be able to first compute the retinal image for a given source image and a given state of the eye optics[113,114]. The optical performance of any optical system including human eye is often described in terms of the wavefront error at the exit pupil. Standardized methods have been developed to describe these errors over the pupil size, as a sum of a set of weighted Zernike polynomials[115]. These wavefront errors can be used to compute the optical visual point spread function (PSF), and to thereby calculate the retinal image[116].

Attempts have also been made to develop optical quality metrics for the human eye that correlate well with visual performance. Although some of these metrics have proven quite successful at predicting visual acuity[117,118,119], refractive error[120], or subjective blur[121], they have been based upon monochromatic descriptions of the eye's optical quality. Human vision generally involves polychromatic stimuli, which suggests the need for polychromatic measures of retinal image quality; however, the wavefront error of the eye is typically diagnosed with monochromatic stimuli. The complex interactions between monochromatic and chromatic aberrations in forming the retinal image[122,123] has provided motivation to develop computational methods for characterizing the optical quality of the eye that incorporate both types of aberrations. Few general approaches have been proposed in the past for computing the polychromatic image quality of the human eye from a single measure of monochromatic aberrations[124,122,125]. Beyond the objective metrics, subjective responses from the patients are also readily used to assess their visual performance, but ophthalmologic questionnaires and statistical analysis methods also present potential shortcomings[126].

More precise lasers with small laser spots and high repetition rates are now widely used to manipulate the shape of the cornea to correct refractive errors. Corneal remodeling is essentially similar to any other form of micro-machining. The lasers used in micro-machining are normally pulsed excimer lasers, where the duration of the pulses is very short compared to the time period between the pulses. Although pulses contain little energy, given the small beam size, energy density can be nevertheless high. This high energy and the short pulse duration yield a high peak power.

The radiant exposure, measured by the pulse energy density, governs the amount of corneal tissue removed by a single pulse. In excimer laser refractive surgery, this energy density must exceed 40-50 mJ/cm[127]. The depth of the produced ablation crater by a single impact relates to the radiant exposure, also affecting the thermal load per pulse increasing with increasing fluence[128].

Several parameters characterizing the laser beam are critical for an accurate and safe refractive surgery[129,130,131], and can influence the laser ablation process as well as its outcome. These parameters include (but are not limited to) laser wavelength, pulse duration, super Gaussian order, spot diameter, spot truncation, radiant exposure, placement of laser spots achieved with the laser scanners and the debris removal mechanism[132]. It has been theoretically shown that corneal laser surgery could benefit

from smaller spot sizes and higher repetition rates[133]. Furthermore, higher refractive settings correlate with decreasing surface smoothness. These results have been reproduced in polymethylmethacrylate (PMMA) by O'Donnell CB et al.[134], showing an increase of 25 nm roughness per micron of ablation in PMMA. Various measurement techniques have been developed for the measurements of surface roughness[135].

Smoothing agents and optimized energy distribution patterns have been also explored to achieve smoother surfaces after laser ablation. Marco Lombardo et al.[136] examined the impact of smoothing agent (0.25% sodium hyaluronate) on post-operative roughness in porcine corneas subjected to Excimer laser photorefractive keratectomy, by means of atomic force microscopy. Images of the ablated stromal surface showed undulations and granule-like features on the ablated surface of the specimens. The specimens on which the smoothing procedure was performed (root-mean-square [RMS] rough: 0.152±0.014 µm) were more regular (P<0.001) than those on which PRK alone was performed (RMS rough: 0.229±0.018 µm).

Deviations of Lambert-Beer law affect corneal refractive parameters after refractive surgery[137]. Several mathematical models have been proposed in the recent times, particularly for laser tissue interaction in refractive surgery, in the form of modifications in the Lambert-Beer law[138,139,140,141,142,143,144,145,146,147,148,149]. One such model was proposed by Arba-Mosquera and Verma[43], to determine the optimum laser parameters for maximizing the ablation efficiency for different materials (in particular human cornea) at different incidence angles. The model incorporated laser beam characteristics and ablative spot properties, and provided a method to convert energy fluctuations during ablation to equivalent ablation deviations in the cornea.

Arba-Mosquera et al.[150] presented the dual fluence concept for the sequencing of laser shots in corneal ablation, for achieving higher fidelity and avoiding vacancies and roughness of the cornea. Some commercially available laser systems for laser vision correction[151] use the deconvolution method to decompose the ablation volume into pulses[152,153,154]. Previous generations of the SCHWIND AMARIS laser system used a simple heuristic search, without local or global optimizations. Smart Pulse Technology was realized in the SCHWIND platform of lasers during 2014. With Smart Pulse Technology, the simple heuristic search was expanded to a global optimization problem, which finds a balance between minimum residual roughness and maximum ablation precision. SmartSurf[ACE] treatment (SCHWIND eye-tech solutions GmbH) is a combination of TransPRK, implemented using the Smart Pulse Technology, aiming at reducing the residual roughness to enhance the short-term outcomes without compromising stability or long term outcomes[155,156]. The ablation profile with Smart Pulse Technology is described as a 3 dimensional volume with x/y/z-coordinates based on a curved corneal surface where each position has an equidistant in the 3 dimensional room. SmartSurf[ACE] has shown to maintain or slightly improve preoperative corneal asphericity for low to moderate myopic corrections (up to -6.00 D)[157]. Lin et al.[158] investigated the immediate and short-term visual recovery in a large cohort of 2093 myopic eyes (with or without astigmatism) treated with SmartSurf[ACE] procedure. In this large cohort of eyes, immediate and short-term visual recovery was rapid (achieved immediate average UDVA = 20/41±8, improving further at 3-months postoperatively to an average UDVA of 20/21±5), providing functional binocular UDVA immediately after the surgery.

1.5   Challenges in Refractive Surgery

1.5.1   Influence of Environment in Refractive Surgery

Laser-based refractive surgery techniques incorporate sophisticated calculations and compensation of several variable factors involved in the entire process, with the global aim of optimizing surgery outcomes in terms of visual acuity, contrast sensitivity, and night vision. Technological advancements help realize new features in refractive surgery like shorter treatment times, distributed thermal load with optimized spot patterns,[133] and optimized ablation efficiency at non-normal incidence[43,159]. Spatial distribution of laser pulses on the cornea is controlled such that each pulse sequentially ablates a small amount of corneal tissue, collectively etching a very refined pattern calculated and designed to counterbalance the aberrations. Ultraviolet radiation commonly used in laser refractive surgeries is regarded as "cold" radiation. The reason for this consideration is that the thermal relaxation time of the molecules is usually shorter than the thermal denaturation time[160]. However, even these UV laser pulses also impart a certain thermal load to the cornea tissue seen as an increase in ocular surface temperature, observed through simulation models[141], in clinical settings[161,162,163,164] as well as in laboratory settings[165,166], further influenced by the ablation parameters like the ablation frequency and type of treatment (intra-stromal or surface type)[128].

Refractive surgery involves application of laser pulses on the corneal tissue, performed in a temperature and humidity controlled environment. Despite strong climatic controls, the varying degree of corneal hydration is linked to excimer laser corneal ablation rates[167,168]. Luger et al.[169] analyzed the effect of seasonal changes in residual refraction in 5740 consecutive treatments, one year after corneal refractive surgery using the SCHWIND AMARIS laser system. Treatments performed in April, June, August, September, and October showed relative undercorrections of the spherical equivalent (SE) (-0.09D), whereas treatments performed in January, February, and March showed relative overcorrections of the SE (+0.13D). Similarly, treatments performed in spring and summer showed relative undercorrections of the SE (-0.04D), whereas treatments performed in winter showed relative overcorrections of the SE (+0.10D).

Dehydration of cornea begins as soon as the blinking is prevented (e.g. with use of lid speculum), also influencing the ocular surface temperature[170]. Changing corneal hydration affects laser ablation efficiency, which could influence the accuracy of correction. Online optical coherence pachymetry reveals that ambient temperature and humidity levels intraoperatively do not influence the outcome. Yet, basic structural characteristics of patients along with both change in refractive index and corneal shrinkage (because of corneal dehydration) are associated with differences in pachymetry during the procedure[171], affecting postoperative outcomes in a subtle, yet significant manner[172]. In another study, dehydration of the human cornea after insertion of a lid speculum showed corneal thinning with a rate of 0.19μm/s[173].

As demonstrated in bovine eye experiments, significant changes in corneal hydration are realized under different drying conditions and treatment methodologies[174]. Dougherty PJ et al. studied the effect of corneal hydration on the excimer laser ablation rate in bovine eyes and found that the dry component ablation rate (amount of collagen and ground substance removed per pulse) increases as the cornea dries, and

significant dehydration of the cornea before ablation might lead to relative overcorrections of myopia[175].

Laser systems often utilize plastic material ablations like PMMA for calibration[176], due the good correlation between results of laser surface profilometry scans on PMMA and clinical outcomes[177]. But PMMA ablation may also be equally affected by the variations in temperature and humidity[111]. When a PMMA plate is ablated by excimer laser, debris is generated, which may affect homogeneity of the laser beam and energy density, and change the ablation rate. More powerful debris removal systems and smart shot patterns in terms of thermal response have shown to improve the ablation efficiency of excimer lasers on PMMA[132,178]. Dantas et al.[176] evaluated excimer laser fluence after experimentally induced changes in room temperature and relative air humidity and concluded that in a setting with controlled temperature and relative air humidity, subtle changes in environmental factors do not appear to influence laser fluence and efficacy, but acknowledge that the variations seen in PMMA test ablations may not translate completely into clinical changes. Regarding tissue characteristics and specificity, stromal tissue may be more sensitive to environmental changes than PMMA because of the differences in ablation thresholds and the effects of dehydration.

With refractive surgery procedures being performed worldwide, laser systems need to operate in different geographical locations with highly variable climatic characteristics. Although, Operation Theater conditions are relatively standardized, local climatic conditions may still affect anatomy and physiology of the cornea tissue[179,180,181,182,183,184]; and furthermore influence the working environment of the laser system itself. All these factors are highly important for both the laser ablation rates and hence post-ablation outcomes. Previous attempts have analyzed these factors but at a single test location and under controlled climatic conditions that may vary minutely compared to the standard climatic conditions at different geographic locations. Plastic models like PMMA are readily used for calibration of the laser system, but PMMA ablation may also be equally affected by the variations in temperature and humidity[111], intern affecting the calibration and performance of the laser systems.

1.5.2 Roughness in Refractive Surgery

Despite a myriad of technological advances in this field, laser corneal refractive surgery still presents some challenges in achieving higher ablation smoothness and minimizing the applied energy on the cornea. The temporal and spatial distribution of the laser spots (scan sequence) has shown to affect the surface quality and maximum ablation depth of the ablation profile[133]. Smoothness of ablation may also vary with different excimer lasers systems.[185] In a study, ablations were performed on PMMA plates, with four different excimer lasers: VISX-Star, Coherent Schwind Keratom I/II, Chiron Technolas Keracor 117C (Plano Scan), and the Nidek EC-5000, to determine and compare the homogeneity and smoothness of the surface. It was concluded that the laser with Scanning spot technology produced smooth ablations even up to -9.00 D. Ablation smoothness is also influenced by the spot positioning algorithms. Dago et al. performed ablations on PMMA plates using four scanning excimer lasers, two with flying spot technology (Zeiss-Meditec MEL-70, and a Russian-made unit, Microscan) and two Nidek models with scanning slit delivery systems and an expanding iris diaphragm (EC-5000 and EC-5000 CX).[186] The smoothest surface was obtained in samples produced by Zeiss-Meditec MEL-70 unit (RMS=112 +/- 23 nm), followed by the Nidek EC-5000 CX (RMS=153 +/- 12 nm), and the Microscan (RMS=181 +/- 11 nm). It was concluded that scanning excimer lasers based on flying spot technology created smoother ablations on PMMA plates compared to the older Nidek EC-5000 unit.

Vinciguerra et al. used a Nidek Eas-1000 Anterior Eye Segment Analysis System to examine the ablated surface or the interface regularity immediately after PRK and LASIK[187]. At 12 months postoperatively, they found that patients with no postoperative irregularity had a sharply lower incidence of haze and a better refractive outcome compared to patients showing corneal irregularity. Comparatively PRK has shown better short-term visual acuities than LASIK due to the differences in healing of the epithelium[188]. Although improvement in uncorrected visual acuity is more rapid in LASIK, efficacy outcomes in the longer term generally are similar between the two procedures[189]. Performing a final smoothing immediately after PRK or LASIK has been advocated to further improve refractive and optical outcomes[190]. The claims that surface ablation induces roughness needs to be conditioned with the clinical impact on vision since measuring vision is the endpoint. Furthermore, the induced roughness is generally ameliorated by epithelial resurfacing leaving an optically acceptable interface, aiding the postoperative vision.

The roughness in ablation after refractive surgery is related to the transmission of light in the cornea[191]. P. Perez-Merino et al.[192] analyzed the relationship among transmittance, scattering and epithelial surface properties during wound healing after refractive surgery in hens operated using different refractive surgery techniques (LASIK, LASEK, PRK). Their results suggested that higher roughness in the epithelium-stroma interface causes a decrease of transmittance and an increase of scattering. Larger differences between internal and external roughness of epithelium contributes to produce a decrease of transmittance and an increase of scattered light.

The routine technique for evaluating the smoothness of an excimer laser keratectomy has been scanning electron microscopy. However, this method suffers from tissue shrinkage and surface artifacts, and evaluates the surface only in a qualitative manner. In a study, a Zygo microscope was used to quantitatively assess the smoothness of

the excimer laser ablated corneas, without complicated tissue processing. Significant differences were reported between ablated corneas and PMMA blocks, where ablated corneal surfaces were found rougher than the ablated PMMA surfaces[193]. Hauge et al.[194] examined plane parallel plates of PMMA ablated using two excimer lasers, by the means of focimetry, interferometry, and mechanical surface profiling. Interferometry revealed marked irregularity in the surface of negative corrections, which often had a positive "island" at their center. Positive corrections were generally smoother. These findings were supported by the results of mechanical profiling. Contrast sensitivity measurements carried out when observing through ablated lenses whose power had been neutralized with a suitable spectacle lens of opposite sign confirmed that the surface irregularities of the ablated lenses markedly reduced contrast sensitivity over a range of spatial frequencies.

To test the effect of radiant exposure on surface smoothness, Fantes FE et. al.[195] ablated rabbit corneas with the 193 nm argon fluoride excimer laser at nine radiant exposures from 50 to 850 mJ/cm^2. They showed that the uniformity of the surface following laser ablation may play an important role in the rate of epithelial healing and amount and type of stromal scarring. It has been experimentally shown that high levels of surface roughness produced by some laser systems may be sufficient to degrade visual performance under some circumstances[196]. Sean J. McCafferty[197] et al. postulated that the surface changes demonstrated after excimer laser ablation may be indicative of temperature-induced transverse collagen fibril contraction and stress redistribution, or the ablation threshold of the stromal surface may be altered. This phenomenon may be of increased importance using lasers with increased thermal load.

Corneal excimer laser ablations result in increases in surface roughness, surface contraction, and stromal morphologic change. Such surface changes are an important factor in any laser refractive correction procedure, where smoother ablated surfaces show more efficient refractive correction, induce less scatter postoperatively, and present a more regular optical surface for a faster healing[155,156]. Furthermore, postoperatively seen stromal roughness can be simply expressed as sequences of stromal peaks and troughs. In the natural healing process of the cornea, the epithelium would need to fill up the troughs to the level of the peaks to eliminate roughness and regularize the corneal surface (*Figure 8*).
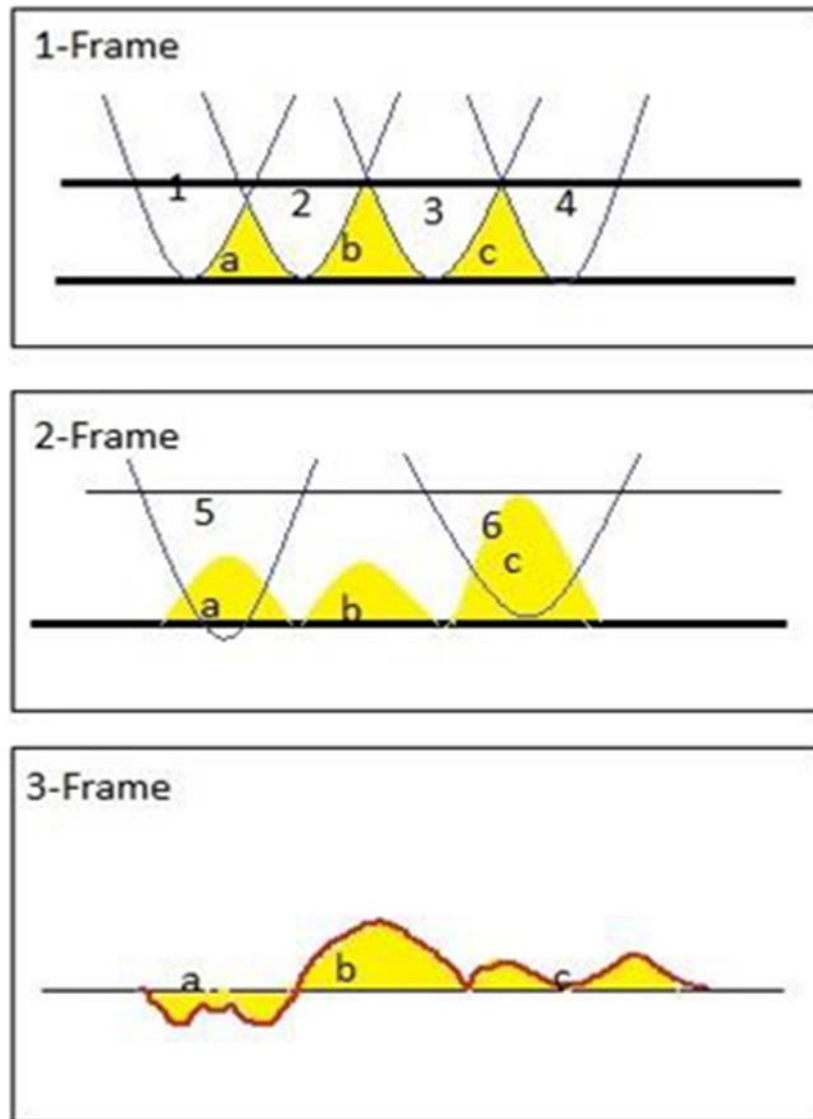
Figure 8. Schematic representation of how the roughness is induced during the pulse-by-pulse ablation process – exaggerated scale

All these researches and existing challenges substantiate the need for achieving a smoother surface in laser ablation for vision correction, for achieving higher fidelity in the post-operative outcomes. Although theoretical models and software exist to qualitatively and quantitatively compute the monochromatic and polychromatic retinal image for given state of the eye optics, to the best of our knowledge, there are no proposed methods applying these models to analyze the impact of residual roughness associated with laser ablation of the cornea in refractive surgery. Furthermore, despite the various modelling approaches comparing the overall predicted performance of laser platforms, an extensive analysis of the impact of individual laser beam characteristics like spot energy, spot diameter, super Gaussian order, truncation radius, spot geometry, spot overlap and lattice geometry on ablation smoothness will add value to the scientific knowledge on the subject. These laser beam characteristics may individually affect the ablation smoothness; for eg. truncating the flanks of the beam profile to avoid thermal loads, preferring flatter beams for a higher ablation volume per laser pulse, preferring smaller spot sizes to increase the resolution for ablating fine structure, preferring lower pulse energy for imparting lesser energy on the

cornea (but being more sensitive to perturbations), or preferring higher pulse energy for achieving stability but at the expense of higher thermal load, may all impact the ablation smoothness either constructively or destructively.

1.5.3 Nomograms in Refractive Surgery

Nomograms have been used from the beginning of refractive surgery. The need for having nomograms is catalysed by variability. In order to achieve optimum results, the laser systems available in the markets can be optimized based on their technical specifications, but the results of refractive surgery also depends on the subtle differences among lasers, surgeons, operation room environment and the patient population and demographics. In order to compensate for these differences and obtain optimum results, different values are treated by the surgeons compared to the actual patient data. These adjustments are determined using Nomograms. Nomograms are designed after precisely analysing a range of patient data based on several factors contributing variability. The precision and success of a nomogram rests on several factors like valid algorithm design, accurate patient data and correct grouping of the data. In addition to this, nomograms must be constantly updated, as lasers, surgeons, and techniques change over time[198].

Feltham and Wolfe[199], retrospectively analyzed the effects of ablation size, refractive errors, patient age, and corneal curvature on the retreatments and found that the older the patient and the larger the refractive error, the greater the risk of not achieving a residual refractive error of ± 0.50 diopter (D) 3 months postoperatively and that corneas that are steeper preoperatively have a greater risk of retreatment.

Most reported nomograms have provided accurate results for myopic spheres; however, for hyperopic spheres and astigmatic outcomes the results are less predictable. Moniz and Fernandes[200] analyzed a nomogram for treating astigmatism with LASIK. Similarly, Alpins and Goggin[201] provided a method to analyze refractive outcomes of astigmatic refractive surgery. The Alpins methodology uses three principal vectors and the various ratios among them provide an aggregate analysis of astigmatic change with parallel indices for spherical correction. However, nomograms are only useful if the effects of their proposed surgical plans can be positively verified. Gailitis[202] compared the outcomes between two different excimer laser platforms using optimized nomograms and reported good results for both platforms, but superior results were obtained with the platform using the more recent nomogram.

A nomogram can be designed based on several factors. One can analogise the factors as variables that are used to design an equation that describes an empirical data precisely. Looking at this process purely mathematically, the more variables that are included in the analysis the better the fit becomes. However, there is no ideal criterion to judge the relevance of the analysed factors on the refractive outcomes. These factors are selected mostly based on scientific studies, common sense and sometimes even a feeling. Although before including other factors, reaching an optimum basis for the refractive surgery design is imperative[198]. Arnalich-Montiel et al.[203] examined four systematic strategies and one intuitive approach for adjusting the ablation sphere in myopic wavefront LASIK with reference to preoperative manifest refraction. Surprisingly, they found that the postoperative manifest refraction spherical equivalent varied less when non-systematic, intuitive adjustments to the ablation sphere were

used. There was a strong trend toward reduced variability in the results in patients with a larger wavefront diameter. The authors concluded that back-calculation to model results with different pre-treatment ablation adjustment strategies might be useful to eliminate unpromising new approaches before clinical trials.

In a retrospectively study[198], seven strategies for adjusting refractive surgery plans with reference to the preoperative manifest refraction were analysed based on the refractive outcomes of 150 consecutive patients who underwent LASIK. In was concluded that all nomograms anticipated minor improvements versus actual observed outcomes without clinically relevant differences among them. The minimal uncertainties in determining the manifest refraction (~0.6 D) are the major limitation to improving the accuracy of refractive surgery nomograms. Therefore, more emphasis shall be placed on the estimation of manifest refraction with higher precision, for improving the treatment planning and accuracy in postoperative outcomes.

1.6   Specific goals of this Thesis

This dissertation deals with multiple purposes and goals which are listed below:

Determining the Influence of Environment

TOPIC A: To analyze the effect of seasonal changes in PMMA Performance using the SCHWIND AMARIS laser system[204]

TOPIC B: To analyze impact of various humidity and temperature settings on excimer laser ablation of PET, PMMA and porcine corneal tissue[205]

Minimizing Residual Roughness

TOPIC C: To analyze the impact of residual roughness after corneal ablation in perception and vision[206,207]

TOPIC D: To outline a rigorous simulation model for simulating shot-by-shot ablation process. Furthermore, to simulate the impact of laser beam characteristics like super Gaussian order, truncation radius, spot geometry, spot overlap and lattice geometry on ablation smoothness[43,208,209,210].

TOPIC E: To test the impact of laser beam truncation, dithering, and jitter on residual roughness after PMMA ablations, using a close-to-Gaussian beam profile.[211]

1.7   Thesis Synopsis and Outline

In this Thesis, the two main optimization avenues under consideration are, determining the environmental influence on laser vision correction and minimizing residual roughness after laser vision correction. These have been approached in a scientific manner as illustrated in Figure 9.
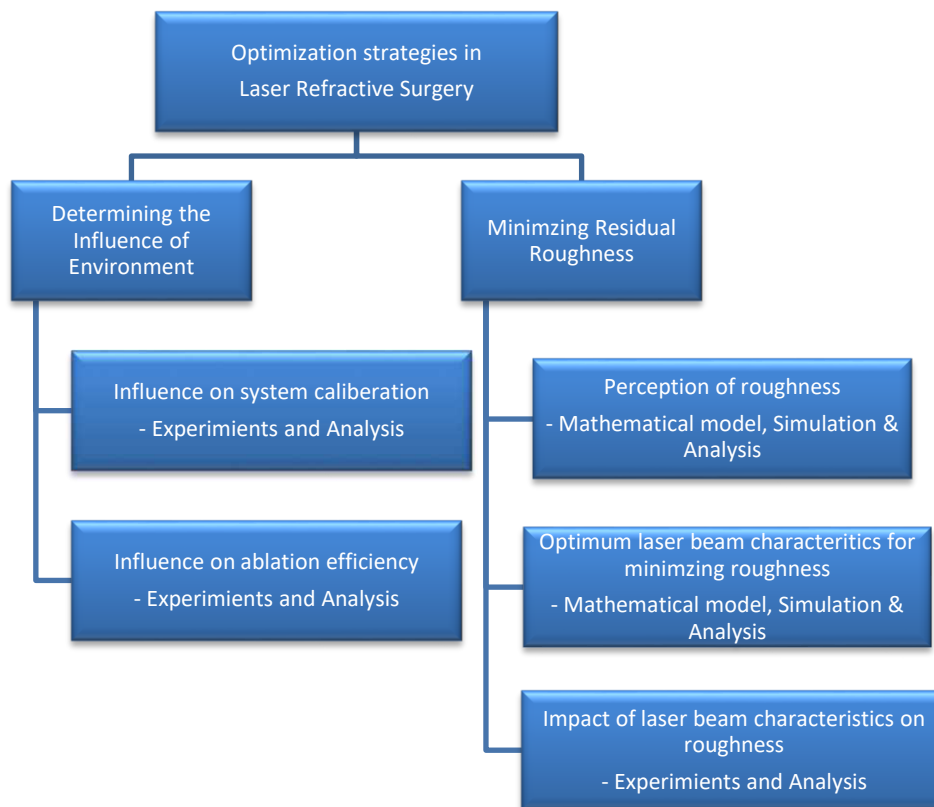
Figure 9. Specific goal and outline of the dissertation.

In the introduction section, several topical reviews of the own work related to this thesis, have been presented. These helped to understand the state of the art research and development done in the fields like bilateral symmetry in vision and its influence of refractive surgery[58], centration reference in refractive surgery[81], calibration systems used in refractive laser systems[109], and planning customized refractive procedure[50]. This formed a sound foundation to extract the main challenges currently seen in the field of laser refractive surgery, and device a strategy to approach the main research questions.

The next chapters of the thesis deal with two research question:

Research Question 1:
"Can we quantify and compensate for the influence of environment conditions on refractive procedures?"

This topic was approached in two steps.

First we quantitatively analyzed the effect of seasonal changes on the performance of excimer lasers on PMMA inside a climate controlled environment, using a large series of AMARIS laser systems. This helped understand the potential influence of seasonal changes on system calibration and refractive outcomes. **(Topic A)**

The analysis in the first step was limited by the small range of variations in the room conditions, which were being controlled to a standard value and were influenced only by the seasonal variation. Therefore, in the second step we expanded the experiments to test a wide range of environmental conditions, and different ablation materials used for system calibration like PMMA, PET, furthermore ex-vivo porcine cornea. Not only were the influence on ablation efficiency analyzed, but the influence on individual metrics characterizing the laser beam were also examined. Finally, a mathematical model was approached to potentially compensate the influence of the environment factors (temperature and humidity) on refractive outcomes. **(Topic B)**

Research Question 2:
"Can we quantify the influence of post-ablation roughness on vision and perception, and optimize refractive procedures for a minimum post-operative roughness?"

This topic was approached in three steps.

In the first step, we developed a method and performed an exploratory study to qualitatively and quantitatively analyze the impact of varying degree of corneal roughness simulated through white and filtered noise, on the retinal image. The results formed a motivation to continue the research work in this direction. **(Topic C)**

As a second step, a rigorous and generic simulation model was developed for simulating the sequential shot-by-shot ablation process based on a measured or modeled beam profile. Using this simulation model, we analyzed the impact of laser beam characteristics like spot energy, spot diameter, super Gaussian order, truncation radius, spot geometry, spot overlap and lattice geometry on ablation smoothness. Finally, we defined a theoretical framework for determining the optimum Laser beam characteristics for achieving smoother ablations in Laser Vision Correction. **(Topic D)**

This was followed by experiments to give empirical evidence for the impact of laser beam characteristics on residual roughness after ablation, with an excimer laser system. Furthermore, an optimum placement strategy for placing the laser spots to discretize the ablation volume, was explored and empirically tested. **(Topic E)**

Chapter 2 and 3 individually present the methods and results of each of the respective topics under research mentioned above. Chapter 4 discuss the findings and their relationship to one another and to the state of the art; also identifying the limitations of our methods.

In chapter 4, an outlook is also presented; as a means to identify the aspects that could not be analyzed in our attempts, but hold relevance to the research topic under question. These aspects are the key to continue research in these fields and potentially further optimize our methods and results.

Finally, in Chapter 5, the findings of this work are summarized, along with their implications.

It is to be noted that some text in the methods, results and discussion section (chapter 2, 3 and 4) was paraphrased from self-publications under review[205,211] or already published[208,206,207] in journals, at the time of submission of this thesis.

2 MATERIALS AND METHODS

2.1 **TOPIC A**: Effect of seasonal changes in PMMA Performance using the SCHWIND AMARIS laser system

The aim of the following methods is to quantitatively analyze the effect of seasonal changes on the performance of excimer laser ablation of PMMA using the SCHWIND AMARIS lasers. By analyzing PMMA ablation performance by a large series of AMARIS laser systems inside a climate controlled environment, the influence purely coming from the seasonal changes is investigated in a large scale retrospective cross sectional review. Analyzing the effects of variations in temperature and humidity on PMMA during different seasons of a year can give more information on the influence of seasonal changes on clinical outcomes in refractive surgery using the AMARIS laser platform and also in general[204].

The performance of an AMARIS laser system is evaluated through a series of PET and PMMA ablations (PMMA test[132]) as a final check for the systems under production, in order to qualify the system as ready for clinical use. The PET ablations are used to estimate the nominal number of laser pulses required to ablate a material of specified thickness and ablation properties; whereas, PMMA ablations are used to estimate the single laser pulse fluence and the ablation performance by comparing the achieved ablation to the planned ablation. These series of ablations are repeated throughout the lifetime of a laser system with a defined frequency in order to calibrate the system to a nominal performance level. Generally, a higher single laser pulse fluence, and more number of nominal laser pulses, shall lead to deeper ablations in PMMA, and ideally a similar behavior during ablation of the cornea tissue.

In this study, 826 consecutive AMARIS systems (including models 500E, 750S, 1050RS) manufactured from February 2012 to February 2018 (6 years) were retrospectively reviewed. For every system, PET and PMMA ablations performed as a final check in production, were considered, to quantitatively analyze the effect of seasonal changes on the performance of excimer laser ablation of PET and PMMA. All the ablations were conducted in climate controlled environment at the SCHWIND production facility in Kleinostheim, Germany. Although the room conditions were set to a constant value, a small range of deviation in the set temperature and relative humidity could not be avoided. Since this deviation (21-24°C temperature and 30-50% Relative humidity) was very small compared to the variations in temperature and relative humidity due to the seasonal changes, the pure influence of the seasonal changes could still be evaluated.

Seasonal outcomes were evaluated in terms of PMMA and PET Performance stratified for every month in a year, as well as stratified for each season in a year. The seasons were defined with respect to the calendar months as, winter (January to March), spring (April to June), summer (July to September) and autumn (October to December).

Statistical Analysis

- Since the standard PMMA test comprises of 12 different ablations[132], for each laser system the mean performance and standard deviation in all the ablations was calculated.

- There are two energy settings available in the AMARIS laser system (High Fluence standard value of "1.0mJ" (~450mJ/cm^2) and Low Fluence standard value of "0.7mJ" (~300mJ/cm^2)). For each laser system, single laser pulse fluence (estimated with PMMA ablations) and nominal number of laser pulses (estimated with PET ablations), were recorded for both the energy settings.
- Based on the distribution of the two energy settings in the AMARIS laser system, and the measured single pulse fluence and nominal number of laser pulses, the overall system performance was calculated for each laser system and termed as the 'technical' performance of the system.
- The parameters analyzed in the following steps were: Single laser pulse fluence (High fluence and low fluence), nominal number of laser pulses (High fluence and low fluence), Mean performance (in 12 PMMA ablations per system), Standard deviation (in 12 PMMA ablations per system), and technical performance of the system (comprising distribution of the two energy settings). For each of these parameters, the global average was calculated for all the laser systems under analysis.
- The lasers were stratified depending on the season of the year and depending on months of a year.
- Student's T-test was performed to statistically compare the stratified values of the parameters based on the season of the year, with the global values of the parameters. The level of statistical significance was set to ≤ 0.05.
- Percentage deviation in stratified values of each parameters was calculated with respect to the global values

The results of this analysis are presented in the section 3.1

2.2 **TOPIC B**: Impact of various humidity and temperature settings on excimer laser ablation of PET, PMMA and porcine corneal tissue

The aim of the following methods is to quantitatively analyze the impact of a wide range of temperature (~18°C to ~30°C) and humidity (~25% to ~80% relative humidity) conditions on excimer laser ablation of PET, PMMA and ex-vivo porcine cornea. Furthermore, we examine whether PMMA calibration may compensate for the variations in the climatic conditions, to limit their possible influence in clinical outcomes[205].

All the equipment used for the tests described in this section, including the SCHWIND AMARIS 1050RS (Schwind eye-tech solutions, Germany) were placed inside a climate chamber (Weiss Umwelttechnik GmbH, type '315'/SD 40…120DU – S' at ACTS, Magna in Sailauf, Germany). The various tests were conducted at different climate (temperature and relative humidity) settings. The porcine eyes were procured from a local slaughterhouse and transported to the test location. The pigs were killed less than 4 hours before starting the tests; however, they were killed for the commercial purposes of the slaughterhouse and were not sacrificed for the tests mentioned in this work. The porcine eyes were stored in glucose solution (1l saline solution + 19 ml of DMEM Low glucose solution from PAA Laboratories GmbH) at room temperature (~23°C), during transportation. At the test location, the eyes were stored in refrigeration, until being ablated with an excimer laser. The eyes showing unwanted characteristics like tears and abrasions in the epithelium, non-transparent cornea and stale smell were removed from the cohort.

A schematic representation of the workflow involving various steps followed in the methods is presented in Figure 10.
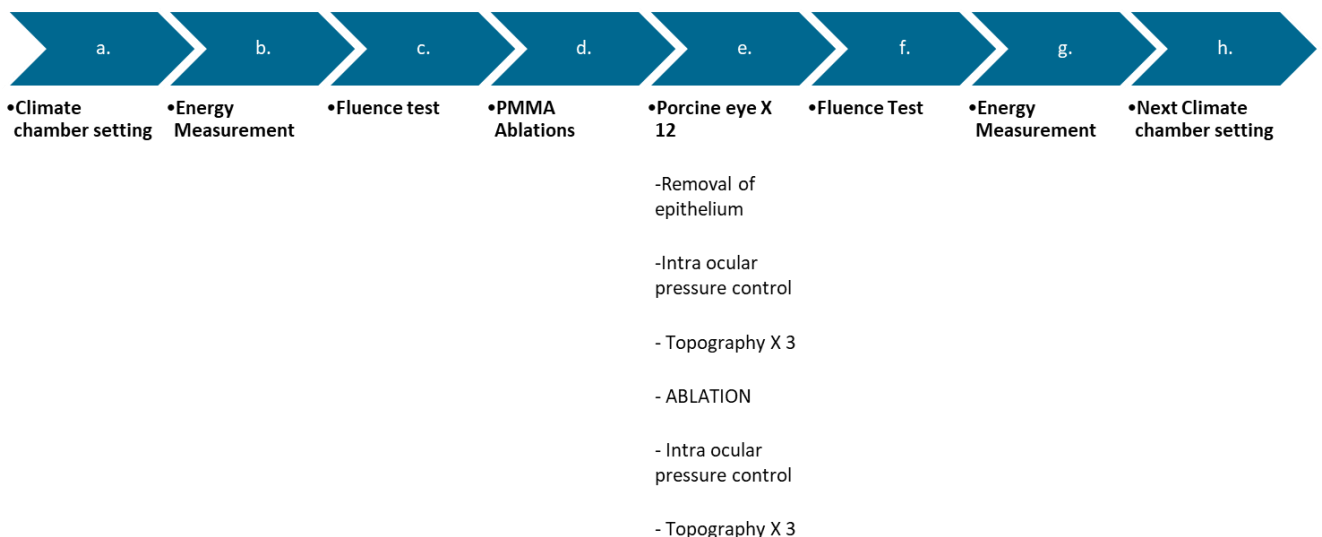
Figure 10. A schematic representation of the workflow involving various steps performed with an aim to analyze the impact of humidity and temperature on excimer laser ablation of PMMA, PET and porcine corneal tissue.

The various steps shown in the workflow (Figure 10) are elaborated as follows:

Climate chamber setting (Constitutes 'a' from the workflow shown in Figure 10)

The temperature and relative humidity in the climate chamber was set to the base setting of temperature ~24±1°C and relative humidity (RH) ~45±2% respectively. This setting represented the normal room conditions.

Energy Measurement (Constitutes 'b' from the workflow shown in Figure 10)

The single laser pulse energy was measured with a moving laser spot (using coherent EnergyMAX J-25MUV-193) and the values were recorded. The energy sensor was placed in the open, under the laser beam (close to the laser focus).

Material Ablation (Constitutes 'c to d' from the workflow shown in Figure 10)

Ablations were performed on PET and PMMA material of standard and controlled thickness and shapes. The ablations were performed in order to measure the fluence of the single laser pulse, and to estimate the efficiency of laser ablation on material of known ablation properties[132]. Fluence was measured for two energy settings available in the laser system (High Fluence standard value of 1.0mJ (450mJ/cm2) and Low Fluence standard value of 0.7mJ (300mJ/cm2)). The ablations ranged from a planned ablation depth of 27µm to 202µm (in cornea, 11µm to 89µm in PMMA) and ablation zone of 6.5mm.

Preparation of porcine eye (Constitutes 'e' from the workflow shown in Figure 10)

- Removal of epithelium

  The epithelium was removed using surgical instrument Hockey Knife and Amoils brush.

- Intra ocular pressure control

  Intra ocular pressure was controlled with an infusion of Fresenius freeflex® Beutel Ringerlösung. The pressure in the eye was subjectively checked by touching the corneal surface with a fingertip, by a trained tester (Biomedical Engineer), in order to match the intra ocular pressure commonly observed in an eye of a live human. For the purpose of these tests, it was assumed that the intra ocular pressure of the porcine eyes and human eyes is similar. After controlling the intra ocular pressure, the infusion was removed from the eye.

- Measurement of corneal topography

  Artificial tear drops (Oculosoft Care Multi) were used to moisturize the cornea. The eye was aligned with the Keratron SCOUT topographer (Optikon2000 SPA, Rome, Italy) and corneal curvature measurements were performed. At least three measurements were performed and Maloney indices were recorded in all topographic measurements.

Laser ablation on porcine eyes (Constitutes 'e' from the workflow shown in Figure 10)

All the treatments were prepared using the SCHWIND CAM software in Aberration-Free treatment mode (SCHWIND eye-tech-solutions, Germany). For the entire ablation standard High (1.0mJ (450mJ/cm2)) and Low fluence (LF 0.7mJ (300mJ/cm^2)) laser pulse distribution of the Schwind ablation profile was used[150]. The eye was mounted on a holder and positioned at the ablation plane (aligned to the corneal vertex). For all the eyes, identical treatment parameters were used. These are summarized in Table 3 and depicted as a snapshot of the treatment plan in SCHWIND CAM software (Figure 11). The repetition rate of the laser system was 1050 Hz for all the tests, however, the local frequency of ablation was limited to the 'intelligent thermal effect control' frequency (normal iTEC frequency) of the AMARIS platform (i.e. system repetition rate limited to 40 Hz local ablation frequency)[212].

Parameter	Value
Age	1 year
Planned refraction	-15D
Maximum ablation depth	363µm
Keratometric readings (K1 and K2)	21D
Treatment type	LASIK Aberration free
Optical Zone	7.5mm
Transition Zone	2.5mm
Corneal pachymetry	750µm
Ablation profile type	Non-wavefront guided aspheric profile

Table 3. Parameters used for planning the treatment in SCHWIND CAM software

Figure 11. Snapshot of the treatment plan in SCHWIND CAM software

After ablation, the corneal topography measurement was repeated. The porcine eye was discarded and the step 'e' was repeated for the next porcine eye. In this manner a total of 12 eyes were ablated for each climate chamber setting.

Material Ablation and energy measurement (Constitutes 'f to g' from the workflow shown in Figure 10)

The single laser pulse energy was measured and the PET ablations were repeated (like in steps 'b' and 'c' above, as *shown in Figure 10*).

Change in Climate chamber setting (Constitutes 'h' from the workflow shown in Figure 10)

The Climate chamber was adjusted to different test settings. For each test setting, steps 'b' to 'g' were repeated, as *shown in Figure 10*.

The different Climate chamber settings (test settings) are presented in *Table 4*. These were non-sequential to avoid/reduce hysteresis, condensation, and model bias. Each setting was realized in a quasi-adiabatic manner, taking a total 1.5 hours (1 hour for temperature/humidity change and 0.5 hour for thermal stabilization) to move from one test setting to the next. These settings were achieved with a precision of <1°C in terms of the temperature and <2% in terms of the relative humidity (according to the calibration certificate, Weiss Umwelttechnik GmbH). The three-day long test plan was designed such that in one day several ablations are performed in three different test settings. In this manner, a total of nine climate settings were tested in three days. At

the end of each test day, the climatic chamber was brought back to standard base climate settings of ~24±1°C temperature with ~45±2% RH.

Setting	Temperature	Relative Humidity
1	~24±1°C	~45±2%
2	~18±1°C	~25±2%
3	~18±1°C	~80±2%
End of Day 1 → Return to base climate setting ~24±1°C with ~45±2% RH		
4	~30±1°C	~80±2%
5	~30±1°C	~25±2%
6	~24±1°C	~25±2%
End of Day 2 → Return to base climate setting ~24±1°C with ~45±2% RH		
7	~24±1°C	~80±2%
8	~30±1°C	~45±2%
9	~18±1°C	~45±2%
End of Day 3 → Return to base climate setting ~24±1°C with ~45±2% RH		

Table 4. Different temperature and humidity test settings that were realized in a climatic chamber for the purpose of the tests that lasted three days. At the end of each day, the climate chamber was brought back to the base setting (~24±1°C with ~45±2% RH)

Analysis

For the purpose of analysis and presentation of results, for each test setting, all the measurements (single pulse energy, high and low fluence, efficiency on PMMA, and refractive change achieved in porcine eyes) performed before the ablation of porcine cornea are referred to as pre-ablation measurements. Similarly all measurements performed after the ablation of porcine cornea are referred to as post-ablation measurements.

Maloney indices were analyzed in all topographic measurements. For each eye, all the measurements performed pre-ablation and post-ablation were averaged separately. The change in defocus was calculated from the difference of post-ablation to pre-ablation Average Keratometric readings. The change in Cylinder was calculated from

the difference of post-ablation to pre-ablation Cylinder readings, as the composite change in cardinal and oblique astigmatism components.

Laser Scanning Deflectometery[213,109] was performed to measure the refractive change achieved in PMMA.

All the output values were normalized based on the average value of the metric. This was done in order to analyze the results in the form of percentage relative change. We describe the dependencies via a linear approximation. Hence, multiple linear regression was performed using least square method with the predictive factors (Input parameters): Temperature, Relative Humidity and Time stamp (since the beginning of the test).
The linear ablation model was designed to estimate the outputs based on the predictive factors. The generalized linear model approach was used, which can be represented with the following Equation:

$$Output = m1 \cdot T + m2 \cdot RH + m3 \cdot t + C$$

Equation 4

Here, the input parameters Temperature, Relative Humidity and time are represented as 'T', 'RH' and 't' respectively. The Output means pre-ablation and post-ablation single pulse energy, high and low fluence, efficiency on PMMA, and refractive change achieved in porcine eyes. The slopes (m1, m2 and m3) and constant term (C) was calculated for each Output parameter. The coefficient of determination (R^2) was calculated for each Output parameter and statistical significance of the predictive factors was evaluated, with $p <= 0.05$ as the level of significance.

After ensuring the credibility of the ablation model, the influence of climate settings was modelled for Single Laser Pulse Energy, Single Laser Pulse Fluence, ablation efficiency on PMMA, and ablation efficiency on porcine cornea tissue. Based on these outcomes, a working window of climate settings was defined for an optimum operation of the laser system.

The results of this analysis are presented in the section 3.2

2.3 **TOPIC C**: Impact of residual roughness after corneal ablation in perception and vision

The aim of the following methods is to propose an approach to convert wavefront aberrations modified for a varying degree of roughness, characteristic to the laser ablation process, to a visual PSF, in order to calculate the polychromatic retinal image. Using this approach, the impact of varying degree of corneal roughness (characterized as random and filtered noise), on the simulated retinal image, is analyzed qualitatively and quantitatively.[206,207]

The methods published by Ravikumar et al.[125] were used in the simulations. They employed a model of ocular chromatic aberration based on population average levels of Longitudinal Chromatic Aberrations (LCA), which has been shown to vary little from eye to eye[214], to examine the impact of different levels of monochromatic aberrations and Transverse Chromatic Aberrations (TCA), which are known to vary widely from eye to eye. Based on the methods, polychromatic PSFs calculated for the wavefront aberration function of the eye, were used to compute retinal images for spectrally homogeneous targets.

Theoretical Background for simulating retinal images

- The wavefront aberration function of the eye was used to calculate the Monochromatic complex pupil function:

$$PF(x, y) = P(x, y) \cdot e^{\frac{-i2\pi}{\lambda}W(x,y)}$$

Equation 5

  Where, x and y are the pupil coordinates, $P(x,y)$ is the amplitude component which defines shape, size and transmission of the system pupil, $W(x,y)$ is the wave aberration function, and λ is the reference monochromatic wavelength of light at which the wavefront was defined. The parameter $P(x,y)$ takes the Stiles-Crawford Effect in to account. The wavefront $W(x,y)$ can be defined using a series of Zernike coefficients calculated over a pupil diameter.

- Monochromatic PSF was calculated from the complex pupil function using Fraunhofer approximation formula:

$$PSF(x, y) = \left| FT\left[P(x, y) \cdot e^{-\frac{i2\pi}{\lambda}W(x,y)} \right] \right|^2$$

Equation 6

- If wavefront aberration maps are available for a representative selection of wavelengths in the spectrum of the polychromatic source, then the calculation of PSF can be repeated at each wavelength to obtain a family of spread functions.

  In our simulations, we entered the wavefront for a wavelength of 550nm, and the software estimated the wavefront (high and low order aberrations) for other wavelengths as previously described[215].

Polychromatic PSF was calculated using series of such monochromatic PSF and weighting them by the luminance (S(λ)) of the polychromatic source at that wavelength

$$PSF_{poly}(x,y) = \int S(\lambda) P(x,y,\lambda) d\lambda$$

<div align="right">*Equation 7*</div>

Where, (S(λ)) is given by the height of the source spectrum curve shown below the LCA curve in *Figure 12*. Although, the luminance of the polychromatic source was considered, the methods did not modulate the polychromatic PSF for the sensitivity of the retina.
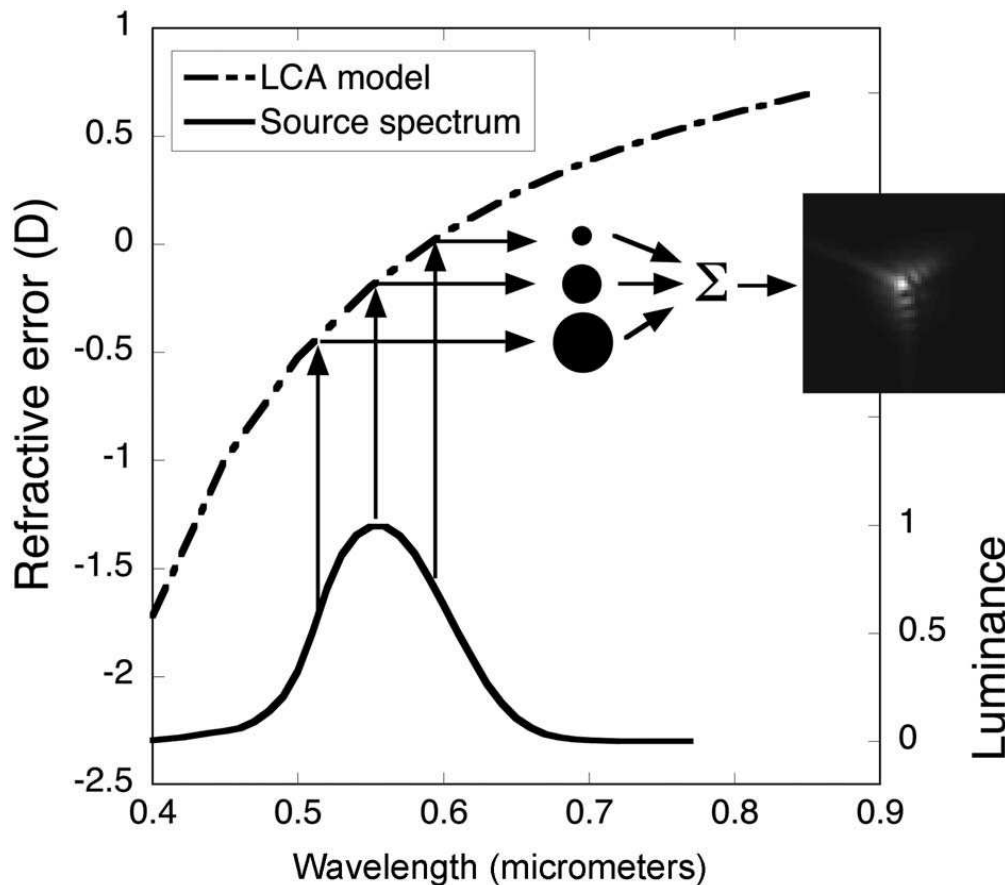
Figure 12. Graphical interpretation of text Equation 7 for computing the polychromatic PSF as the sum of luminance-weighted monochromatic PSFs. For each wavelength in the source spectrum, a monochromatic PSF is computed from monochromatic aberrations plus the focal shift associated with LCA and the lateral displacement associated with TCA; the diagram shows three such PSFs schematically as blur disks of varying diameter. The luminance weighting of each blur disk is given by the height of the source spectrum curve shown below the LCA curve. (Courtesy Ravikumar et. al. (J Opt SocAm A Opt Image SciVis. 2008 Oct;25(10):2395-407))

- Simulated polychromatic retinal image was calculated by convoluting the polychromatic PSF with the object image:

$$I(x, y) = PSF_{poly}(x, y) \otimes O(x, y)$$

Equation 8

Where I(x,y) is the simulated retinal image and O(x,y) is the object image.

- For each simulated retinal image, Strehl ratio and Visual Strehl Ratio computed in frequency domain (VSOTF) was calculated[216]

A preliminary version of Indiana Retinal Image Simulator (IRIS) was used for all the simulations, which implements the various steps detailed above.

Methodology for simulating Random and Filtered noise

For simulating the retinal image, wavefront was input into the IRIS software in the form of corresponding Zernike coefficients (*Figure 13*). The wavefront was simulated for 6mm diameter. The signal included the 2-4th Zernike orders, while noise used 7-8th Zernike orders. Noise was scaled to predetermined RMS values. All the terms in 5th and 6th Zernike order were set to 0, to avoid overlapping of signal and noise.
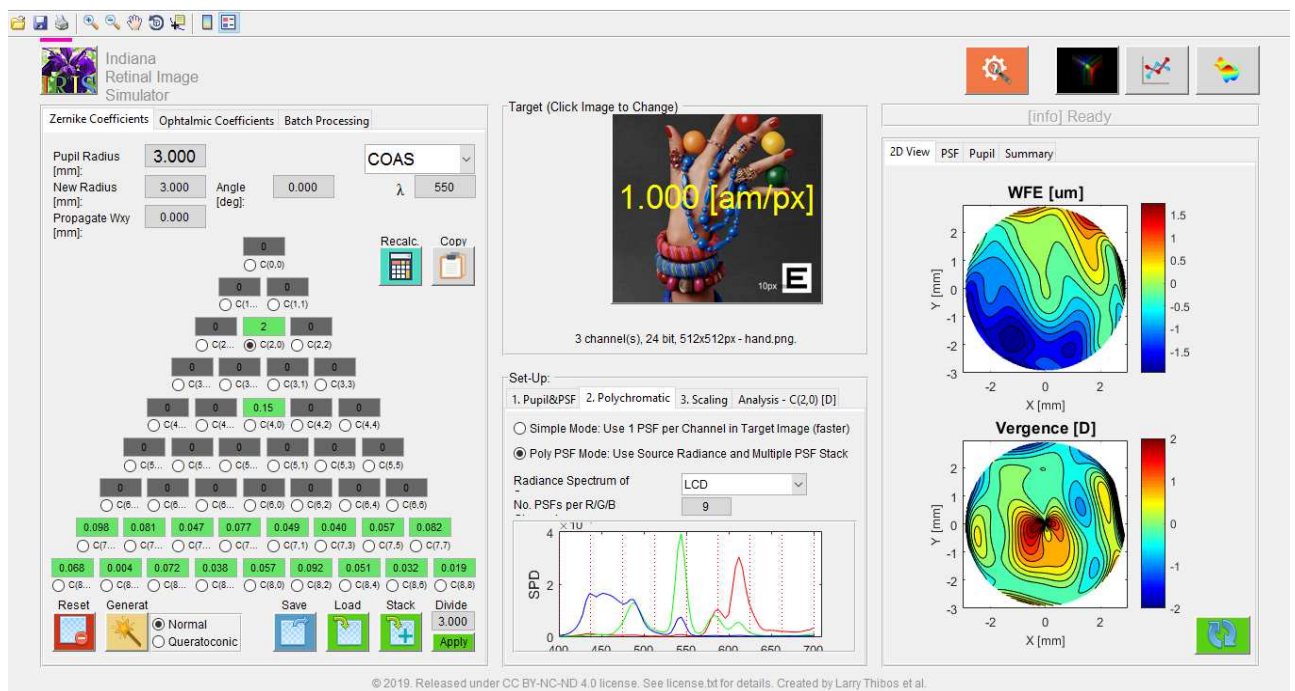

Figure 13. Graphical User Interface of the Indiana Retinal Image Simulator (IRIS) used to simulate the polychromatic retinal images.

For simulating random noise, random Higher Order Aberrations (7th and 8th Zernike Order) were calculated. The same set of Zernike coefficients representing random

noise were used in all simulation cases involving random noise, unless mentioned otherwise.

Filtered noise was simulated, using a reticular pattern, with degrees of freedom (amplitude of the signal, spatial frequency and width of signal channels), fit to Zernike polynomials of upto 8th order. A randomization factor was added to the pattern to account for the perturbations expected in the real world situations (*Figure 14*).
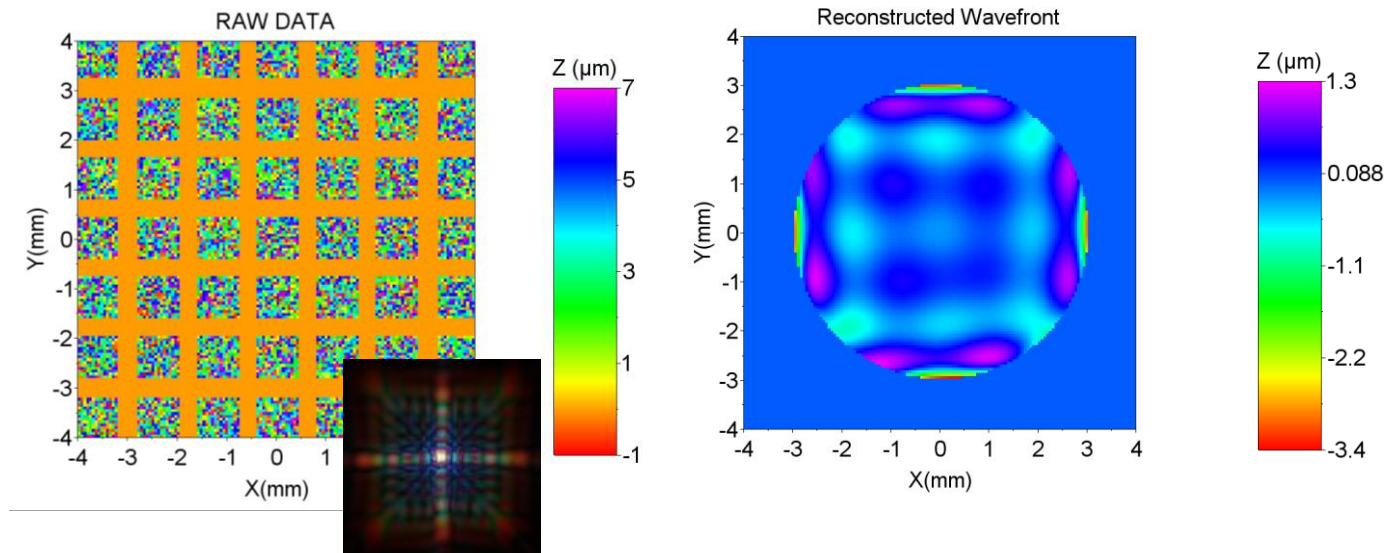
Figure 14. Left: Example of the filtered noise simulated using a reticular pattern (inset corresponding PSF). Right: The wavefront map reconstructed from the Zernike coefficients obtained after fitting the filtered noise pattern to Zernike Polynomials (up to 8th order), with a fit diameter of 6mm.

Standard settings for the simulation cases

The standard values of the input parameters used for all the simulations in the IRIS software are summarized in *Table 5*. Only one of these input parameter was manipulated at a time, depending on the simulation cases.

Input parameters	Standard value
Pupil size	6 mm
Defocus Z[2,0]	2 µm (-1.54D)
Spherical Aberrations Z[4,0]	0.15 µm
Wavefront signal	2nd-4th order Zernike coefficients
Noise signal	7th and 8th Zernike coefficients giving an RMS of 0.25 µm at 6mm diameter
Spatial frequency for filtered noise	0.48 cycles per mm (at corneal plane)
Reference wavelength	550 nm
Stiles-Crawford Sigma	0.115
Spectral power distributions of image	~34nm period (9 channels)

Table 5. The standard values of the input parameters used for all the simulations in the IRIS software. Only one input parameter was manipulated at a time, depending on the simulation cases.

Simulation Cases

The impact of varying degree of roughness, refractive error, pupil diameter, spherical aberrations and spatial frequency of the filtered noise, was individually analyzed on the simulated retinal image through various simulation cases. These cases are summarized in *Table 6*. For the parameters not mentioned in the table 2, their standard values were used as described in *Table 5*.

Simulation Case Number	Z[2,0] (µm)	Z[4,0] (µm)	Pupil Diameter (mm)	Noise Type	Noise RMS at 6mm diameter (µm)
1	0	0	6	None	-
2	0	0	6	Random	0.25
3	0	0	6	Filtered	0.25
4	0	0	6	Random	0.65
5	0	0	6	Filtered	0.65
6	2	0.15	6	Random	0.25
7	2	0.15	6	Filtered	0.25
8	2	0.15	6	None	-
9	2	0.15	3	None	-
10	2	0.15	3	Random	0.25
11	2	0.15	3	Filtered	0.25
12	2	0	6	None	-
13	2	0	6	Random	0.25
14	2	0	6	Filtered	0.25

Table 6. Settings for different simulation cases for the analyzed metrics.

The simulation case 1 represents purely the impact of chromatic aberrations at 6mm diameter without the presence of any refractive error. Besides the simulation cases presented in *Table 6*, further simulations were performed with only filtered noise (no lower order aberrations) of different spatial frequencies (ranging from 0.34 to 1 cycles per mm defined at the cornea plane). Unlike the simulation cases presented in *Table 6*, where a single of Zernike coefficients were used, for each spatial frequency, different set of Zernike coefficients were used, however the RMS of 7th and 8th Zernike order was maintained to 0.25µm.

For each analyzed metric, simulation cases were compared based on the simulated retinal image, Strehl Ratio and VSOTF. The results of this analysis are presented in the section 3.3

2.4 **TOPIC D**: Determination of optimum laser beam characteristics: Theoretical simulations

The aim of the following methods is to present a rigorous and generic simulation model for simulating the sequential shot-by-shot ablation process based on a measured or modeled beam profile. Additionally, we test the impact of laser beam characteristics like spot energy, spot diameter, super Gaussian order, truncation radius, spot geometry, spot overlap and lattice geometry on ablation smoothness, for both theoretically modelled super Gaussian beam profiles and measured intensity beam profiles acquired using a beam profiler camera. In order to account for the impact of deviations in real world settings on the methods, a rigorous perturbation analysis is also performed.[208]

A simulation model was developed for simulating the sequential shot-by-shot ablation process based on a measured or theoretically modeled beam profile, following the simulation methodology as:

Simulation methodology

The following steps were implemented to simulate a sequential shot-by-shot ablation process:

1) Given the super Gaussian order (N) and Full Width Half Maximum (FWHM), Ro (the beam size when the radiant exposure falls to $1/e^2$ its peak value) was calculated for a theoretical super Gaussian beam using a modified equation based on the Lambert-Beer law:

$$Ro = \frac{FWHM}{\left(\frac{\ln(2)}{2}\right)^{1/(2N)}}$$

Equation 9

2) For a fixed resolution of 6 μm per element, a square matrix was calculated with defined number of elements (hereafter called as pixels), tightly enclosing the foot print of one laser pulse, calculated as explained in[43].

3) Two theoretically modelled Gaussian spot geometries were simulated. For the round spot geometry, the value of Ro (calculated in previous steps) was kept constant at each meridian. For the square spot geometry, the value of Ro was meridionally changed to match the size of the square matrix resulting in a Gaussian profile with a square base.

4) A normalized intensity distribution of the super Gaussian beam profile was calculated using the standard form of Lambert-Beer law at each pixel as[43]:

$$I(n,m) = Io \cdot \exp\left(-2 \cdot \left(r(n,m)/Ro\right)^{2N}\right)$$

Equation 10

Where I represents the intensity calculated for each pixel position defined by the coordinates n and m, Io represents the peak radiant exposure (normalized to Io = 1), and r represents the radial distance.

5) The intensity distribution was scaled for a given spot energy, using the normalized intensity distribution (*Equation 10*) and resolution (6µm) as:

$$I(n,m) = \frac{\text{Spot Energy}}{Sum(I(n,m)) \cdot \text{Resolution}} \cdot I(n,m)$$

Equation 11

6) From the calculated intensity distribution, the ablation profile (ablation depth (ds)) for a single laser pulse with normal incidence, was calculated as explained in[43], using the following relation:

$$d_S = \frac{1}{\alpha} \ln\left(\frac{I(n,m) \cdot \cos\theta}{I_{Th}}\right)$$

Equation 12

Where $\theta = 0°$, is the deviation from normal incidence. Figure 15 presents the 2D and 3D simulated ablation profile for a single laser pulse with square and round spot geometry.
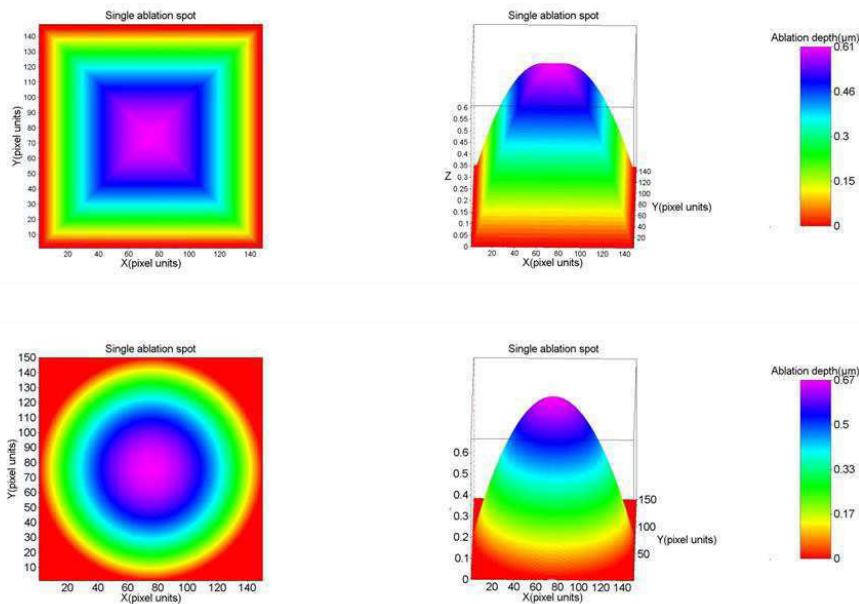

Figure 15. 2D and 3D simulated ablation profile for a single laser pulse with square (top) and round spot (bottom) geometry, for the standard test setting presented in Table 7

7) A square ablation matrix of given dimensions was defined to sequentially position several ablation profiles corresponding to a single laser pulse, simulating a larger ablation area.

8) Two types of lattices were implemented for sequential spot placement within the ablation matrix, Reticular and triangular lattice.

9) The Reticular lattice was realized by regularly arranging the ablation profiles within the rows and columns in the ablation matrix

10) The triangular lattice was realized by shifting the ablation profiles in every consecutive row and column, such that each ablation profile had an equal radial distance to all the neighboring ablation profiles in its vicinity.

11) Only a single layer of ablation matrix was simulated for both the types of lattices, without superimposing one complete ablation matrix on top of another ablation matrix.

12) A smaller ablation matrix of given dimensions was calculated after cropping the complete ablation matrix. This was done to avoid the artifacts arising from uneven ablation spot placement at the edges of the ablation matrix. Figure 16 compares the Reticle and triangular lattice in a cropped ablation matrix.
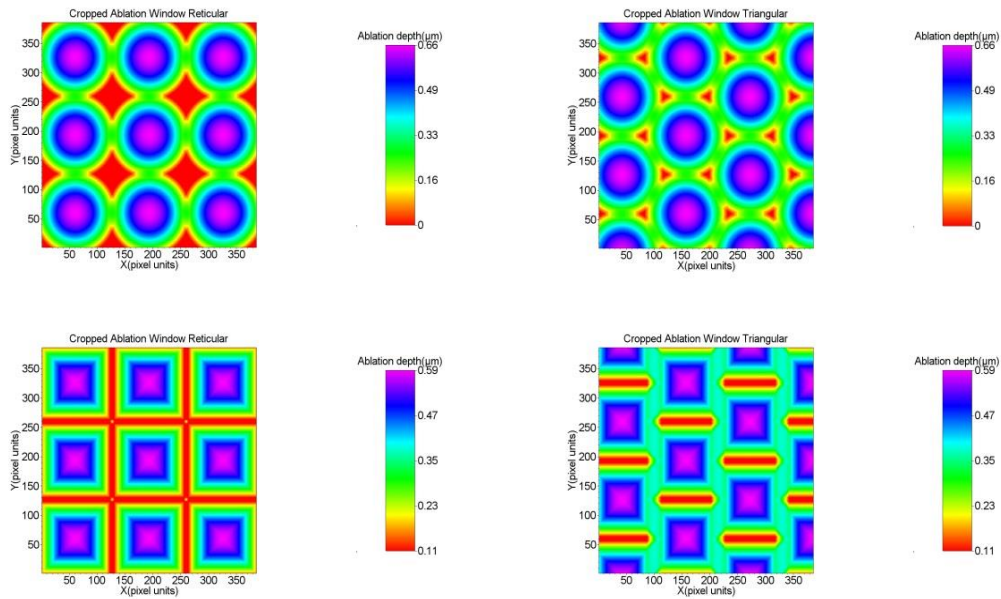
Figure 16. Reticle (left) and Triangular (right) lattice in a cropped ablation matrix, for the standard test setting presented in Table 7. The top row presents the reticular and triangular lattice simulated for a round spot geometry, whereas the bottom row presents the reticular and triangular lattice simulated for a square spot geometry. For this simulation, an overlap distance of 798µm was used.

13) The roughness in ablation was estimated using the metric

$$\text{Roughness in ablation} = \frac{RMS}{\sqrt{\text{Layer Depth}}}$$

Equation 13

58

Where RMS is the root mean square error, calculated as the standard deviation of the cropped ablation matrix, and Layer depth is the average ablation depth in the cropped ablation matrix.

14) All the steps were repeated for different values of overlap distances starting from 6 μm (equivalent to inter pulse distance of 1 pixel) to 888μm (equivalent to inter pulse distance of 148 pixels (foot print of one spot)), with an increment of 6 μm. The increment of 6 μm represents the resolution limit of the simulation model.

15) Following similar methodology (from step 6 to 14), the roughness in ablation was calculated for a measured spot profile from an excimer laser system (1050 Hz repetition rate with spot energy 1 mJ), measured using a beam profiler camera (Coherent Lasercam-HR-UV and Coherent BeamView-Software, with a laser trigger frequency of 49Hz from a distance of 150cm).

In all the simulations, the area of square ablation matrix was set to 2.56 mm^2 (with side 1.6mm). The standard test setting with the values of various input parameters is presented in *Table 7*. Most of these values were retained in all the simulations unless stated otherwise. In the tables, the spot depth and spot volume were calculated using the methods presented in[43].

Parameter	Default Value used for the model
Threshold Ablation Fluence (mJ/cm^2) for human cornea	42
Absorption Coefficient for human cornea (µm^{-1})	3.33
Spot Depth (µm)	0.66
Spot Volume (pl)	205
Spot Energy (mJ)	0.95
Full Width Half Maximum (mm)	0.5
Ro, beam size when the radiant exposure falls to 1/e^2 its peak value (mm)	0.425
Truncation Diameter (mm)/Foot print (mm)	0.89
Super Gaussian Order (N)	1
Matrix Size (pixels with resolution 6µm/pixel)	148 X148
Spot Geometry	Round
Lattice Geometry	Reticular

Table 7. Standard test settings: The values of various input parameters used in the simulation methodology. These values were retained in all the tests unless stated otherwise.

Analysis methodology included analyzing single parameters characterizing the beam profile individually, and estimating their optimum value by comparing the simulated roughness in ablation for different values of the parameters in an exploratory manner. A proper optimum configuration was found for the given input parameters, for minimizing the roughness in ablation, under the assumption that the combination of all optima also represents an optimum. The simulation program was developed in SCILAB (© Scilab Enterprises), and the analysis was performed using Microsoft Excel (© Microsoft Corporation). The optimum condition for the following parameters characterizing the beam profile was explored.

Optimum truncation size

Roughness in ablation was calculated at different overlap distances, for a super Gaussian beam profile (N = 1) with three truncation fractions (100%, 70%, 50%). The truncation fraction is hereby determined by the ratio,

$$\text{Truncation Fraction} = \frac{\text{Truncation Diameter}}{2 \cdot R_o}$$

Equation 14

The complete beam profile is represented with a truncation fraction of 100%. Smaller truncation fractions represent more cutting off the flanks of the beam profile. Different truncation fractions were realized by changing the values of Ro while keeping the truncation diameter (PH) constant. These test settings are summarized in *Table 8*. Other input parameters including the spot energy were kept constant as presented in *Table 7*.

Parameter	PH 100%	PH 70%	PH 50%
Ro, beam size when the radiant exposure falls to $1/e^2$ its peak value (mm)	0.425	0.6	0.85
Io, Peak radiant exposure (mJ/cm^2)	376	250	198
Spot depth (µm)	0.66	0.54	0.46
Spot volume (pl)	205	231	238

Table 8. Optimum Truncation size: Test settings for finding the optimum truncation size for a lower simulated roughness in ablation. The Truncation Fraction (PH) represents a ratio of truncation diameter and (2XRo), where Ro is the beam size when the radiant exposure falls to 1/e^2 its peak value. The changing test parameter is indicated in blue. The remaining input parameters, including spot energy (from Table 7) were retained in every test setting.

Optimum Super Gaussian Order

Roughness in ablation was calculated at different overlap distances, for three super Gaussian beam profiles (N = 1, N = 2, Flat Top). For the three beam profiles, spot energy, truncation diameter and other parameters were kept constant as presented in Table *7*, however some parameters changed as shown in *Table 9*.

Parameter	N = 1	N = 2	Flat Top
N, Super Gaussian Order	1	2	999
Ro, beam size when the radiant exposure falls to $1/e^2$ its peak value (mm)	0.425	0.463	0.445
Io, Peak radiant exposure (mJ/cm^2)	376	225	139
Spot depth (µm)	0.66	0.51	0.36
Spot volume (pl)	205	208	223

Table 9. Optimum Super Gaussian Order: Test settings for finding the optimum Super Gaussian Order (N) for a lower simulated roughness in ablation. The changing test parameter is indicated in blue. The remaining input parameters, including spot energy (from Table 7) were retained in every test setting.

Optimum Spot Geometry

Roughness in ablation was calculated at different overlap distances, for two spot geometries (round and square geometries). The input parameters were retained for both the spot geometries as shown in *Table 7*.

Optimum Lattice Geometry

Roughness in ablation was calculated at different overlap distances, for two lattice geometries (Reticular and triangular geometries). The input parameters were retained for both the lattice geometries as shown in *Table 7*.

Measured Vs. theoretically modeled beam profile

The roughness in ablation was calculated for a measured spot profile from an excimer laser system (as explained in the step 15 of the simulation methodology). The outcomes (roughness in ablation) of the theoretically modelled beam profile (input parameters defined in *Table 7*) were compared with the outcomes of the measured beam profile.

Impact of ablation material

For the input parameters specific to the human cornea (in *Table 7*), roughness in ablation was calculated at different overlap distances. The various simulation steps were repeated for threshold ablation fluence (67 mJ/cm^2) and absorption coefficient (5.2 µm^{-1}) specific to PMMA[217]. The other input parameters were retained from *Table 7*. The outcomes (roughness in ablation) for the two ablation materials (human cornea and PMMA) were compared.

Impact of Spot Energy and Spot Diameter

The analysis and optimization of various parameters was performed for a fix spot energy of ~1mJ and spot size (presented as the truncation diameter/foot print in *Table 7*) of ~0.9mm. This represents a realistic limit commonly seen in laser vision correction[43]. The impact of other extreme values of spot energy (0.5mJ and 1.4mJ) was simulated on the metric roughness in ablation. *Table 10* presents a comparison of the three tested energy settings.

Parameter	Basis	Low Energy	High Energy
Spot energy (mJ)	0.95	0.53	1.40
Ro, beam size when the radiant exposure falls to $1/e^2$ its peak value (mm)	0.425	0.55	0.38
Io, peak radiant exposure (mJ/cm^2)	376	153	664
Spot depth (µm)	0.66	0.39	0.83
Spot volume (pl)	205	119	258

Table 10. Optimum Spot Energy: Test settings for finding the optimum Spot Energy for a lower simulated roughness in ablation. Three values of spot energy were tested. The changing test parameter is indicated in blue. The remaining input parameters (from Table 7) were retained in every test setting.

Furthermore, the impact of other extreme values of spot sizes (0.6mm and 1.2mm) was simulated on the metric roughness in ablation. *Table 11* presents a comparison of the three tested spot sizes.

Parameter	Basis	Small spot	Large spot
Spot diameter (mm) (Foot Print)	0.89	0.60	1.20
Ro, beam size when the radiant exposure falls to $1/e^2$ its peak value (mm)	0.425	0.23	0.76
Io, peak radiant exposure (mJ/cm2)	376	1152	147
Spot depth (μm)	0.66	0.99	0.38
Spot volume (pl)	205	141	213

Table 11. Optimum Spot Diameter: Test settings for finding the optimum Spot Diameter for a lower simulated roughness in ablation. Three values of spot diameter were tested. The changing test parameter is indicated in blue. The remaining input parameters, including spot energy (from Table 7) were retained in every test setting.

Perturbation Analysis

The values of various laser beam characteristics in *Table 7* were simultaneously and randomly varied for each ablation spot in the ablation matrix. The impact of these perturbations was evaluated on the roughness in ablation. The following parameters were varied for the perturbation analysis: spot overlap, threshold ablation fluence, absorption coefficient for human cornea, spot energy, super Gaussian order, matrix size, and beam size. The spot overlap was varied between the ranges +/- 6 pixels of the original value. The rest of the parameters were varied between the ranges +/- 10% of the original value. The outcomes (roughness in ablation) with the standard test setting (*Table 7*) were compared to the outcomes with the perturbed input parameters.

The results of this analysis are presented in the section 3.4.

2.5 **TOPIC E**: Determination of optimum laser beam characteristics: Empirical Evaluation

Following the theoretical framework for determining the optimum Laser beam characteristics for achieving smoother ablations in Laser Vision Correction, the aim of the following methods is to provide empirical results of the impact of laser beam characteristics like truncation radius, lattice arrangement, and jitter on ablation smoothness measured as residual roughness in PMMA plates after being ablated with an excimer laser system.[211]

A modified SCHWIND AMARIS system was used providing a beam profile with the following characteristics: FWHM=540µm, N=1.27, 1050Hz. The laser parameters and the pulse energy were optimized following previous works[43,208]. For PMMA ablations, two configurations (with a 0.7mm pinhole and 0.75mJ and without pinhole and 0.9mJ (for fluences of 329mJ/cm^2 and 317mJ/cm^2 and corneal spot volumes of 174pl and 188pl)) were considered, along with two types of lattices (with and without ordered dithering to select the optimum pulse positions), and two types of spot placement (with and without jitter). Real ablations on PMMA (ranging from -12D to +6D with and without astigmatism) completed the study setup. The various test conditions are presented in *Table 12*. For each test condition, a total of 12 ablations were performed on PMMA, and the average efficiency (Achieved ablation/Expected ablation) was considered as the outcome.

Test number	Pinhole (Energy)	Dithering	Jitter
1	Y	N	N
2	Y	N	Y
3	Y	Y	Y
4	Y	Y	N
5	N	Y	N
6	N	Y	Y
7	N	N	Y
8	N	N	N

Table 12. Summary of the various test settings. Here for Pinhole, 'Y' represents truncation of the laser beam using a pinhole (0.7mm diameter) and 'N' represents no truncation (and for Energy, 'Y' represents 0.75mJ and 'N' represents 0.9mJ); for Dithering, 'Y' represents use of lattice with ordered dithering to select the optimum pulse positions and 'N' represents lattice without ordered dithering; for Jitter, 'Y' represents a controlled random noise (up to ±20µm in either direction) added to the theoretical scanner positions while 'N' represents no random noise.

The effect of the 2x2x2 different configurations (2 states of Pinhole, 2 sates of lattice order dithering, and 2 states of jitter spot placement) was analyzed based on the roughness in ablation estimated from the root mean square error in ablation.

An empirical comparison model was set up for evaluating the roughness induced by the ablation process, following the methodology as (see also *Table 13*):

1) Set High Low Fluence parameters to the same energy (0.75mJ) at the working plane (single fluence)
2) Perform a fluence test and a PMMA Test (Test1: pinhole, w/o dithering, w/o jitter)
3) Enable jitter=20µm
4) Perform a fluence test and a PMMA Test (Test2: pinhole, w/o dithering, jitter)
5) Enable dithering
6) Perform a fluence test and a PMMA Test (Test3: pinhole, dithering, jitter)
7) Disable jitter
8) Perform a fluence and a PMMA Test (Test4: pinhole, dithering, w/o jitter)
9) Remove the pinhole
10) Set High Low Fluence parameters to the same energy (0.9mJ) at the working plane (single fluence)
11) Perform a fluence and a PMMA Test (Test5: w/o pinhole, dithering, w/o jitter)
12) Enable jitter=20µm
13) Perform a fluence and a PMMA Test (Test6: w/o pinhole, dithering, jitter)
14) Disable dithering
15) Perform a fluence and a PMMA Test (Test7: w/o pinhole, w/o dithering, jitter)
16) Disable jitter
17) Perform a fluence and a PMMA Test (Test8: w/o pinhole, w/o dithering, w/o jitter)
18) Reset system to standard AMARIS settings

This corresponds to a non-sequential settings procedure to avoid/reduce model bias; time drifts, hysteresis effects.

Parameter	Common Parameters	Common Parameters
Repetition Rate (Hz)	1050	1050
Full Width Half Maximum (mm)	0.54	0.54
Super Gaussian Order (N)	1.27	1.27
R_0, beam size when the radiant exposure falls to $1/e^2$ its peak value (mm)	0.41	0.41
Threshold Ablation Fluence (mJ/cm^2) for human cornea	42	42
Absorption Coefficient for human cornea (μm^{-1})	3.21	3.21
Threshold Ablation Fluence (mJ/cm^2) for PMMA	67	67
Absorption Coefficient for PMMA (μm^{-1})	5.2	5.2
Parameter	Default Value	Test Value
Truncation Diameter (mm)/Foot print (mm)	0.7	None
Spot Energy (mJ)	0.75	0.9
Pinhole Transmission (%)	76%	100%
Cut-off at the flanks (%)	27%	0%
Laser Power (mW)	788	945
Peak radiant exposure (mJ/cm2)	329	317
Corneal Spot Depth (μm)	0.64	0.63
Corneal Spot Size (mm)	0.7	0.82
Corneal Spot Volume (pl)	174	188
PMMA Spot Depth (μm)	0.31	0.30
PMMA Spot Size (mm)	0.7	0.74
PMMA Spot Volume (pl)	74	72
Dithering	None (Heuristic reticular search)	Ordered (Ordered Dithering Search)
Jitter (μm)	0	20

Table 13. Dual test settings: The values of various input parameters used in the ablation methodology. These values were retained in all the tests unless stated otherwise.

Truncation (Pinhole)

Roughness in ablation was measured with (standard setting) versus without truncation (0.7mm diameter, corresponding to 76% transmission, and 27% cut-off at the flanks). The effect of Pinhole on radiant exposure, estimated ablation depth on the cornea and PMMA is displayed in *Figure 17*.
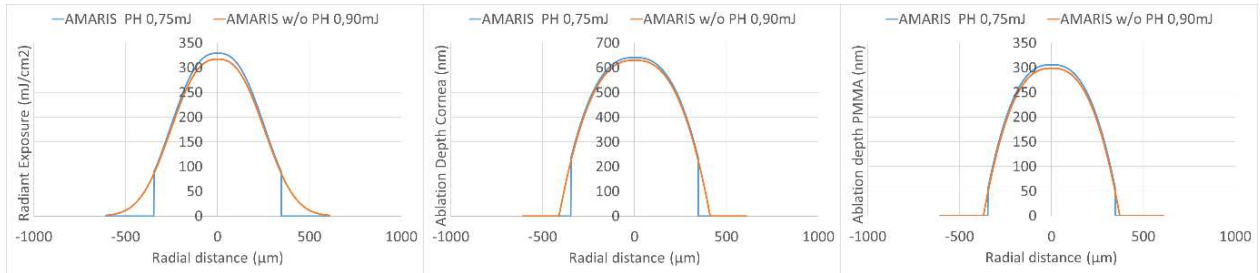
Figure 17. Effect of pinhole truncating the beam to a 0.7mm spot. Essentially the pinhole cuts-off the flanks of the spot, reducing the total energy of the pulse at the expense of inducing high frequency signals. The peak radiant exposure (related to the pulse energy) of the beam without pinhole has been slightly reduced to keep a good comparison in the per pulse ablation volume on corneal tissue and PMMA.

Ordered Dithering Lattice Geometry

Ordered dithering is an image dithering algorithm. It is commonly used to display a continuous image on a display of smaller color depth. The algorithm reduces the number of colors by applying a threshold map M to the pixels displayed, causing some pixels to change color, depending on the distance of the original color from the available color entries in the reduced palette. This threshold map (for sides with length as power of two) is also known as an index matrix or Bayer matrix.[218]

Arbitrary size threshold maps can be devised with a simple rule: First fill each slot with successive integers. Then reorder them such that the average distance between two successive numbers in the map is as large as possible, ensuring that the table "wraps" around at edges.

The algorithm renders the image normally, but for each pixel, it adds a value from the threshold map, causing the pixel's value to be quantized one step higher if it exceeds the threshold. For example, in monochrome rendering, if the value of the pixel is less than the number in the corresponding cell of the matrix, plot that pixel black, otherwise, plot it white.

The size of the map selected should be equal to or larger than the ratio of source colors to target colors. For example, when quantizing a 24bpp image to 15bpp (256 colors per channel to 32 colors per channel), the smallest map one would choose would be 4×2, for the ratio of 8 (256:32). This allows expressing each distinct tone of the input with different dithering patterns.

Bayer has shown that for matrices of orders which are powers of two there is an optimal pattern of dispersed dots which results in the pattern noise being as high-frequency as possible.

The idea behind it is simple: given two available values a and b, let's say black and white, the value x between a and b — that should be grayish — is simulated by mixing pixels of colors a and b. To apply some ordered dithering on an image, we apply the same logic but in 2D by using a Bayer matrix. By turning the pixel on in a very specified order, the matrix creates the perception of continuous variation of color. In these

matrices, consecutive threshold values are located far apart spatially, which gives the perception of a progressive variation. This concept can be easily adapted to the discretization of an ablation volume into an integer collection of pulses per position. The task is now to express a continuous profile on basis smaller resolution. The algorithm causes some pixels to round up the number of pulses to be placed, and some others to round down. The size of the map selected should be equal to or larger than the ratio of the size of the ablation profile to the size of the spot (building block).

Jitter

In optics, the term jitter is used to refer to the oscillatory motion of the image with respect to the detector, which blurs the image. In our case, it is a controlled random noise (up to ±20µm in either direction) added to the theoretical scanner positions. This may help avoiding/breaking patterned effects in the overlapped spots. As expressed in the history of PRK:[219]

"The researchers began working in a trailer at LSU that was next to a trash compactor, which inadvertently led to a discovery. The researchers found that when the trash compactor was operating, it shook the trailer, which made the laser wobble instead of shooting straight down into the patient's eye. McDonald said that when the trailer was not vibrating, the treatments were not as smooth and the results not as good. This led to a smoothing of the procedure so the ridges the laser produced were eliminated."

PMMA Tests

8 PMMA Tests have been performed (each consisting of 12 ablations ranging from -12D to +6D)[132] and analyzed[213] from a single AMARIS system. These conformed a 2x2x2 matrix comparing with vs. without Pinhole, Dithering, and Jitter. Mean performance values, standard deviations, and roughness have been evaluated. To increase robustness 8x8 analyses, 4 vs. 4 cumulative analyses, as well as pairwise analyses were performed.

The results of this analysis are presented in the section 3.5.

3 RESULTS

3.1 **TOPIC A**: Effect of seasonal changes in PMMA Performance using the SCHWIND AMARIS laser system

Seasonal Influence

The percentage deviation in the average values of all the parameters in each season with respect to their global averages is presented individually in Figure 18 and as a group in Figure 19. All the parameters showed a strong cyclic trend with the changing season, with the most predominant change observed for winter and summer season. The percentage deviation in the parameter 'standard deviation' among the 12 PMMA ablations was particularly higher compared to the other parameters, however, this was due to the fact that percentage changes were examined in numbers of originally very low magnitude.
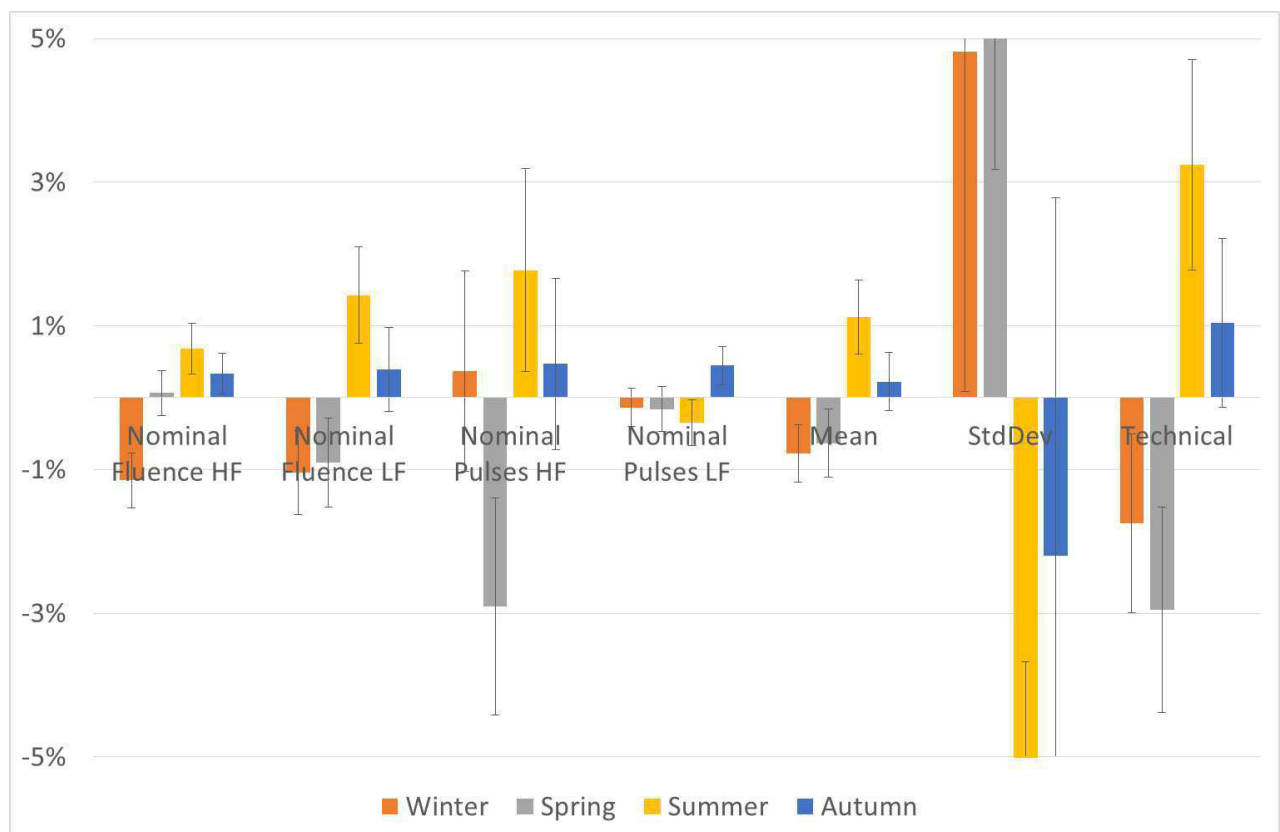

Figure 18. The percentage deviation in the average values of all the parameters in each season with respect to their global averages is presented individually. Here, 'nominal fluence' represents single laser pulse fluence, 'HF' is high fluence, 'LF' is low fluence, 'StdDev' is standard deviation, and the different seasons were defined with respect to the calendar months as, winter (January to March), spring (April to June), summer (July to September) and autumn (October to December).
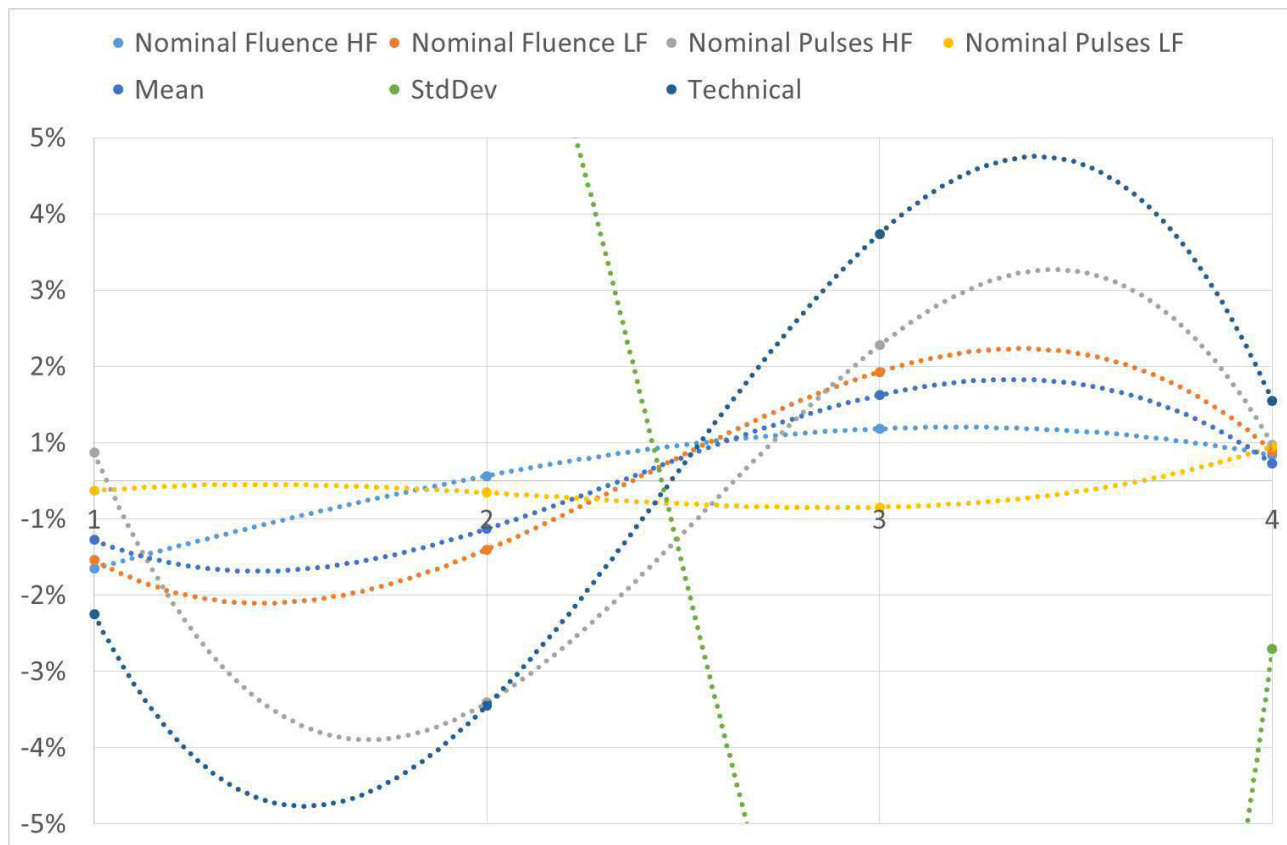
Figure 19. The percentage deviation in the average values of all the parameters in each season with respect to their global averages is presented as a group. Here, 'nominal fluence' represents single laser pulse fluence, 'HF' is high fluence, 'LF' is low fluence, 'StdDev' is standard deviation.

Although a cyclic trend can be observed for all the parameters among the various seasons, not all the observed changes reached statistical significance. The season winter and summer showed statistical significance with respect to the global values for all the tested parameters except the nominal number of laser pulses for high and low fluence setting. The trends showing statistical significance and the range or maximum deviation for each parameter is presented in Table 14. The metric technical performance of the analyzed systems showed a stronger PMMA ablation performance in Summer time compared to a weaker performance in the winter time, with the maximum seasonal deviation of 6%.

Value	Single laser pulse fluence (HF)	Single laser pulse fluence (LF)	Nominal Pulses (HF)	Nominal Pulses (LF)	Mean	Standard Deviation	Technical Performance
Season where the value was Lower than Global Average (p<0.05)	Winter	Winter	Spring	Stable	Winter	Summer	Winter
Season where the value was higher than Global Average (p<0.05)	Summer	Summer	Summer	Stable	Summer	Winter	Summer
Range or maximum deviation	2%	2%	5%	1%	2%	21%	6%

Table 14. The trends showing statistical significance and the range or maximum deviation for each parameter, analyzed in lasers stratified depending on the season of the year.

Seasonal Influence - stratification on months of a year

The percentage deviation in the average values of all the parameters in each month of the year with respect to their global averages is presented individually in Figure 20 and as a group in Figure 21. Even upon stratifying the lasers depending of the month of a year, similar cyclic trend as observed among the four seasons could be reproduced, consistently confirming the findings of the analysis. Similar to the seasonal deviations, the percentage monthly deviation in the parameter 'standard deviation' among the 12 PMMA ablations with respect to the global values, was particularly higher compared to the other parameters due the very low magnitude.

Figure 20. The percentage deviation in the average values of all the parameters in each month of the year with respect to their global averages is presented individually. Here, 'nominal fluence' represents single laser pulse fluence, 'HF' is high fluence, 'LF' is low fluence, 'StdDev' is standard deviation.
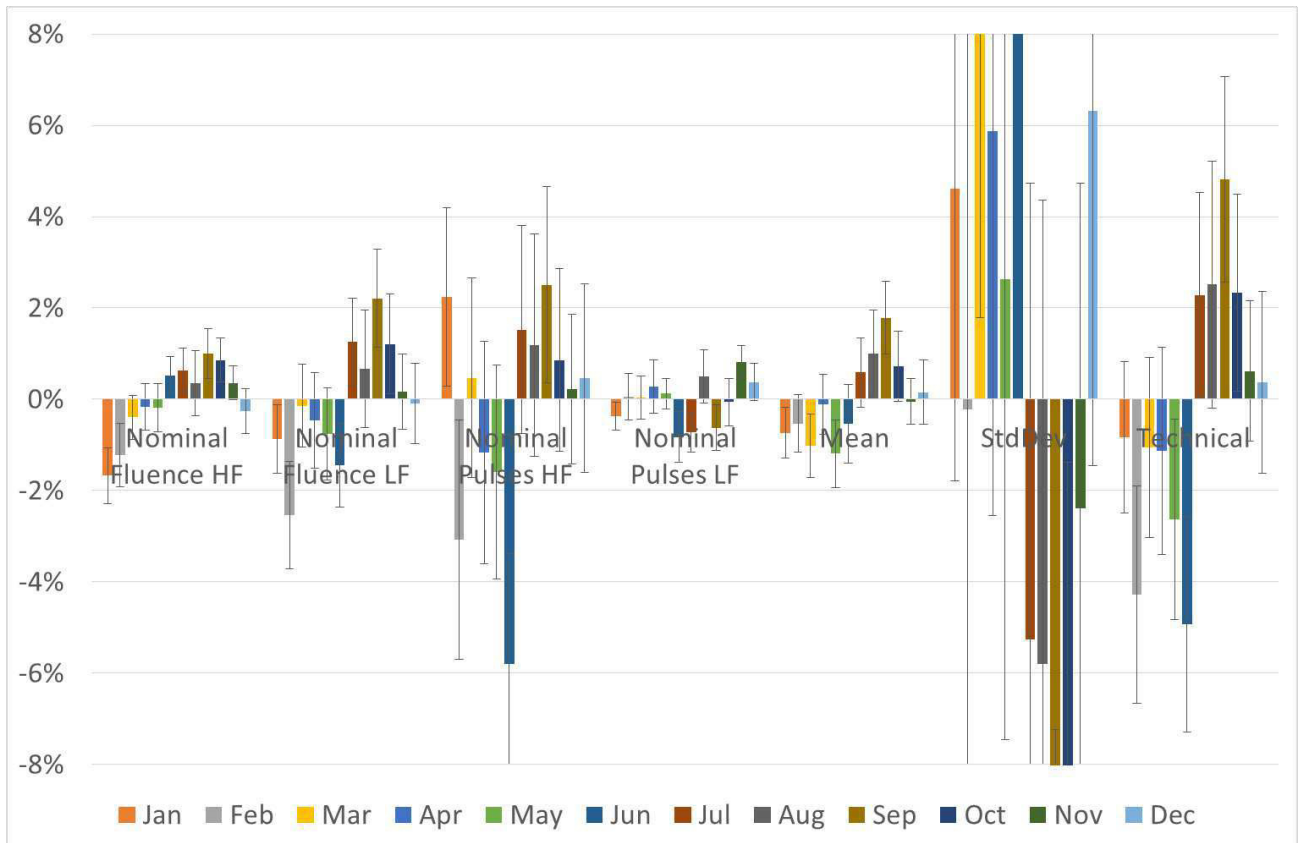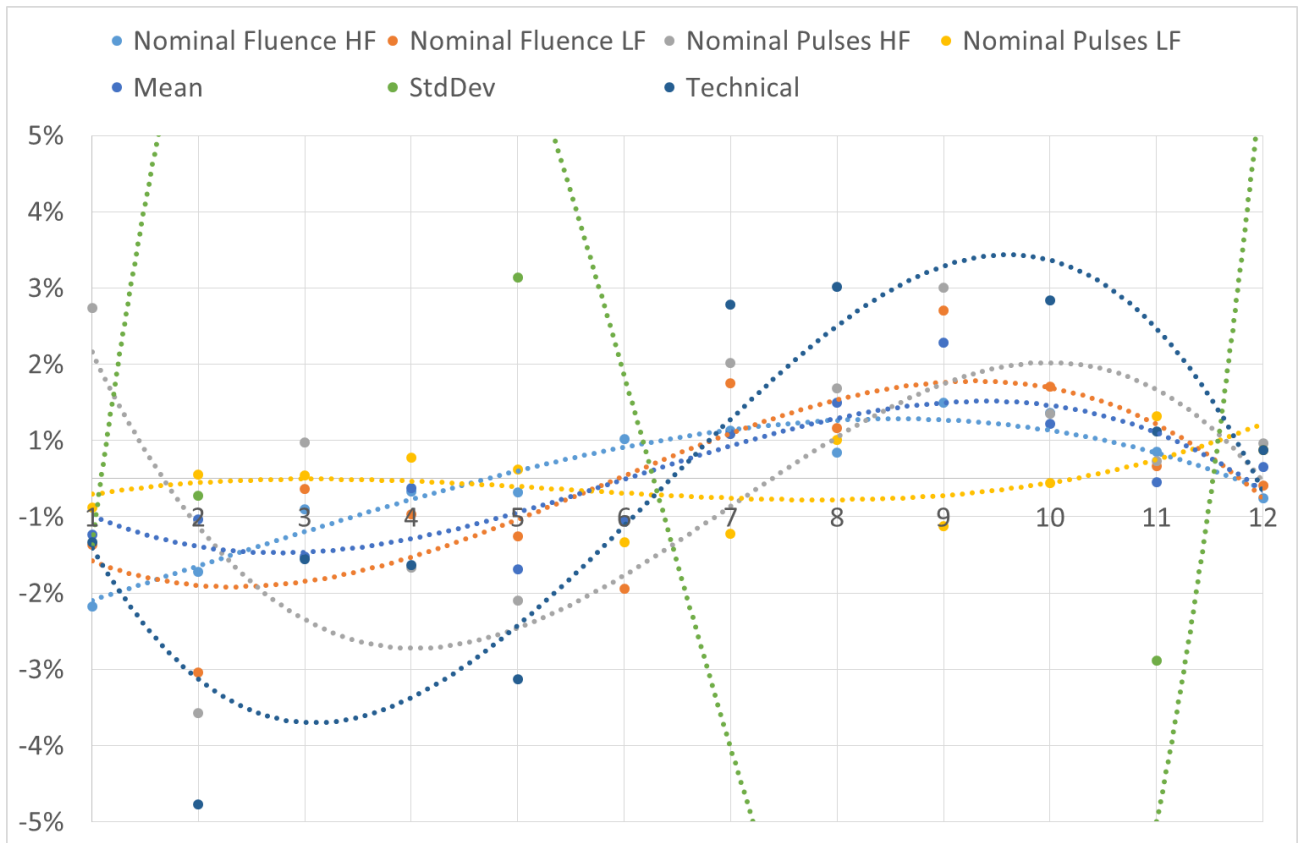
Figure 21. The percentage deviation in the average values of all the parameters in each month of the year with respect to their global averages is presented as a group. Here, 'nominal fluence' represents single laser pulse fluence, 'HF' is high fluence, 'LF' is low fluence, 'StdDev' is standard deviation.

The trend showing statistical significance among the different months of a year, and the range or maximum deviation for each parameter is presented in Table 15.

Value	Single laser pulse fluence (HF)	Single laser pulse fluence (LF)	Nominal pulses (HF)	Nominal pulses (LF)	Mean	Standard deviation	Technical performance
Months where the value was Lower than global average (p<0.05)	Jan-Feb	Jan-June	Feb-June	Stable	Jan-June	July-Oct	Jan-June
Months where the value was higher than global average (p<0.05)	June - Oct	July-Oct	July-Oct	Stable	July-Oct	Jan-June	July-Oct
Range or maximum deviation	3%	5%	9%	1%	3%	45%	10%

Table 15. The trend showing statistical significance and the range or maximum deviation for each parameter, analyzed in lasers stratified depending on months of the year.

3.2 **TOPIC B**: Impact of various humidity and temperature settings on excimer laser ablation of PET, PMMA and porcine corneal tissue

Following the methods described in 2.2, in total, 108 porcine eyes, 108 PMMA ablations and 36 PET ablations were performed in a span of 3 days, encompassing a total of 9 climate settings. Due to technical limitations of the climate chamber, at very low temperatures settings (18°C), extreme relative humidity could not be achieved despite continued attempts. Therefore, not all the climate settings in design of experiment could be reached. A comparison of the aimed and reached climate settings is graphically presented in Figure 22.
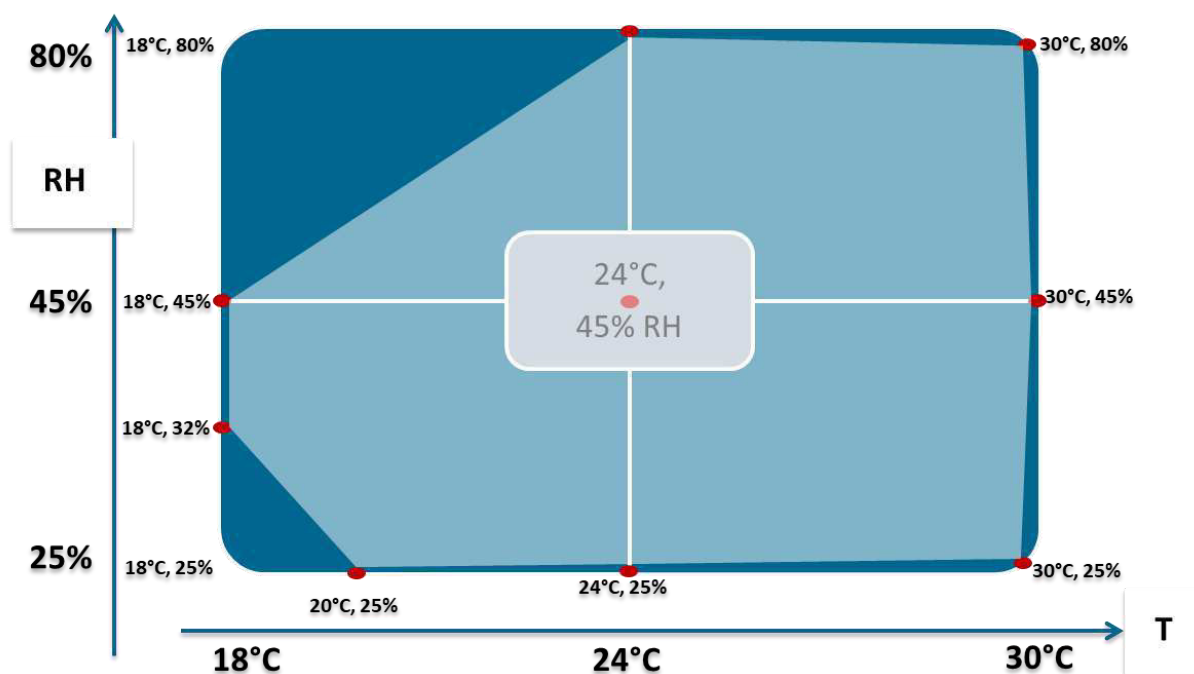

Figure 22. A graphic representation of the attempted climate settings in the design of experiment (Dark blue) versus the achieved climate settings (Light blue)

Ablation model

The ablation model for each output metric is presented in Table 16. In the table, Pre and Post represents pre-ablation and post-ablation measurements respectively. The high and low fluence are presented as HF and LF respectively. The statistically significant predictive factors for each output metric are shown in green color; all other predictive factors did not show statistical significance. The p-values for each output parameter and predictive factors are presented in brackets.

Metric	Energy Pre	HF Pre	LF Pre	PMMA	Porcine	HF Post	LF Post	Energy Post
m1 – T	-0.032% (p = 0.87)	0.073% (p = 0.63)	-0.091% (p = 0.61)	-0.185% (p = 0.33)	0.462% (p = 0.17)	0.023% (p = 0.83)	-0.055% (p = 0.72)	-0.106% (p = 0.46)
m2 – RH	-0.164% (p = 0.01)	-0.106% (p = 0.03)	-0.098% (p = 0.07)	0.035% (p = 0.46)	-0.128% (p = 0.14)	-0.163% (p = 0.00)	-0.115% (p = 0.02)	-0.233% (p = 0.00)
m3 - Time	-0.834% (p = 0.00)	-0.390% (p = 0.01)	-0.657% (p = 0.00)	-0.288% (p = 0.05)	-0.257% (p = 0.24)	-0.470% (p = 0.00)	-0.459% (p = 0.00)	-0.762% (p = 0.00)
C	126%	111%	120%	109%	100%	117%	116%	129%
R²	0.94	0.88	0.92	0.58	0.63	0.96	0.90	0.97

Table 16. Ablation model for output metrics Single Laser Pulse Energy, Single Laser Pulse Fluence, ablation efficiency on PMMA, and ablation efficiency on porcine cornea tissue, based on the predictive factors Temperature (T), Relative humidity (RH) and Time stamp (since the beginning of the test).

Temperature was not a significant predictor for any output parameter. Relative Humidity was a significant predictor for Energy (pre-ablation and post-ablation) and PET ablation performance at both energy settings. Time was a significant predictor for all output parameters, except for refractive change achieved on porcine cornea. The mean coefficient of determination of the ablation model was 0.8, suggesting a good predictability of each output parameters based on the predictive factors.

The impact of climate settings on various metrics is elaborated below, and depicted with the help of surface plots encompassing a broad range of temperature (18 to 30°C) and relative humidity conditions (20 to 80% RH). The direction of the maximum rate of change was included in the plots to indicate the environmental gradients leading to the maximum response. These surface plots were created based on the output values resulting from the ablation model, by inputting a 4X4 matrix of values for the predictive factors (Temperature 18°C, 22°C, 26°C, 30°C; Relative humidity 20%, 40%, 60%, 80%). The time stamp was taken out from the ablation model as a covariate, and its influence was eliminated from the analysis. Hence, a fixed value of average time stamp (from the beginning of the tests) was used for the analysis.

Influence of climate settings on Single Laser Pulse Energy

The impact of the climate settings on single laser pulse energy is presented in Figure 23, for the pre-ablation and post-ablation condition. Between the pre-ablation and post-ablation condition, there was a time gap of ~2 hours, in which a total of 12 porcine eyes, 12 PMMA, and 4 PET ablations were performed. The change in temperature did not affect the single pulse energy, for a constant relative humidity. However, changing the relative humidity from 20% to 80% resulted in changing the single pulse energy from 105% to 95% pre-ablation, and 106% to 92% post-ablation. Dry climate conditions resulted in higher single pulse energy, compared to moist climate conditions, resulting in lower single pulse energy.
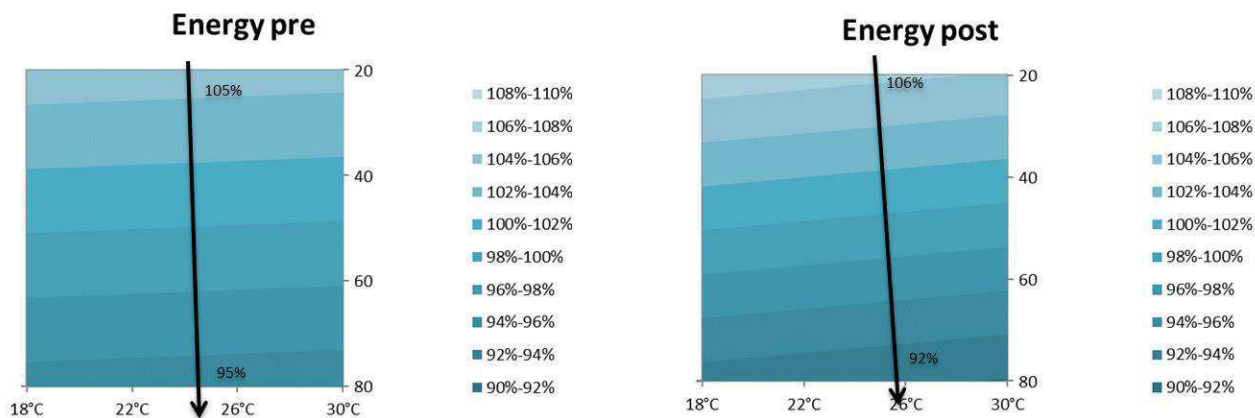
Figure 23. Surface plots presenting the impact of change in relative humidity (in Y-axis) and temperature (in X-axis) on single laser pulse energy, pre-ablation (in left) and post-ablation (in right).

Influence of climate settings on Single Laser Pulse Fluence

The impact of the climate settings on single laser pulse fluence for the two energy settings (high and low fluence) is presented in Figure 24, for the pre-ablation and post-ablation condition. Between the pre-ablation and post-ablation condition, there was a time gap of ~1.75 hours, in which a total of 12 porcine eyes, 12 PMMA ablations were performed. The change in temperature did not affect the single laser pulse fluence, for a constant relative humidity. The High and low fluence setting behaved similarly. Furthermore, the fluence behaved similarly pre-ablation and post-ablation. Dry climate conditions (20% RH) resulted in higher single laser pulse fluence (~103%), compared to moist climate conditions (80% RH), resulting in lower single laser pulse fluence (~95-97%).
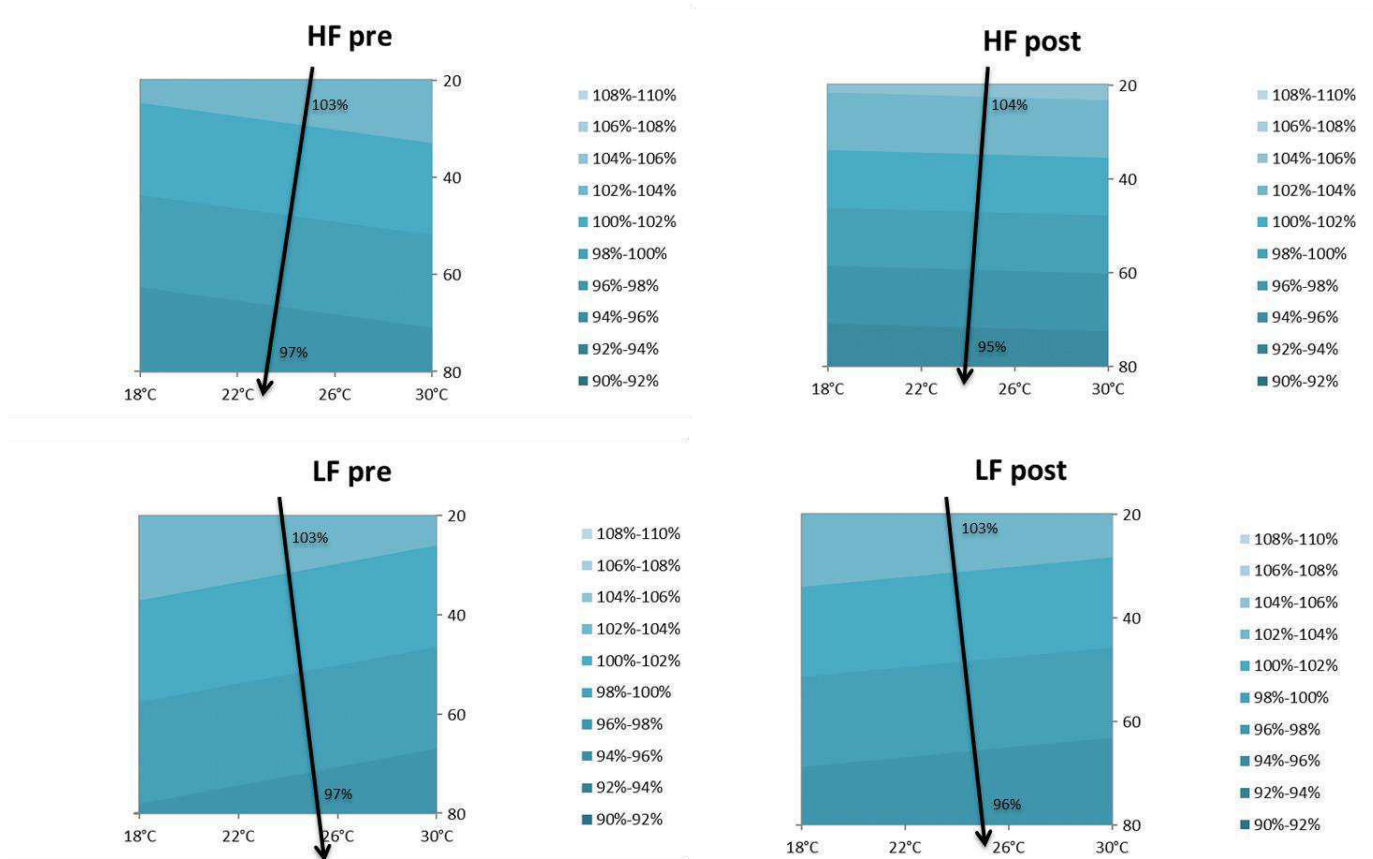
Figure 24. Surface plots presenting the impact of change in relative humidity (in Y-axis) and temperature (in X-axis) on single laser pulse fluence (Top: High fluence; Bottom: Low fluence), pre-ablation (in left) and post-ablation (in right).

Influence of climate settings on Laser ablation efficiency on PMMA

The impact of the climate settings on Laser ablation efficiency on PMMA is presented in Figure 25, for the mean values and standard deviation in ablation efficiency. The mean ablation efficiency remained stable and close to 100% for a wide window of climate settings. For extremely low humidity and high temperatures (30°C with 20%RH, dry and hot conditions), reduced performance (98%) was recorded, compared to increased efficiency (103%) at low temperatures and high humidity (18°C with 80%RH, cold and dry conditions). The trend was similar for the standard deviation in ablation efficiency, however, percentage changes were large in comparison, since they depict a change in very small numbers compared to the mean values.
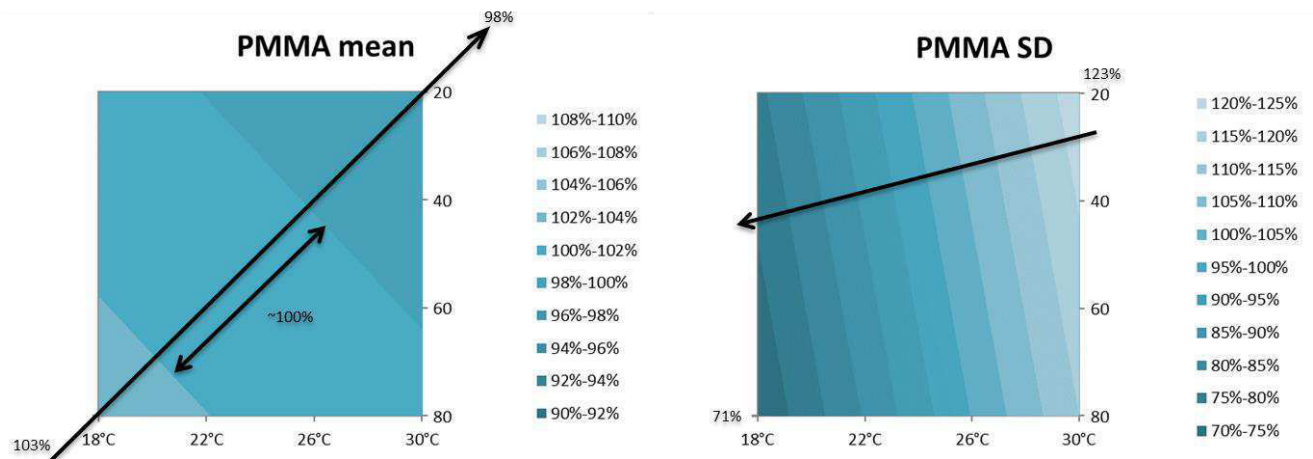
Figure 25. Surface plots presenting the impact of change in relative humidity (in Y-axis) and temperature (in X-axis) on mean (left) and standard deviation (right) of ablation efficiency in PMMA.

Influence of climate settings on Laser ablation efficiency on porcine cornea tissue

The impact of the climate settings on porcine cornea ablation is presented in Figure 26, for the mean values and standard deviation in achieved refractive change. For extremely low humidity and high temperatures (30°C with 20%RH, dry and hot conditions), higher refractive change (106%) was recorded, compared to reduced efficiency (93%) at low temperatures and high humidity (18°C with 80%RH, cold and dry conditions). The trend was similar for the standard deviation in refractive change, however, percentage changes were large in comparison, since they depict a change in very small numbers compared to the mean values.
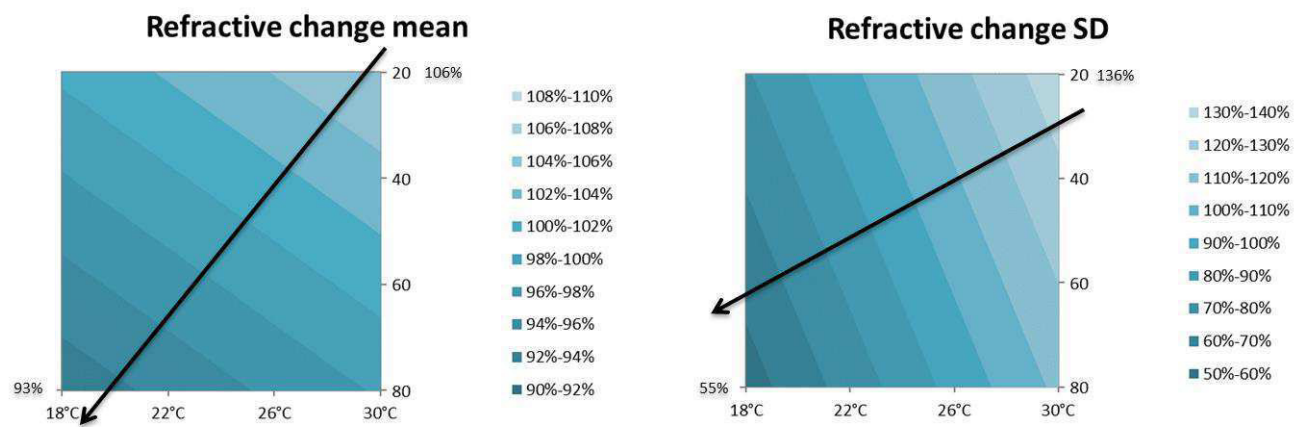

Figure 26. Surface plots presenting the impact of change in relative humidity (in Y-axis) and temperature (in X-axis) on mean (left) and standard deviation (right) of refractive change achieved in porcine cornea.

3.3   **TOPIC C**: Impact of residual roughness after corneal ablation in perception and vision

In total 20 simulation cases were examined and compared on the basis of VSOTF, Strehl Ratio and the simulated retinal image qualitatively.

Impact of chromatic aberrations and roughness (random and filtered noise)

The impact of the chromatic aberrations and roughness is presented in *Figure 27*. Without any refractive error, chromatic aberrations resulted in image quality metric VSOTF of ~0.44 and Strehl Ratio of 0.3. Addition of random noise on the signal resulted in deteriorating both VSOTF (from 0.44 no noise to 0.075 with 0.25μm RMS random noise, and 0.0078 with 0.65μm RMS random noise) and Strehl Ratio (from 0.3 no noise to 0.03 with 0.25μm RMS random noise, and 0.005 with 0.65μm RMS random noise). The decrease in image quality was even worse with the addition of filtered noise.


Original Object Image	Case 1; Signal = 0; Noise = 0; Pupil = 6mm VSOTF = 0.442 ; Strehl = 0.3
Case 2; Signal = 0; 0.25μm RMS (Random); Pupil = 6mm VSOTF = 0.075 ; Strehl = 0.03	Case 3; Signal = 0; 0.25μm RMS (Filtered); Pupil = 6mm VSOTF = 0.045 ; Strehl = 0.022

| Case 4; Signal = 0; 0.65μm RMS (Random); Pupil = 6mm
VSOTF = 0.0078 ; Strehl = 0.005 | Case 5; Signal = 0; 0.65μm RMS (Filtered); Pupil = 6mm
VSOTF = 0.002; Strehl = 0.003 |

Figure 27. Impact of roughness without refractive error on simulated retinal image. Top left: Original object image; Top right: simulated retinal image without refractive error and noise signal; middle left: simulated retinal image without refractive error, with random noise signal (0.25μm RMS); middle right: simulated retinal image without refractive error and with filtered noise signal (0.25μm RMS); bottom left: simulated retinal image without refractive error, with random noise signal (0.65μm RMS); bottom right: simulated retinal image without refractive error and with filtered noise signal (0.65μm RMS).

Impact of roughness with refractive error

The impact of the roughness with refractive errors (Defocus and spherical aberrations) is presented in *Figure 28*.
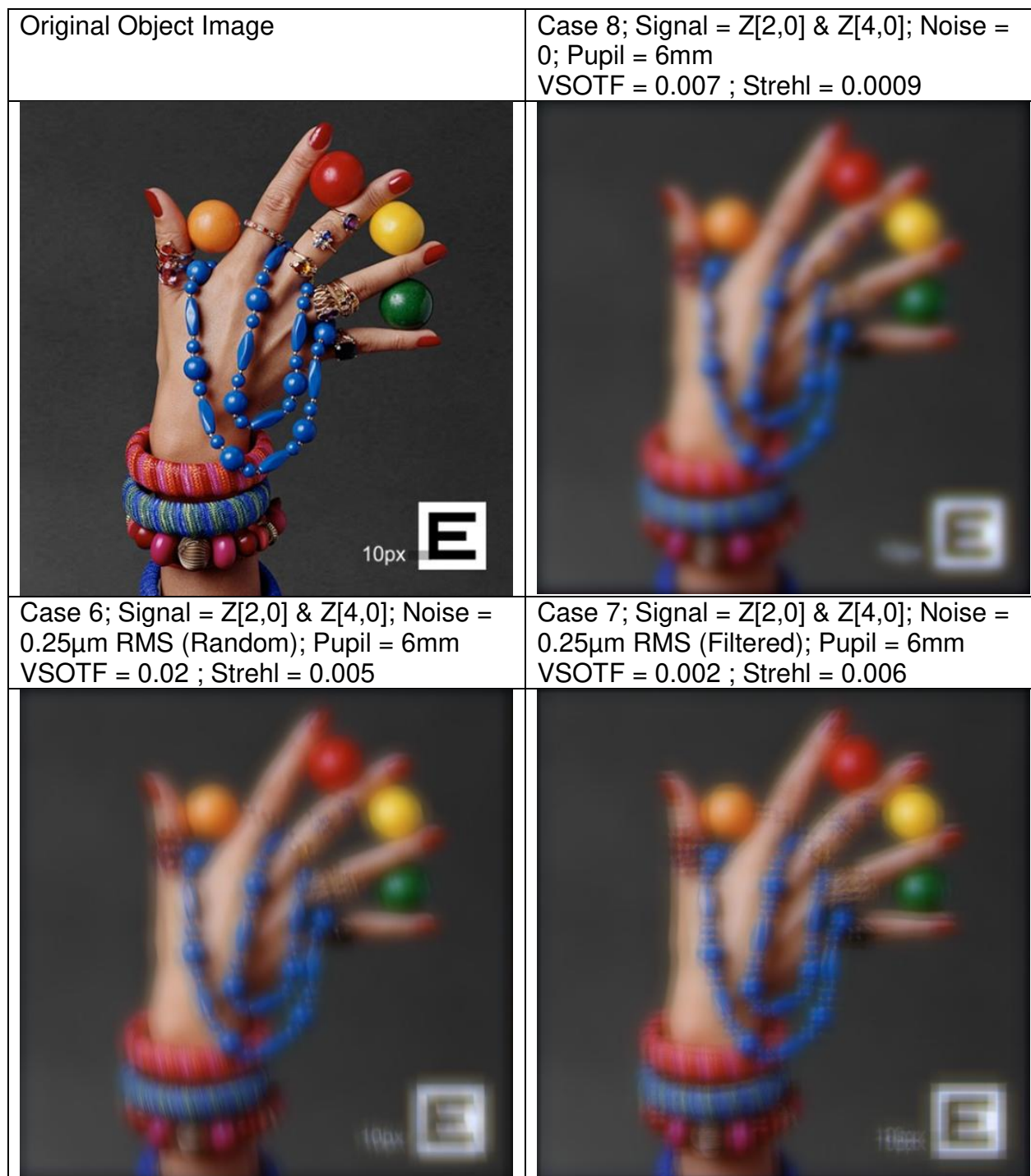
Figure 28. Impact of roughness with refractive errors (defocus and spherical aberration) on simulated retinal image. Top left: Original object image; Top right: simulated retinal image with refractive error but no noise signal; Bottom Left: simulated retinal image with refractive error and random noise signal; Bottom Right: simulated retinal image with refractive error and filtered noise signal.

In the presence of refractive errors of this order ($Z[2,0]$ = 2µm and $Z[4,0]$ = 0.15µm), adding random noise improved the VSOTF (0.007 to 0.02) and Strehl Ratio (0.0009 to 0.005). However, for the filtered noise, the image quality metric VSOTF (0.007 to 0.002) deteriorated while the Strehl Ratio improved (0.0009 to 0.006).

Impact of Spherical Aberrations

Adding spherical aberrations to the signal results in improving the simulated retinal image quality in the absence of any noise (VSOTF 0.0025 for $Z[4,0]$ = 0µm to 0.007 for $Z[4,0]$ = 0.15 µm), in presence of random noise (VSOTF 0.0132 for $Z[4,0]$ = 0µm to 0.02 for $Z[4,0]$ = 0.15 µm), and also in presence of filtered noise (VSOTF 0.0006 for $Z[4,0]$ = 0µm to 0.002 for $Z[4,0]$ = 0.15 µm). This affect is presented in *Figure 29*.

Case 8; Signal = Z[2,0] & Z[4,0]; Noise = 0; Pupil = 6mm VSOTF = 0.007 ; Strehl = 0.0009	Case 12; Signal = Z[2,0]; Noise = 0; Pupil = 6mm VSOTF = 0.0025 ; Strehl = 0.00045
Case 6; Signal = Z[2,0] & Z[4,0]; Noise = 0.25µm RMS (Random); Pupil = 6mm VSOTF = 0.02 ; Strehl = 0.005	Case 13; Signal = Z[2,0]; Noise = 0.25µm RMS (Random); Pupil = 6mm VSOTF = 0.0132 ; Strehl = 0.0045

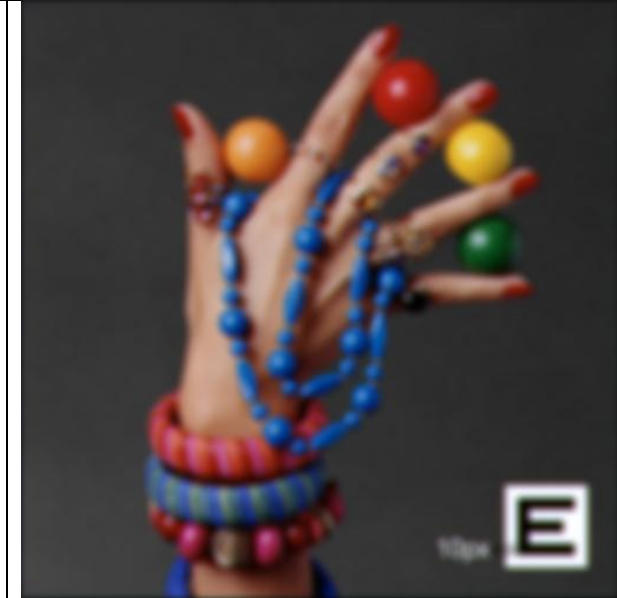| Case 7; Signal = Z[2,0] & Z[4,0]; Noise = 0.25µm RMS (Filtered); Pupil = 6mm VSOTF = 0.002 ; Strehl = 0.006 | Case 14; Signal = Z[2,0]; Noise = 0.25µm RMS (Filtered); Pupil = 6mm VSOTF = 0.0006 ; Strehl = 0.0059 |

Figure 29. Impact of spherical aberration in the presence of defocus error on simulated retinal image, with and without the noise signal. Top: simulated retinal image with no noise; middle: simulated retinal image with random noise RMS 0.25 µm at 6mm diameter; Bottom: Simulated retinal image with filtered noise RMS 0.25µm at 6mm diameter. The simulation results with spherical aberrations Z[4,0] = 0.15µm are presented in the left column, and spherical aberrations Z[4,0] = 0µm in the right column.

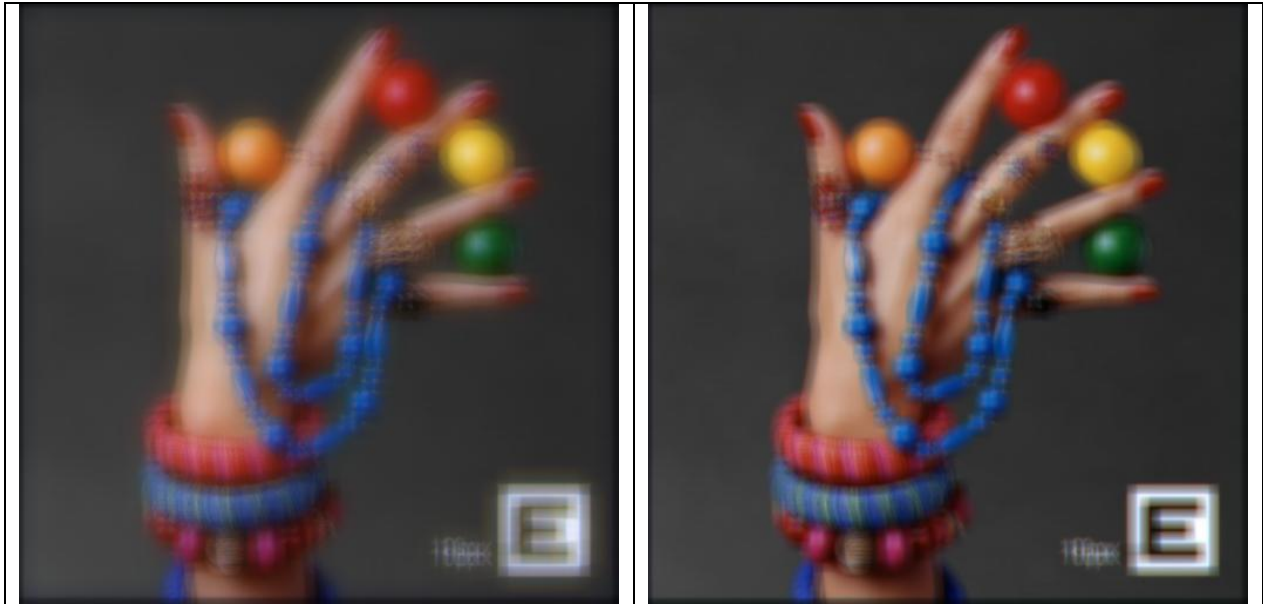*Impact of Pupil Diameter*

Reducing the pupil size resulted in dramatically improving the simulated retinal image without any noise (Strehl Ratio 0.0009, VSOTF 0.007 at 6mm pupil to 0.018 and 0.03 at 3mm pupil respectively), and in the presence of random noise (Strehl Ratio 0.005, VSOTF 0.02 at 6mm pupil to 0.062 and 0.08 at 3mm pupil respectively). However, for

filtered noise, the gains in image quality were marginal in terms of VSOTF (0.002 at 6mm pupil to 0.0025 at 3mm pupil), although evident in terms of Strehl Ratio (0.006 at 6mm pupil to 0.022 at 3mm pupil) and the image quality in general. These affects are presented in *Figure 29*.

Case 8; Signal = Z[2,0] & Z[4,0]; Noise = 0; Pupil = 6mm VSOTF = 0.007 ; Strehl = 0.0009	Case 9; Signal = Z[2,0] & Z[4,0]; Noise = 0; Pupil = 3mm VSOTF = 0.03 ; Strehl = 0.018
Case 6; Signal = Z[2,0] & Z[4,0]; Noise = 0.25µm RMS (Random); Pupil = 6mm VSOTF = 0.02 ; Strehl = 0.005	Case 10; Signal = Z[2,0] & Z[4,0]; Noise = 0.25µm RMS (Random); Pupil = 3mm VSOTF = 0.08 ; Strehl = 0.062
Case 7; Signal = Z[2,0] & Z[4,0]; Noise = 0.25µm RMS (Filtered); Pupil = 6mm VSOTF = 0.002 ; Strehl = 0.006	Case 11; Signal = Z[2,0] & Z[4,0]; Noise = 0.25µm RMS (Filtered); Pupil = 3mm VSOTF = 0.0025 ; Strehl = 0.022

Figure 30. Impact of pupil diameter in the presence of refractive errors (defocus and spherical aberration) on simulated retinal image. Top: simulated retinal image with no noise; middle: simulated retinal image with random noise RMS 0.25 µm at 6mm diameter; Bottom: Simulated retinal image with filtered noise RMS 0.25µm at 6 mm diameter. The simulation results with pupil diameter 6mm are presented in the left column, and pupil diameter 3mm in the right column.

Impact of spatial frequency of the filtered noise

Simulations were performed for six different spatial frequencies of the filtered noise pattern (0.34, 0.48, 0.52, 0.67, 0.81, 1 cycles per mm defined at the cornea plane). For each spatial frequency, different set of Zernike coefficients were used, however the RMS of 7th and 8th Zernike order was maintained to 0.25µm. The impact of spatial frequency on simulated retinal image quality is presented in *Figure 31*. The image quality metrics VSOTF and Strehl Ratio showed a similar and cyclic progression; VSOTF and Strehl Ratio reached their peaks at the spatial frequency of 0.67 cycle per mm.
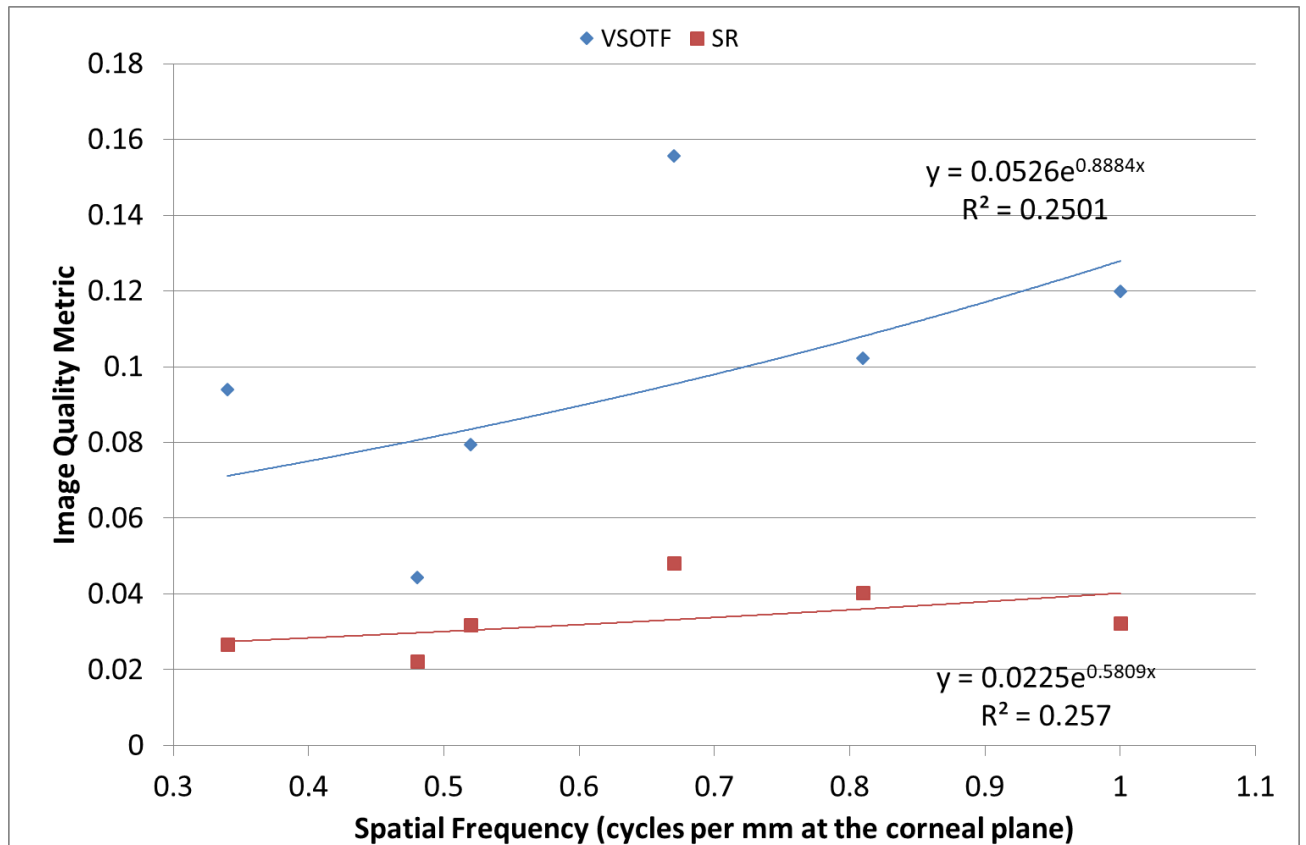
Figure 31. Impact of spatial frequency on simulated retinal image quality. The image quality metrics (VSOTF and Strehl Ratio) reached their peak at the spatial frequency of ~0.67 cycle per mm.

3.4 **TOPIC D**: Determination of optimum laser beam characteristics: Theoretical simulations

In general, the layer depth progressed as $1/\text{overlap}^2$, decreasing as the overlap distance increased. For the input parameters presented in *Table 7*, the progression of layer depth is shown in *Figure 32*. In *Figure 32* and subsequent figures in this section, the horizontal axis (overlap (µm)) represents the overlap distance (or inter spot distance) between two consecutive ablation spots in µm, where a lower overlap represent a tighter spot placement.
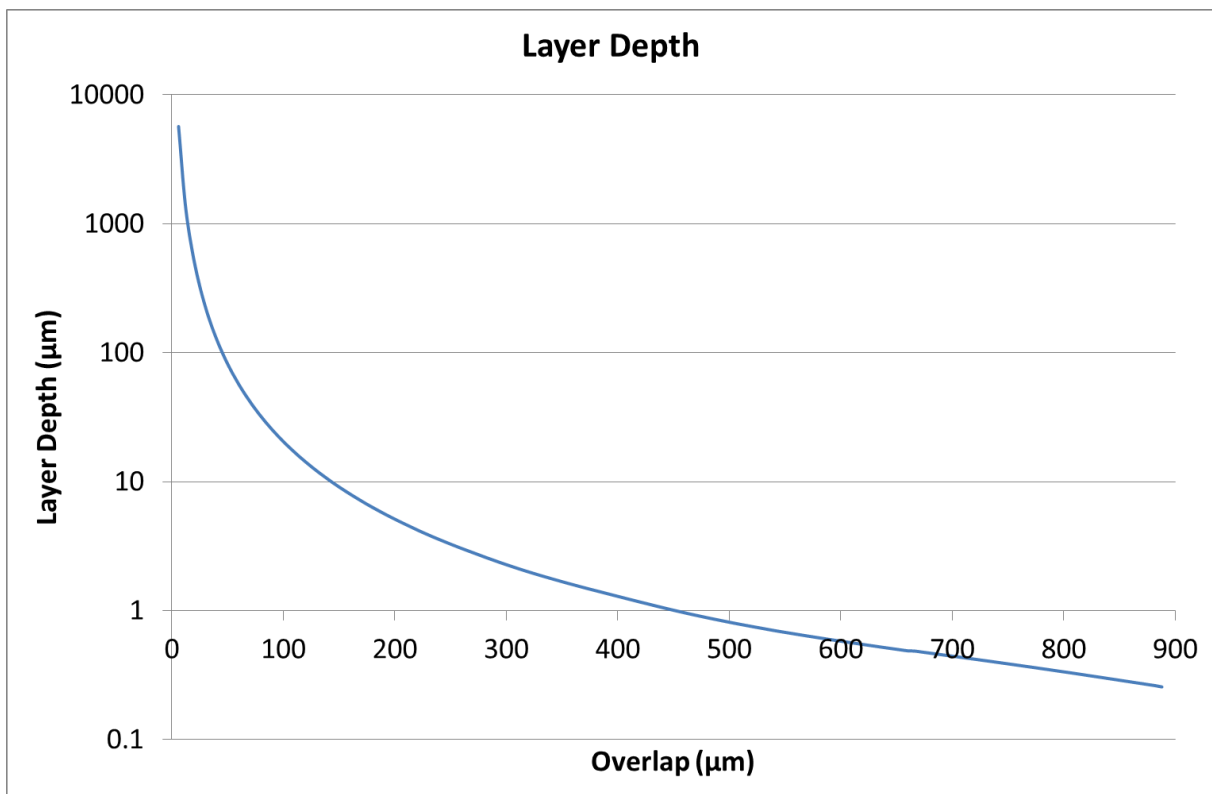
Figure 32. The progression of layer depth with respect to the overlap distance, for the input parameters presented in Table 7. The horizontal axis (overlap (µm)) represents the overlap distance (or inter spot distance) between two consecutive ablation spots in µm, where a lower overlap represent a tighter spot placement. The layer depth progressed as $1/\text{overlap}^2$ with respect to the overlap distances.

The optimum condition for the following parameters characterizing the beam profile was found:

Optimum truncation size

The results of the simulations are presented in *Figure 33*. The complete beam profile represented with a truncation fraction of 100%, resulted in the smoothest ablations. A further truncation of the beam profile increased the roughness in ablation for overlap distances less than 600µm. These results suggest that application of a pinhole to truncate the beam profile may marginally increase the ablation efficiency but

dramatically deteriorates the ablation smoothness for the entire range of overlap distances below ~600μm (corresponding nearly to the size of a single spot). An exception was seen at overlap distances ~400μm, where three profiles collapsed.
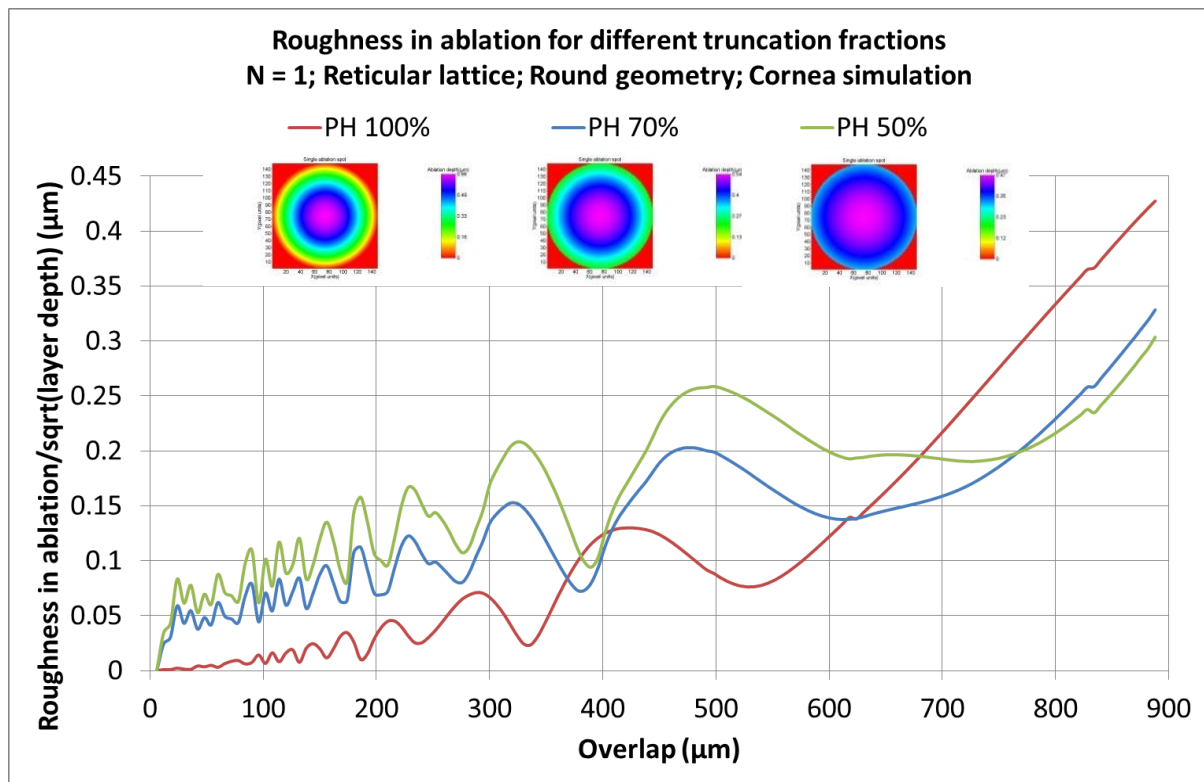
Figure 33. The Roughness in ablation with respect to the varying overlap distances for different truncation fractions. The complete beam profile represented with a truncation fraction of 100%, results in the smoothest ablations. A further truncation of the beam profile increases the roughness in ablation for overlap distances less than 600μm.

Optimum Super Gaussian Order

The results of the simulations are presented in *Figure 34*. The roughness increased for larger values of N. Gaussian profiles theoretically result in smoother ablations, particularly for overlap distances smaller than ~620μm, corresponding nearly to the size of a single spot.
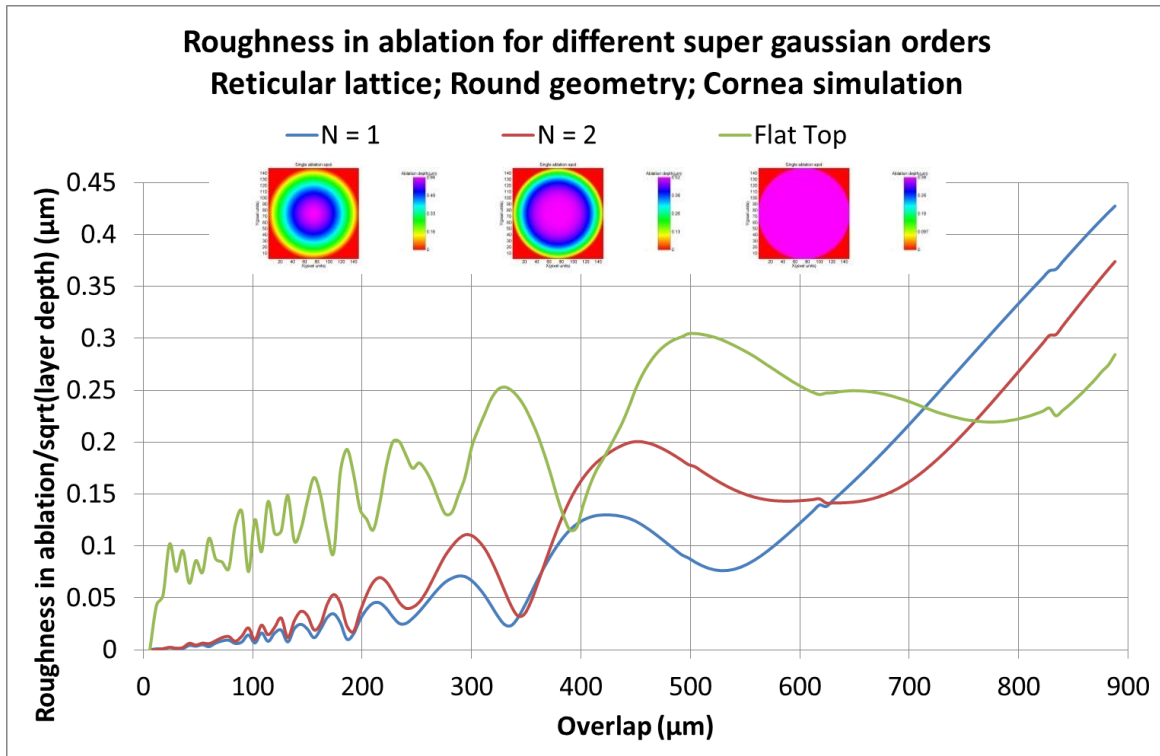
Figure 34. The roughness in ablation with respect to the varying overlap distances for different super Gaussian orders (N). The roughness increases with increasing values of N, particularly for overlap distances smaller than ~620μm.

Optimum Spot Geometry

The results of the simulations are presented in *Figure 35*. Theoretically, round spot geometries produced lower roughness in ablation compared to the square geometry, particularly for overlap distances smaller than ~600μm, corresponding nearly to the size of a single spot.
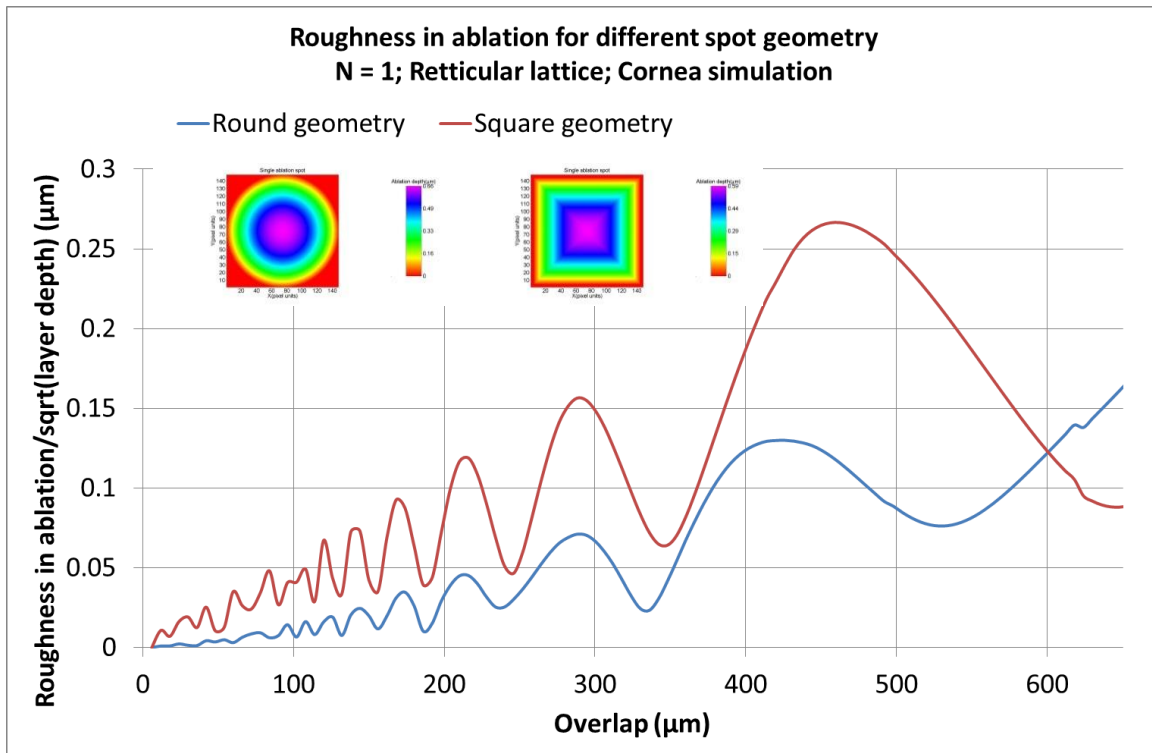
Figure 35. The roughness in ablation with respect to the varying overlap distances for round and square spot geometries. Round spot geometries result in lower simulated roughness in ablation compared to the square geometry, particularly for overlap distances smaller than ~600µm, corresponding nearly to the size of a single spot.

Optimum Lattice Geometry

The results of the simulations are presented in *Figure 36*. For lower overlap distances (<200µm), Triangular lattices shall theoretically produce lower roughness in ablation compared to the reticular lattice. As the overlap distances increase, a shift was seen in the corresponding peaks and valleys in the curve for triangular and reticular lattice, with triangular lattice achieving its corresponding peaks and valleys (in terms of the roughness in ablation), at smaller overlap distances compared to the reticular lattice. This suggests that at higher overlap distances, triangular lattice results in lower roughness in ablation compared to the reticular lattice.
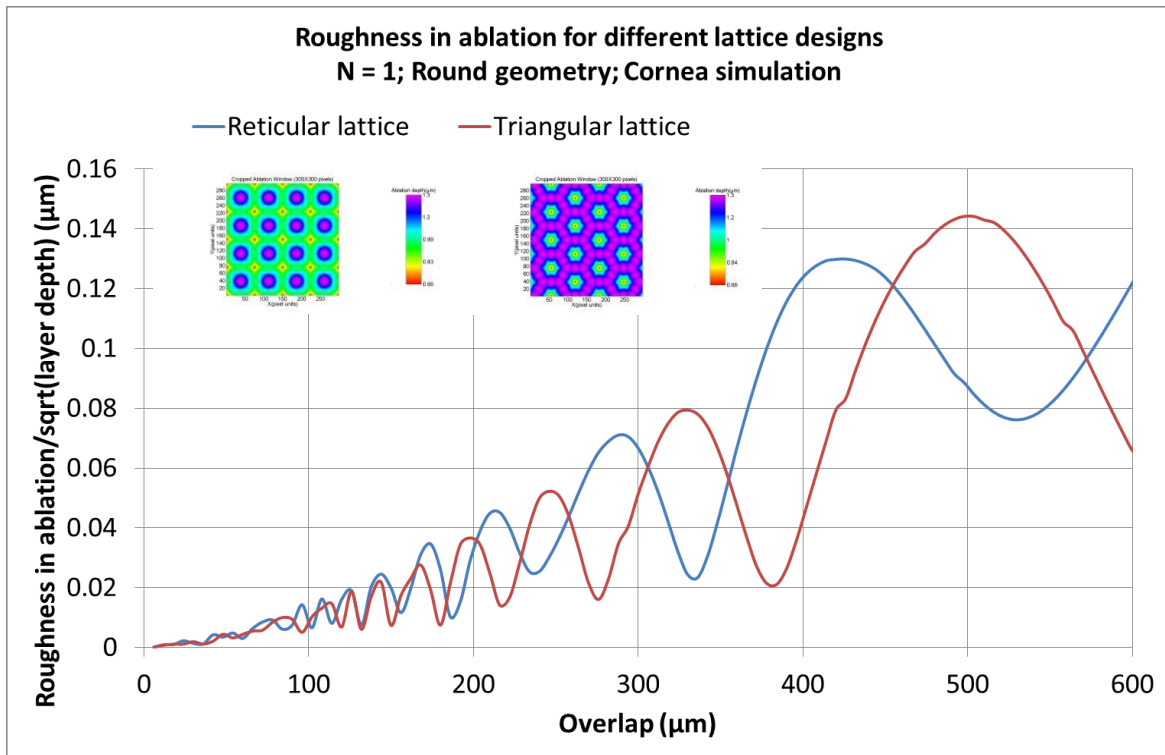
Figure 36. The roughness in ablation with respect to the varying overlap distances for Reticular and Triangular lattice geometries. For lower overlap distances (<200µm), Triangular lattices resulted in lower simulated roughness in ablation compared to the reticular lattice. As the overlap distances increase, a shift can be seen in the corresponding peaks and valleys in the curve for triangular and reticular lattice.

Measured vs. theoretically modeled beam profile

The simulated roughness in ablation for the theoretically modelled beam profile was compared to the measured beam profile. This comparison is presented in *Figure 37*. The measured beam profile corresponded well with the theoretically modelled beam for the entire range of overlap distances; however the modelled beam profile showed comparatively lower roughness in ablation in general.
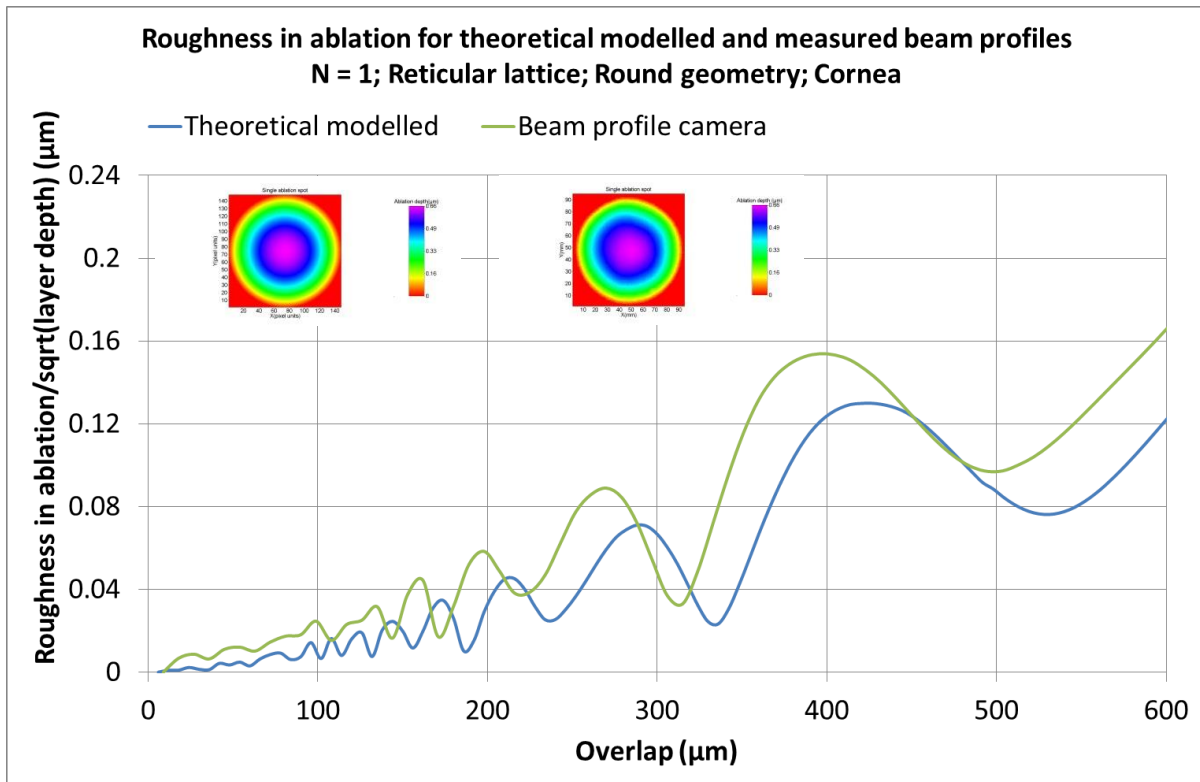
Figure 37. The roughness in ablation with respect to the varying overlap distances for theoretically modelled and measured beam profile (using beam profile camera). In general, the theoretically modelled beam profiles result in lower simulated roughness in ablation compared to the measured beam profile. Good correspondence was observed between the two beam profiles for the entire range of overlap distances.

Impact of ablation material

The results of the simulations are presented in *Figure 38*. The simulated roughness in ablation on PMMA tends to be lower than on the human cornea, although correspondingly, lower ablation volumes are also associated with PMMA. For a window of overlap distances (90-150µm), the correspondence between PMMA and cornea was very good in terms of the roughness in ablation (indicated with a green window in *Figure 38*). As the overlap distances increase, a shift was seen in the corresponding peaks and valleys in the curve of PMMA and cornea.
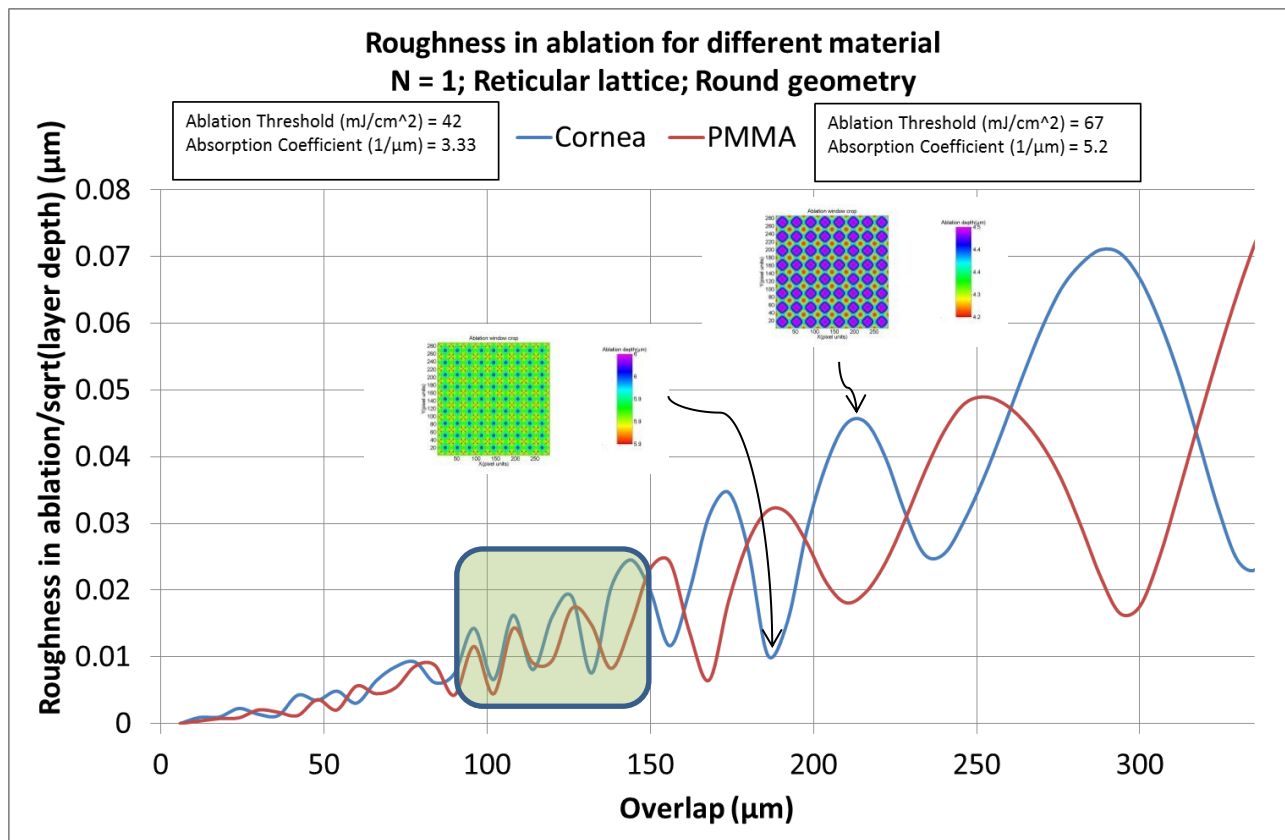
Figure 38. The roughness in ablation with respect to the varying overlap distances for human cornea and PMMA (polymethylmethacrylate). The simulated roughness in ablation on PMMA tends to be lower than on the human cornea. For a window of overlap distances (90-150µm), high correspondence is seen between PMMA and cornea in terms of the roughness in ablation (indicated in green).

Impact of Spot Energy and Spot Diameter

The results of the simulations are presented in *Figure 39* and *Figure 40*. The roughness in ablation was lower for lower energy and larger spot sizes. This suggests that for smoother flat ablations, lower spot energy and larger spot sizes should be preferred. However, this would limit the lateral resolution that is imperative to ablate the fine shapes needed in higher order correction in refractive surgery.
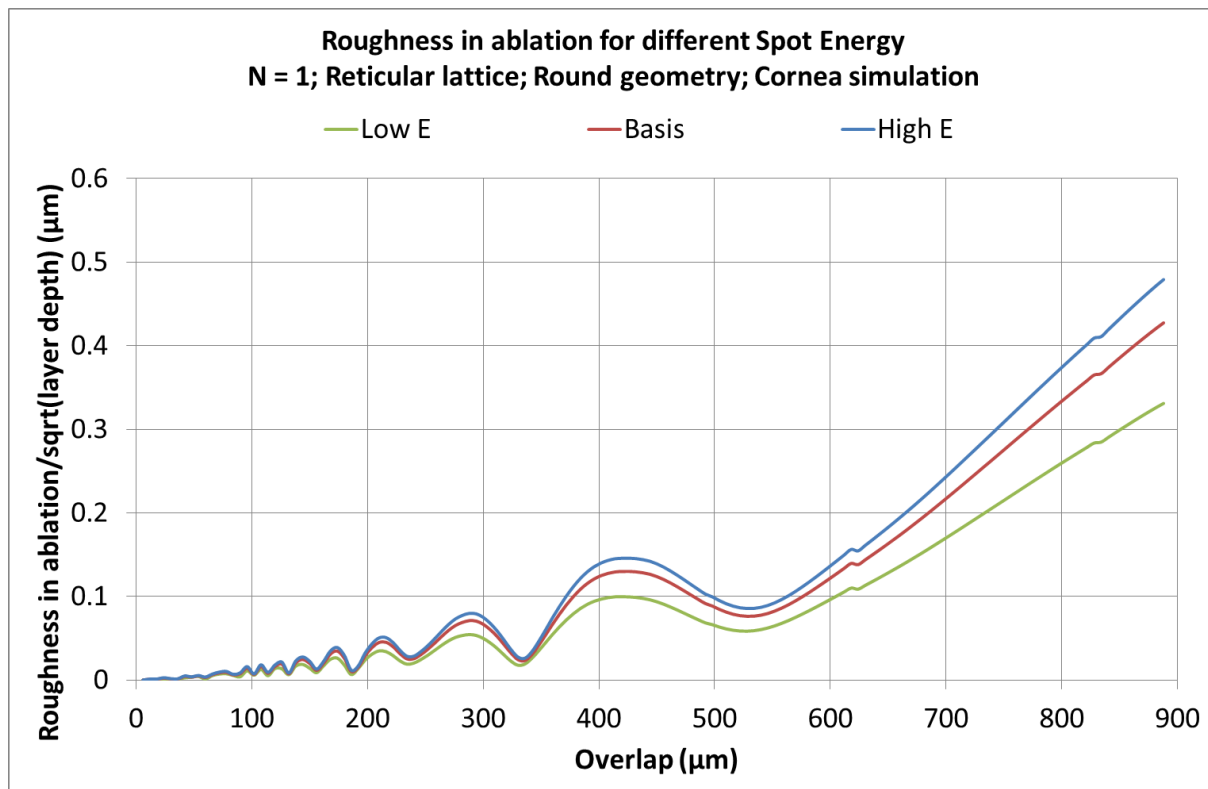
Figure 39. The roughness in ablation with respect to the varying overlap distances for different energy settings presented in Table 10. Here, Low E represents a spot energy of 0.53mJ, Basis represents the standard test setting (Table 7, spot energy = 0.95mJ) and High E represents a spot energy of 1.40mJ. The roughness in ablation tends to be lower for lower values of spot energy, and increases as the values of spot energy increases, for the complete range of overlap distances.
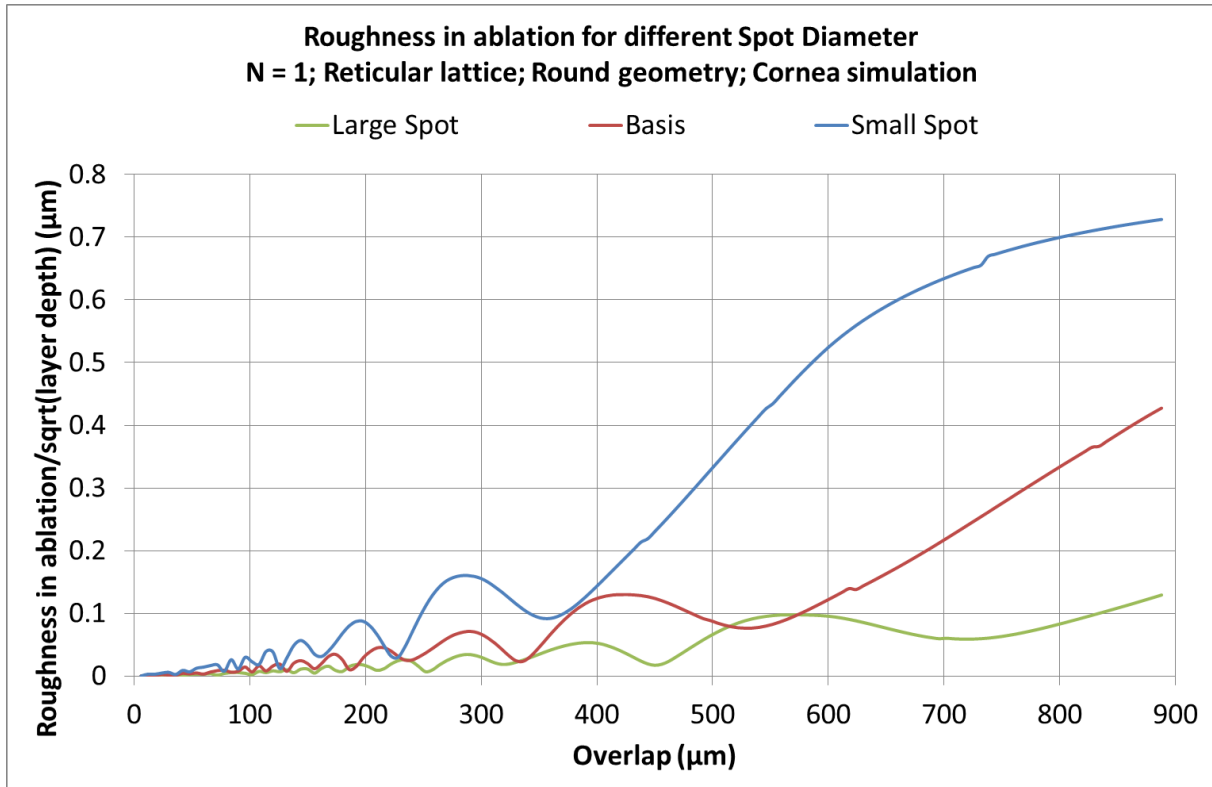
Figure 40. The roughness in ablation with respect to the varying overlap distances for different spot diameters presented in Table 11. Here, Large Spot represents a spot diameter of 1.20mm, Basis represents the standard test setting (Table 7, spot diameter = 0.89mm) and Small Spot represents a spot diameter of 0.60mm. The roughness in ablation tends to be lower for larger spot diameters, and increases as the values of spot diameter decreases, for the complete range of overlap distances, barring the exception of few overlap distances where all the three curves collapse giving a similar roughness.

Perturbation Analysis

The results of the perturbation analysis are presented in *Figure 41*. With respect to the standard test settings (*Table 7*), the simultaneous perturbation in the input parameters, including the spot overlap distances represents more realistic results expected in the real world. According to the expectations, the simulated roughness in ablation with the perturbed input parameters, followed a similar but very jittery progression as the standard test settings. However, unlike the standard test settings, for the overlap distances below 300µm, the simulated roughness remained closer to 0.1µm and did not systematically reduce to zero roughness. This suggests that in the real world settings, minimum roughness in ablation shall be achieved at an overlap distance of 300µm, and an overlap distance below 300µm shall not detrimentally affect the roughness in ablation.
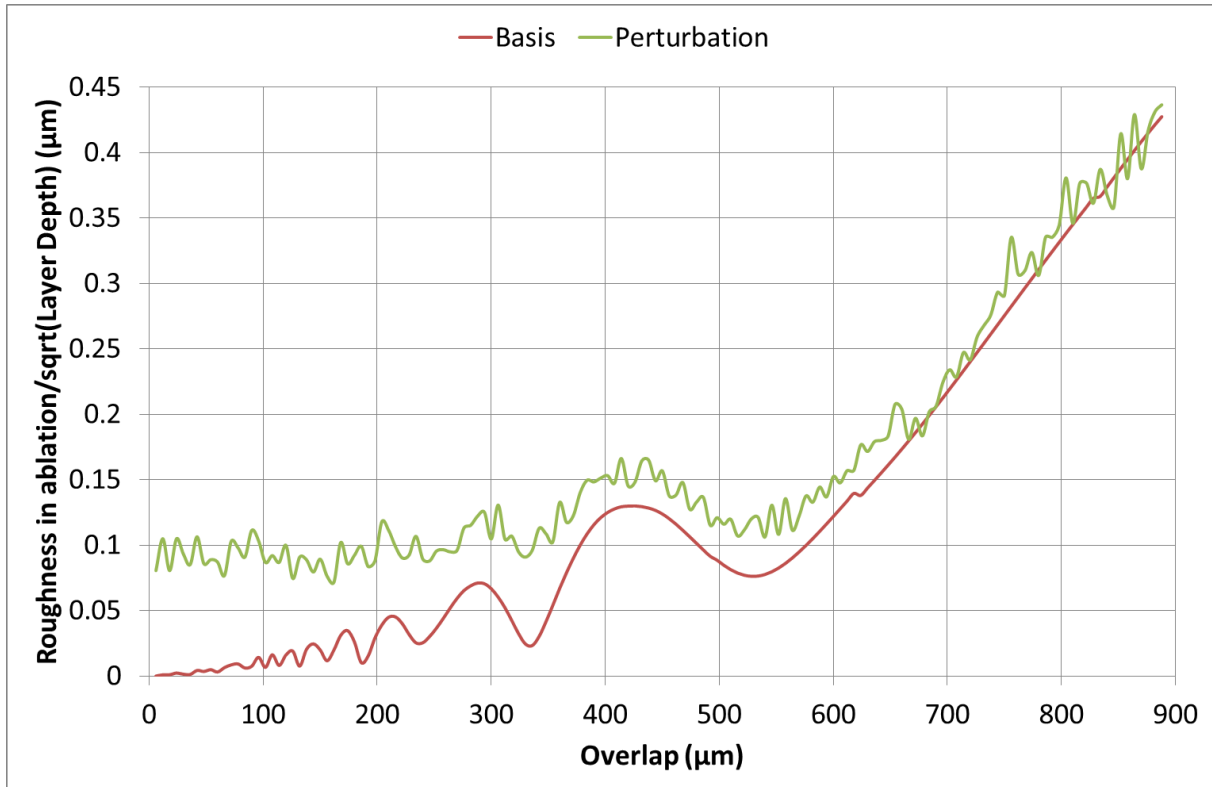
Figure 41. The roughness in ablation with respect to the varying overlap distances, for the standard test setting (Table 7) compared to the outcomes with the perturbed input parameters. The simulated roughness in ablation with the perturbed input parameters, followed a similar but very jittery progression as the standard test settings. For the overlap distances below 300µm, the simulated roughness remained closer to 0.1µm and did not systematically reduce to zero roughness.

Proper Optimum for minimum roughness in ablation

For the input parameters presented in *Table 7*, a proper optimum configuration for minimizing the roughness is summarized in *Table 17*. The optimum overlap distances correspond to the valleys in *Figure 36* (Reticular lattice), that is, 96µm, 120 µm, 132µm. However, considering the outcomes of the perturbation analysis, any spot overlap below 300µm would result in minimum roughness in ablation given the variability in relevant parameters, observed in a realistic setting.

Parameter	Optimum Value for lower roughness
Optimum truncation diameter	PH = 100% (No Truncation)
Optimum Super Gaussian Order	N = 1
Optimum Spot Geometry	Round Spot
Optimum Lattice Geometry	Triangular Lattice
Overlap Distances (µm)	96, 120, 132 (Theoretical optimum) <300µm (based on Perturbation analysis)
Optimum Spot Energy	Lower Energy (0.53 mJ)
Optimum Spot Diameter	Large spot (Foot print = 1.20mm)
Impact of absorption coefficient and threshold of the irradiated tissue or material (α, Ith)	PMMA lower than cornea
Modelled beam vs. Measured beam profile	Model beam profile

Table 17. Proper Optimum: A proper optimum configuration for minimizing the roughness in ablation, for the input parameters presented in Table 7. It is assumed that the combination of individual optima represents an optimum for the given conditions.

3.5 **TOPIC E**: Determination of optimum laser beam characteristics: Empirical Evaluation

The modelling and optimization in the simulation environment was followed by experiments to give empirical evidence for the impact of laser beam characteristics on residual roughness after ablation, with an excimer laser system. In general, truncation of the beam is negatively associated to a higher level of residual roughness; ordered dithering to select the optimum pulse positions is positively associated to a lower level of residual roughness; jitter is negatively associated to a higher level of residual roughness. The effect of dithering was the largest, followed by truncation, and jitter had the lowest impact on results. So that: dithering approaches help to further minimize residual roughness after ablation; minimum (or no) truncation of the beam is essential to minimize residual roughness after ablation; and jitter shall be avoided to minimize residual roughness after ablation.

Mean Performance

Performance for all 8 test settings is displayed in *Figure 42* (Left), whereas cumulative effect of pinhole, dithering and jitter is displayed in *Figure 42* (Right). The absence of pinhole enhanced performance by +4% (p<.005); the use of ordered dithering enhanced performance by +3% (p<.01); and the absence of jitter enhanced performance by +1% (p<.05).
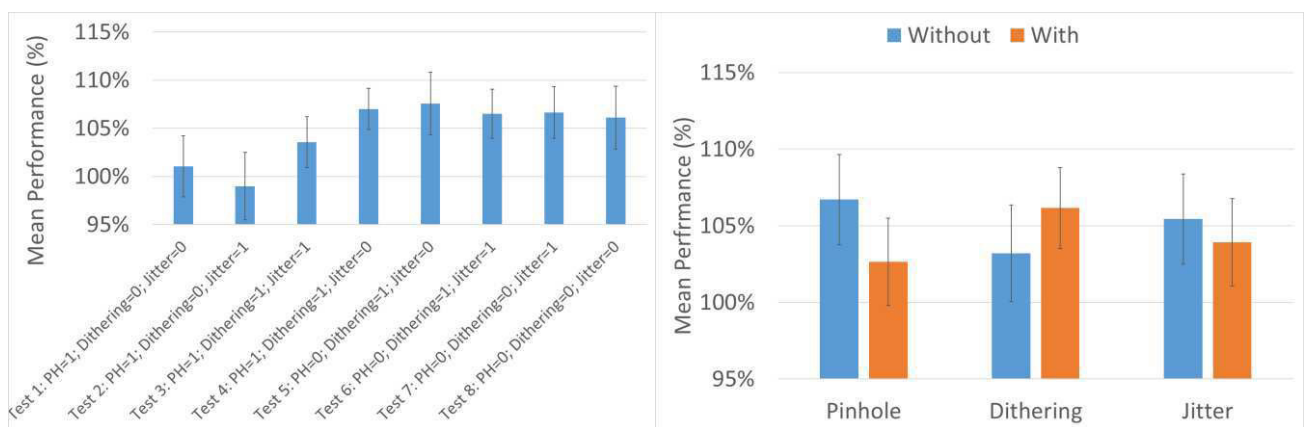
Figure 42. Mean performance measured for each test condition, ranging from 99% to 108% (left). 4 vs. 4 cumulated comparison of the effects of pinhole, dithering, and jitter on mean ablation performance on PMMA (right). The absence of pinhole enhanced performance by +4% (p<.005); the use of ordered dithering enhanced performance by +3% (p<.01); and the absence of jitter enhanced performance by +1% (p<.05).

Roughness

Roughness for all 8 test settings is displayed in *Figure 43* (Left), whereas cumulative effect of pinhole, dithering and jitter is displayed in *Figure 43* (Right). The absence of pinhole reduced roughness by -8% (p<.00005); the use of ordered dithering reduced roughness by -11% (p<.00001); and the absence of jitter reduced roughness by -4% (p<.0005).
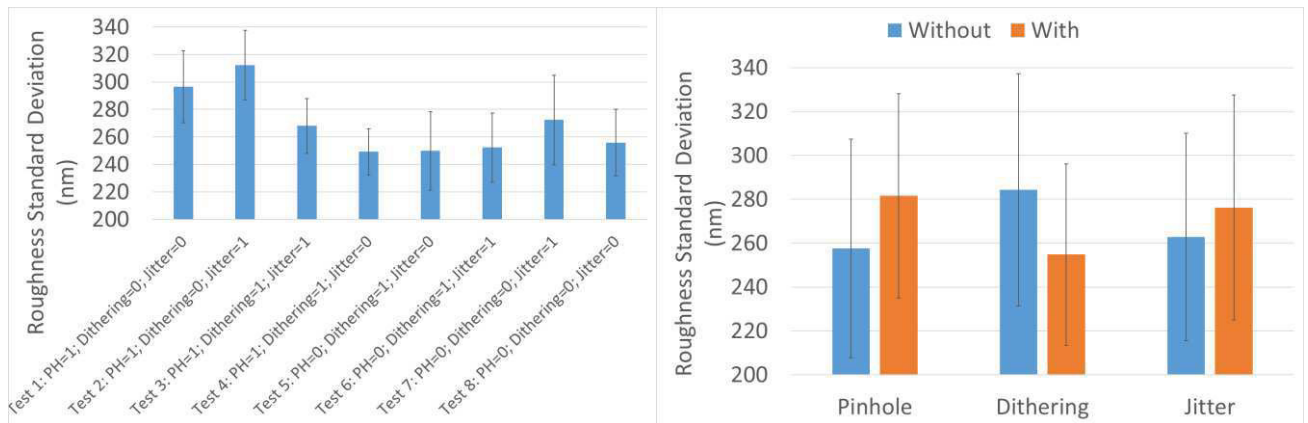
Figure 43. Residual roughness measured for each test condition, ranging from 160nm to 427nm (left). 4 vs. 4 cumulated comparison of the effects of pinhole, dithering, and jitter on residual roughness on PMMA (right). The absence of pinhole reduced roughness by -8% (p<.00005); the use of ordered dithering reduced roughness by -11% (p<.00001); and the absence of jitter reduced roughness by -4% (p<.0005).

Roughness versus ablation depth

The relationship roughness (in the form of sum of the squared residuals) vs. maximum ablation depth is displayed in *Figure 44* for Pinhole (left), Dithering (middle), and Jitter (right). It followed a power function, with an exponent ~1.4-1.5 with maximum ablation depth providing reasonable $R^2>0.8$. The best fit lines confirm that the absence of pinhole, the use of ordered dithering, and the absence of jitter all reduced roughness.
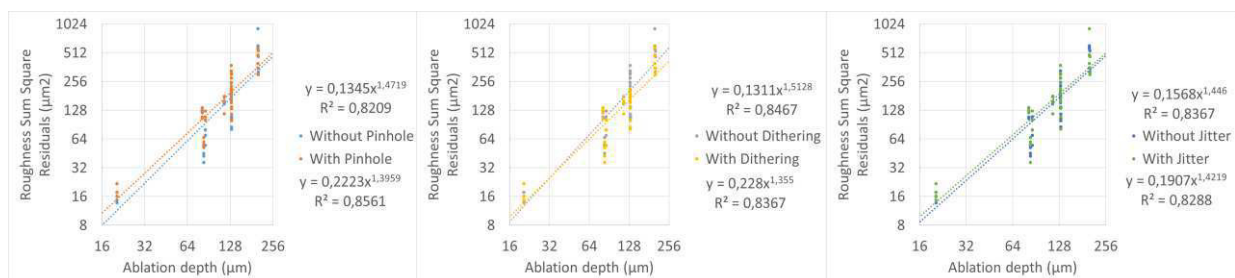
Figure 44. Roughness (expressed as the sum of squared residuals) versus maximum ablation depth in a 4 vs. 4 cumulated comparison of the effects of pinhole (left), dithering (middle), and jitter (right). It follows a power function, with an exponent ~1.4-1.5 with maximum ablation depth providing reasonable R2>0.8. The best fit lines confirm that the absence of pinhole, the use of ordered dithering, and the absence of jitter all reduced roughness.

Pairwise comparisons

Pairwise comparisons are shown in *Table 18*. The pairwise comparisons confirm that for all but one case the absence of pinhole, the use of ordered dithering, and the absence of jitter all reduced roughness.

| Pairwise	*Test*	SD	*Counterpart Test*	SD	**Comparison (bold Statistically significant)**
Pinhole	*Test 1: PH=1; Dithering=0; Jitter=0*	297±26	*Test 8: PH=0; Dithering=0; Jitter=0*	256±24	**No PH better**
	Test 2: PH=1; Dithering=0; Jitter=1	312±25	*Test 7: PH=0; Dithering=0; Jitter=1*	272±32	**No PH better**
	Test 3: PH=1; Dithering=1; Jitter=1	268±20	*Test 6: PH=0; Dithering=1; Jitter=1*	252±25	No PH better
	Test 4: PH=1; Dithering=1; Jitter=0	249±17	*Test 5: PH=0; Dithering=1; Jitter=0*	250±28	PH better
Dithering	*Test 3: PH=1; Dithering=1; Jitter=1*	268±20	*Test 2: PH=1; Dithering=0; Jitter=1*	312±25	**Dithering better**
	Test 4: PH=1; Dithering=1; Jitter=0	249±17	*Test 1: PH=1; Dithering=0; Jitter=0*	297±26	**Dithering better**
	Test 5: PH=0; Dithering=1; Jitter=0	250±28	*Test 8: PH=0; Dithering=0; Jitter=0*	256±24	Dithering better
	Test 6: PH=0; Dithering=1; Jitter=1	252±25	*Test 7: PH=0; Dithering=0; Jitter=1*	272±32	**Dithering better**
Jitter	*Test 2: PH=1; Dithering=0; Jitter=1*	312±25	*Test 1: PH=1; Dithering=0; Jitter=0*	297±26	**No Jitter better**
	Test 3: PH=1; Dithering=1; Jitter=1	268±20	*Test 4: PH=1; Dithering=1; Jitter=0*	249±17	**No Jitter better**
	Test 6: PH=0; Dithering=1; Jitter=1	252±25	*Test 5: PH=0; Dithering=1; Jitter=0*	250±28	No Jitter better
	Test 7: PH=0; Dithering=0; Jitter=1	272±32	*Test 8: PH=0; Dithering=0; Jitter=0*	256±24	**No Jitter better**

Table 18. Pairwise comparisons: the absence of pinhole, the use of ordered dithering, and the absence of jitter all reduced roughness.

Best-Worst comparisons

The rank of residual roughness is shown in Table *19*. The worst condition was test setting 2 (with pinhole, without dithering, with jitter) as exactly predicted by *Figure 43* and *Figure 44* (and *Table 18*). Its counterpart, derived as best from figures *Figure 43* and *Figure 44* (and *Table 18*) would be test setting 5 (without pinhole, with dithering, without jitter), but the actual empirical best condition was Test setting 4 (with pinhole, with dithering, without jitter). These 3 settings are displayed and analyzed in *Figure*

45. There was no statistically significant difference in roughness between test settings 4 and 5 (empirical best vs. predicted best) (difference in roughness 0.1%; p=.5). There was a clear statistically significant difference in roughness between test setting 2 and test settings 4 and 5 (worst vs. best) (difference in roughness +24%; p<.00001). The same holds for the relationship roughness (in the form of sum of the squared residuals) vs. maximum ablation depth, which is largely overlapped for test settings 4 and 5 (best), and distinctly higher for test setting 2.

Rank	Test
1	Test 4: PH=1; Dithering=1; Jitter=0
2	Test 5: PH=0; Dithering=1; Jitter=0
3	Test 6: PH=0; Dithering=1; Jitter=1
4	Test 8: PH=0; Dithering=0; Jitter=0
5	Test 3: PH=1; Dithering=1; Jitter=1
6	Test 7: PH=0; Dithering=0; Jitter=1
7	Test 1: PH=1; Dithering=0; Jitter=0
8	Test 2: PH=1; Dithering=0; Jitter=1

Table 19. Rank for the residual roughness on PMMA.
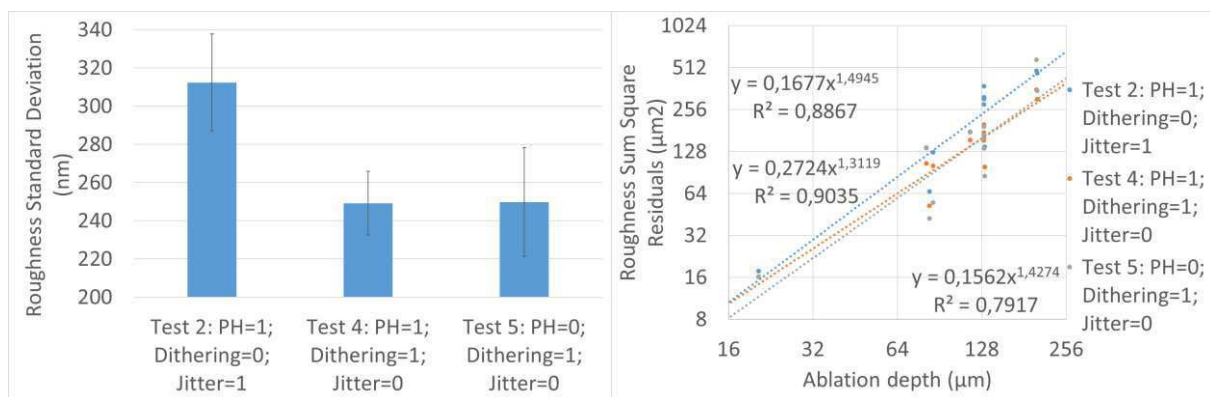
Figure 45. Worst-Best comparisons: the absence of pinhole, the use of ordered dithering, and the absence of jitter all reduced roughness. There was no statistically significant difference in roughness between test settings 4 and 5 (empirical best vs. predicted best) (difference in roughness 0.1%; p=.5). There was a clear statistically significant difference in roughness between test setting 2 and test settings 4 and 5 (worst vs. best) (difference in roughness +24%; p<.00001). The same holds for the relationship roughness (in the form of sum of the squared residuals) vs. maximum ablation depth, which is largely overlapped for test settings 4 and 5 (best), and distinctly higher for test setting 2.

Summary

For the input parameters presented in *Table 13*, a proper optimum configuration for minimizing the roughness is summarized in *Table 20*.

Conditions without Jitter//with Jitter=20µm	**0.7m pinhole and 0.75mJ energy**	**No pinhole and 0.9mJ energy**
Heuristic reticular search	Baseline (100% residual roughness)//+5%	-8%//-4%
Ordered dithering search	-11%//-7%	-18%//-14%

Table 20. Consolidated summary of the results

4 DISCUSSION

4.1 **TOPIC A and TOPIC B**: *Can we quantify and compensate for the influence of environment conditions on refractive procedures?*

A critical interplay exists between several factors affecting the corneal temperature and hydration during the refractive surgery, namely geographical location and patient lifestyle[220,221,222], fluid distribution, photoablation time, temperature[128] etc.

Several groups have tested the impact of hydration and room temperature in human eyes undergoing refractive surgery, reporting different influence on post-ablation outcomes[223,224]. In a retrospective chart review comprising 368 consecutive eyes of 191 myopic patients who had laser in situ keratomileusis (LASIK) by the same surgeon, Walter and Stevenson determined whether environmental factors affect LASIK enhancement rates (the percentage of people undergoing a secondary procedure to improve surgery outcomes)[225]. Using univariate and multivariate analysis, they found that LASIK enhancement rates strongly correlated with procedure room humidity, 2-week preparative mean outdoor humidity, outdoor temperature, and age; suggesting that these factors should be taken in to account while planning the LASIK procedure. In another study, a modified LASIK procedure was performed on the corneal surface that was kept relatively dry by blotting of the stromal surface between sets of laser pulses[226]. A group of 36 eyes undergoing the modified LASIK procedure was compared to a group of 40 eyes undergoing normal LASIK procedure. It was reported that for less hydrated corneas, ablation effects were greater than for corneas not blotted during the procedure, but these patients appeared to undergo greater myopic regression. Contrary to these results, studies with other laser platforms could not demonstrate any significant difference in patients grouped according to season at time of treatment[227].

The results of our large scale retrospective cross sectional study demonstrated a cyclic winter-summer variation in PMMA ablation using the SCHWIND AMARIS lasers. The correspondence between nominal laser pulses (determined on PET) and the nominal single laser pulse fluence (determined on PMMA) may indicate that the underlying effect is not arising from the ablation material but from the laser system itself. Furthermore, our results were consistently confirmed in the seasonal as well as monthly analyses showing a very comparable trend. Although, all the ablations were performed with laser systems under stable room conditions and only minor seasonal differences in relative humidity, yet differences in performance could be observed. Since the recorded room temperature and relative humidity remained almost constant throughout the entire duration of testing (21°C-24°C (21°C-22°C in winter and 23°C-24°C in summer) and 30%-50% Relative humidity (30%-40% in winter and 40%-50% in summer)), this may indicate that not only the room temperature and relative humidity plays a role in influencing the laser system performance, but also other factors may be involved like the air circulation which may be affected with the seasonal variations (blowing hot air in wintertime vs. Cold air and dehumidifying in summertime).

Through the results obtained during the experiments in the climate chamber, we could establish a well-fitting multi-linear model to estimate the impact of changes in temperature and relative humidity on laser energy, fluence, and ablation efficiency on PMMA and tissue. According to this model, time was a significant predictor for all

output parameters, except for refractive change achieved on porcine cornea, suggesting that the system performance changed significantly with time. One possible explanation for this could be that the rapidly changing room environment conditions affected the performance of the laser system dramatically. In order to analyze the impact of temperature and humidity, independently, and eliminate the influence of time, the time was taken out as a covariate in our analysis. This can be regarded as a limitation of the ablation model.

There are some further limitations to our work; unlike the cross-section review, the tests in the climate chamber and the resulting ablation model was established based on only one laser system used over a series of days of testing, and under a range of climate conditions. The inter-system variability was not included in our analysis, however, PMMA ablation efficiency being the calibration method for SCHWIND AMARIS laser systems, a comparison of the ablation efficiency in PMMA and porcine corneal tissue was a more critical analysis goal.

Our ablation model, followed multi-linear approximation of the deviations in the normalized data. The deviations in other metrics (like median, averages etc.) were not analyzed. In our methods, we describe the dependencies via a linear approximation. The analysis was repeated for an exponential model which showed very comparable results to the linear approximation. However, due to obtained good correlation, further modelling approaches (exponential, sigmoid etc.) were not tested. In addition, the goodness of the ablation model was tested for a narrow window of parameters, however, surpassing the extremes of the potential working conditions for refractive surgery laser systems. No further conditions were tested to qualify the model and recognize the outliers. An ablation model based on human cornea would be ideal, however our tests were conducted on enucleated porcine eyes; hence, the results shall be extrapolation from porcine to human cornea. The pressure in the eye was subjectively checked by touching the corneal surface with a fingertip instead of an objective measurement through a pressure sensor. During the evaluation of the test set-up prior to the beginning of the tests, it was discovered that using a pressure column to maintain the pressure with an infusion was logistically problematic, for orienting the porcine eyes properly under the laser. A lack of measurement of eye pressure, could have caused variability in the achieved refractive change in the porcine cornea, however, given the number of eyes in the test protocol, it is unlikely that this may induce a systematic bias. Actually, the increased variability may mask a difference as non-significant although there is one, so if at all this may lead to a type II statistical error. The porcine eyes were refrigerated and then were serially placed in the climate chamber, ablated, and discarded. It would have been optimal to have the porcine eyes at normal room temperature and measure the corneal temperature at the time of ablation, in order to precisely determine the effect of temperature and humidity on ablation rate. However, due to the logistical issues and a long test protocol, porcine eyes were refrigerated until being ablated. Nevertheless, this protocol was systematically followed for all the eyes. The porcine eyes were stored in glucose and saline solution until being ablated. No pachymetry data was recorded to evaluate the influence of hydration on the thickness of the corneal tissue. This factor could have even affected the influence of the humidity conditions in the room on to the effective hydration of the cornea. Since fresh porcine eyes were procured and tested on each day, the variability between the days would not be as critical, compared to the changes throughout the day as the eyes are being stored in the solution for nearly 8 hours.

Based on the ablation model, the temperature changes did not affect laser pulse energy, fluence, and ablation efficiency (on PMMA or porcine corneal tissue) significantly. This was confirmed by the surface plots shown in Figure 23 and Figure 24. A diagonal trend was observed in surface plots shown in Figure 25 and Figure 26, showing an influence of the temperature change, although not achieving statistical significance ($p = .33$ for PMMA and $p = .17$ for Porcine cornea, although lowest of all the parameters predicted by the temperature change yet $p > .05$). Changes in relative humidity were more critical and significantly affected the laser pulse energy, high fluence and low fluence, however, these changes did not significantly show up in the ablation efficiency on PMMA and porcine cornea. As per the design of SCHWIND AMARIS, the output of PET ablations calibrates the PMMA ablations in the short term (interval of 2 hours). Therefore, the internal compensation of SCHWIND AMARIS (preset energy, pulses) could be a factor for reducing the influence of temperature and relative humidity on PMMMA and porcine to a non-significant impact. In any modern commercially available refractive laser system, calibration cycles are repeated at different frequencies depending on the frequency of the system feedback[109]. In one form or another, since all laser systems follow the same principle of short term calibration, the results of our tests on PMMA and porcine cornea, and their inter-relationship would still remain valid.

Model simulations have shown that laser energy absorption (up to 7% of the available energy) occurs along the path of laser beam, into the existent space between the laser beam source and the patient's eye, due to the environmental temperature and relative humidity. In comparison, our results suggest laser energy absorption of 10-14% in the range of tested climate conditions. Theoretical model of the water vapor absorption at 193 nm wavelength have been proposed in order to quantitatively assess the influence of environmental parameters on the laser energy that actually reaches the corneal surface.[228,140].

Similar conclusions regarding the influence of temperature and humidity on refractive outcomes were presented in a study with 237 patients who underwent LASIK, between May 1999 and March 2000.[229] The results at 15 and 60 days after LASIK were compared according to different levels of temperature and humidity in the operating room during the procedure. The linear regression coefficient showed that lower temperature levels were associated with lower spherical equivalent refractions at 60 days after LASIK. The evaluation of humidity indicated an influence at 15 days after LASIK, as well as at 60 days, suggesting a higher significance of operating room humidity compared to the temperature.

In our results, moist climate conditions resulted in lower single pulse energy, this could be due to higher UV absorption in moist air present in the environment. Similarly, reduced ablation efficiency was recorded on porcine corneal tissue, at low temperatures and high humidity.

Comparison of PMMA ablation to porcine cornea tissue

Plastic models based on PMMA are readily used for calibration of the laser system, but PMMA ablation may also be equally affected by the variations in temperature and humidity. A comparison of PMMA and porcine corneal tissue in terms of the influence of temperature and relative humidity, for all the points in the 4X4 matrix of input values

of predictive factors (Table 16) is presented in Figure 46. An opposite trend was observed between the performance on PMMA and porcine cornea.

PMMA	18°C	22°C	26°C	30°C	Defocus	18°C	22°C	26°C	30°C
20	101%	100%	99%	98%	20	100%	102%	104%	106%
40	101%	101%	100%	99%	40	98%	100%	102%	103%
60	102%	101%	101%	100%	60	95%	97%	99%	101%
80	103%	102%	101%	101%	80	93%	95%	96%	98%

Figure 46. A comparison of PMMA and porcine corneal tissue in terms of the influence of temperature and relative humidity, for all the points in the 4X4 matrix of input values of predictive factors.

The results of the large scale retrospective cross sectional review documented here, can be compared with the clinical results from Luger et al.[169], who used the same laser platform to analyze the effect of seasonal changes in residual refraction in 5740 consecutive treatments, one year after corneal refractive surgery. With this comparison, one can investigate the relationship between laser ablation of PMMA and human corneal tissue. This comparison also confirms the opposite trends followed by PMMA and corneal tissue ablation under different seasonal conditions. However, the ranges or maximum deviation in performance observed in this large scale retrospective cross sectional review are wider than the results presented by the climate chamber tests; especially considering the controlled room conditions with subtle seasonal changes during production, compared to the forced extreme conditions in the climate chamber tests (temperature ~18°C to ~30°C and relative humidity ~25% to ~80%).

This finding of an opposite trend in performance of PMMA and tissue confirmed through two independent analysis methods, is counterintuitive, as principally, the behavior on calibration material is expected to follow the same trend as tissue ablation. Further explorations are needed to explain this findings, but a potential explanation may be that PMMA has a much lower water content than the cornea, therefore, PMMA regardless of the tested setting tends to moist (faster for larger humidity differences), while cornea regardless of the tested setting tends to dry out (faster for larger humidity differences). Nevertheless, these opposite trends may amplify each other, since calibrating in dry and hot conditions would make the laser underperform on PMMA, which after potentially being adjusted to 100%, would result in over-performance on porcine cornea in dry and hot conditions. In the most extreme case, such a calibration may lead to an over-correction of 8% (2 % adjustment due to PMMA calibration at 30°C and 80%RH, increasing the correction on porcine cornea from 6 to 8%, Figure 46) on porcine cornea, or conversely an under-performance on PMMA by the same amount.

It must be also pointed here, that principal diagonal in PMMA and porcine tissue surface plots (Figure 25 and Figure 26, dry-hot to humid-cold), represents a "90° shift" from the summer-winter diagonal (typically going from hot-humid to cold-dry and vice-versa). Therefore, in reality the laser system shall be unlikely subjected to such an extreme change in the climate.

As shown in the results of the climate chamber tests, the effect of both temperature and relative humidity accounted for a deviation of +/-2.5% in PMMA. Assuming the same maximum deviation of +/-2.5% in refractive change in porcine cornea, a working window of climate settings can be defined for an optimum operation of the laser system. This is presented in Figure 47.
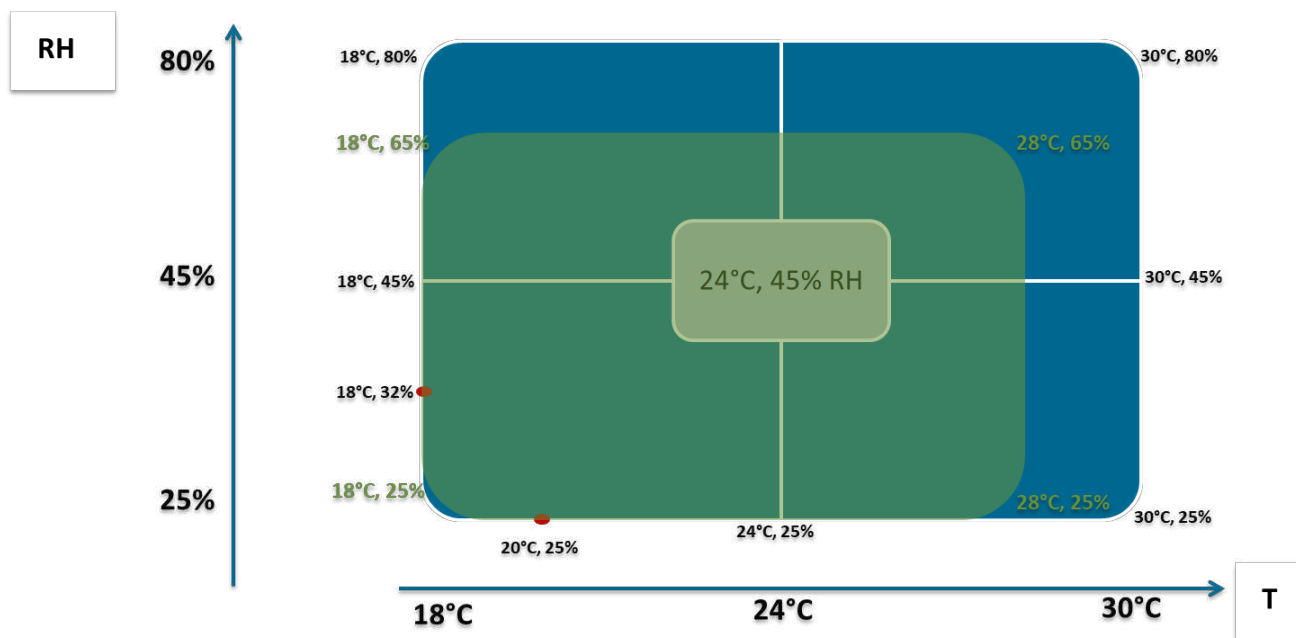
Figure 47. Definition of a working window of climate settings for an optimum operation of the laser system, with a maximum deviation of +/-2.5% in ablation efficiency in PMMA and porcine corneal tissue.

4.1.1 Outlook

A cross sectional analysis is generally limited in analyzing behavior over a period of time, furthermore to determine a cause and effect relationship. It is only effective when it represents the entire population and has a large enough sample size to provide accuracy. We analyzed the ablation performance with only SCHWIND AMARIS laser platform, with all the three commercially available models combined in a single cohort. This can be limiting in providing conclusive evidence for the influence of seasonal changes on excimer lasers in general. However, due to the longitudinal nature of the study lasting six years, and analyzing a large number of AMARIS systems, a scientific conclusion can be drawn with reasonable confidence for the AMARIS laser platform.

This work can be expanded to other laser platforms to draw more global conclusions covering a broader spectrum. Furthermore, it would have been interesting to correlate our findings with the actual room conditions (temperature, humidity, air flow etc.) however, due to the retrospective nature of this study, this data could not be extracted for further analysis. This aspect can be also included in another analysis planned accordingly, but this may presumably last many years to match the number of lasers analyzed here.

Finally, the seasonal variations have shown to influence both the ablation efficiency on corneal tissue and calibration material like PMMA. The underlying mechanism for the observed variations, remains unexplained and warrants further exploration. The influence on ex-vivo porcine corneal tissue was empirically tested here, while the comparison to clinical results in humans was drawn by the results published in the literature. Ideally, the performance of several commercially available laser platforms on ablation material, compared to post-operative results and the laser characteristics, analyzed under a global multi-center long term study could validate our findings, and provide more insights on the topic. Similarly, the analysis should be expanded beyond the application of excimer lasers in refractive surgery, and could also evaluate the influence on other popular modalities using Femtosecond laser applications, like SMILE[230].

4.2 **TOPIC C, TOPIC D and TOPIC E**: *Can we quantify the influence of post-ablation roughness on vision and perception, and optimize refractive procedures for a minimum post-operative roughness?*

While the published work has been focused on comparison of laser delivery methods, beam profiles and calibration materials and their influence on ablation smoothness, an analysis of the impact of residual roughness associated with laser ablation on image perception has not been extensively pursued. In this work, we proposed a method to convert the residual roughness in ablation to its perception in polychromatic vision. The residual roughness in the cornea after the laser ablation process was simulated as random or filtered noise added to the wavefront. The signal included the 2-4th Zernike orders, while noise used 7-8th Zernike orders. In order to test the robustness of this method, three different set of randomly generated higher order (7-8th) Zernike coefficients resulting in a RMS of 0.25µm were fit to a 6mm fit diameter, and the resulting wavefronts were compared in terms of the simulated retinal image quality and image quality metrics VSOTF and Strehl ratio (Figure 48). The simulations showed similar simulated images resulting in comparable image Strehl ratio, suggesting the robustness of the employed method in terms of this metric. The metric VSOTF however showed more variations.

Case 2; Signal = 0; 0.25µm RMS (Random); Pupil = 6mm VSOTF = 0.075 ; Strehl = 0.03	Case 2b; Signal = 0; 0.25µm RMS (Random 2); Pupil = 6mm VSOTF = 0.115 ; Strehl = 0.035	Case 2c; Signal = 0; 0.25µm RMS (Random 3); Pupil = 6mm VSOTF = 0.06 ; Strehl = 0.024

Figure 48. Simulated retinal image and image quality metrics of three wavefronts comprising different set of randomly generated higher order (7-8th) Zernike coefficients as noise (RMS of 0.25µm) fit to a 6mm fit diameter.

Quantification of expected benefit and visual performance is based on different metrics generally grouped under the name of Visual Strehl (VS) related with wavefront error, optical transfer function, point spread function and correlation with templates. The variety of different criteria bear witness to the difficulty of the task. In our methods, the quality of simulated retinal image was quantified using the image quality metric VSOTF and Strehl Ratio. The metric visual Strehl calculated using the OTF method (VSOTF) was chosen since it has been reported as the best single — value metric in a study, for predicting how a change in aberration affects high-contrast logMAR visual acuity. The visual Strehl has been shown to account for 81% of the average variance in high-contrast logMAR visual acuity[117]. However, the suitability of VSOTF as an analysis

metric for our methods, with simulations involving higher order aberrations can still be questioned. Although VSOTF has been considered as a benchmark metric to quantify the image perception quality[117], several authors point out that this criterion is better suited to symmetrical aberrations as opposed their high order counterpart. In fact it is considered that when working with non-symmetrical aberrations it is better to use metrics that emphasize the relevance of the Optical Transfer Function, especially when searching for correlations with letter identification and predicting visual acuity[231,232].

Arines et al.[231] compared VSOTF and the criterion suggested by Young et al[233] called Visual Strehl Combined (VSCombined) with numerical simulations and experimental data. They found that the VSOTF predicted the non-visibility of the letters presenting very small values (also observed in our simulations), similar to those of 2D out of focus images, although they were readable. In contrast, the VSCombined showed better correlation with the visual experience of the letters. While VSOTF provides information about the effect of contrast reduction due to aberrations, VSCombined weighs the effect of phase reversal and PTF modulation on final image quality. It is difficult to establish a clear criterion to assess the performance of extended depth of field solutions. VSOTF provides information mainly about the contrast transfer of the evaluated element while VSCombined provides information on the amount of phase difference between the different frequencies transmitted by the system[231]. It is important to quantify not only contrast loss but also Optical Transfer Function when evaluating non-symmetrical phase elements. A Combination of VSOTF and VSCombined would enable evaluation of contrast transfer and changes in Optical Transfer Function, however such a combination image quality metric was not evaluated in our simulations of perception of roughness.

The reference wavelength of 550nm was chosen in our simulations of the retinal image, being the peak of human contrast sensitivity, in order to compare the different test settings for the strongest simulated retinal image. However, typically 840nm is used to measure aberrations in both Hartmann-Shack[215] and Pyramidal sensor[234] based aberrometers. Therefore, our results and methods shall be adjusted for this wavelength and for an application with clinically diagnosed aberrations.

For all the Wavefronts used in the simulations of the retinal image (with the exception of simulation cases 6 and 7), noise (7-8th Zernike orders) was scaled to a predetermined RMS values of 0.25μm. This value was selected being the typical value of corneal Higher Order Aberrations (HOAs) at 6mm for normal eyes[235,236]. Therefore, the same order of roughness was added to the Wavefronts as seen in the natural HOAs. However, it must be noted that the methods presented here, are equally applicable to simulate other levels of corneal roughness. The typical value of ocular spherical aberrations for a 6mm pupil diameter lies between 0-0.1μm[237]; whereas, the typical value of corneal spherical aberrations lies between 0.2-0.3 μm for a 6mm pupil diameter[238]. Spherical aberration valuing 0.15μm was used in the simulation cases, as a compromise close to the typical corneal and ocular values. Our simulations showed an improvement in image quality metrics with the addition of spherical aberrations. This may be originated due to the same sign of defocus and spherical aberrations (both being positive), thus flattening the central part of the wavefront, and improving the central optics in the process.

The subjective image perception and simulated optical image quality can be different. There are several factors like the image perception by the brain[116], and epithelium

masking after refractive surgery[239] which cannot be easily simulated. In a study involving 15 eyes of 15 patients who underwent LASIK, patients were examined for upto 2 years postoperatively[240]. The total corneal thickness remained unaltered, but epithelial hyperplasia was seen at 2 years. Keratocyte density in the anterior stroma and posterior to the flap interface showed a slight decrease during the follow-up. Subbasal nerve density decreased 82% in 5 days after LASIK. In these eyes, corneal remodeling seemed to continue for at least 2 years. Kanellopoulos and Asimellis[241] explained their findings of epithelial thickening after myopic LASIK with their hypothesis that epithelial behavior is related to the biomechanics of the cornea and that a thinned cornea (in cases of large myopic ablation) might be more susceptible to epithelial hyperactivity and regrowth. Conversely, Reinstein et al.[242] suggested that all epithelial thickness changes can be explained by a compensatory mechanism that is driven by the rate of change of curvature of the stromal surface. Vinciguerra et al.[243,244] demonstrated that the initial curvature gradient after excimer ablation predicts the change in tangential curvature over the subsequent 12 months in areas where the initial tangential curvature is the greatest. When the curvature gradient is high, the surface curvature modification remains in progress even months after the ablation.

There are several challenges associated to the analysis of polychromatic images. Wavefront aberration maps are usually only available for just one wavelength, depending on the wavelength of the aberrometer. Therefore, a conversion of wavefront aberration to another wavelengths is necessary for an analysis. Furthermore, convolution approaches can be only utilized for light sources which are spectrally homogenous. For evaluating the impact of aberrations on polychromatic images, a hyperspectral analysis is required. Additionally, the sampling frequency of the spectral power distributions (of image) and pupil functions should be matched. These measures were accounted, however, our methods still present some constraints. We used Zernike coefficients of 7-8th order to simulate noise. This can be conceptually acceptable for simulating random noise, but filtered noise simulated through these Zernike orders may be too coarse compared to the reality. An ideal solution would have been to include more Zernike orders for simulation or to add the filtered noise as a raw (elevation) map, on to the wavefront signal, however, both strategies were not possible in the version of simulation software (IRIS) used in our methods. Nevertheless, the simulation results for filtered noise can be still considered for comparison to the random noise. The scale of the roughness shall be analysed before applying our methods clinically. If the scale of the roughness being analyzed is small compared to the spacing of lenslets in aberrometer sensor, the measured roughness (RMS HOA) and hence the simulated retinal image cannot be trusted.

Modelling approaches have been proposed in the past to study the ablation profiles and outcomes of the refractive surgery excimer lasers[245]. The predicted post-operative corneal ablation shape, ablated volume, asphericity and spherical aberration varies across commercial laser platforms, as well as the relative contribution of ablation pattern designs and efficiency losses to the increased asphericity[246].

There is a delicate balance between the spot energy and spot diameter in terms of the roughness in ablation. Correcting the higher-order aberrations of the eye requires lasers with smaller spots and finer resolution[153]. We modelled the laser beam characteristics to define a set of parameters characterizing the laser beam profile that can optimize the roughness in ablation. Our theoretical analysis of the optimum spot energy and spot sizes, suggested that for smoother flat ablations, lower spot energy

and larger spot sizes should be preferred. However, for achieving the limit of lateral resolution to ablate the fine shapes needed in higher order correction in refractive surgery, a compromise must be made between ablation smoothness and spot characteristics (including spot geometry and energy). This compromise is reflected in the standard test settings used here (Spot Energy = 0.95 mJ, Ro = 0.425 mm).

Several units for measuring the roughness in ablation have been proposed[134]. In our analysis, we used the $RMS/\sqrt{LayerDepth}$ as unit to define roughness in ablation due to the stability observed for the entire range of overlap distances compared to other metrics such as RMS and RMS/LayerDepth (*Figure 49*).
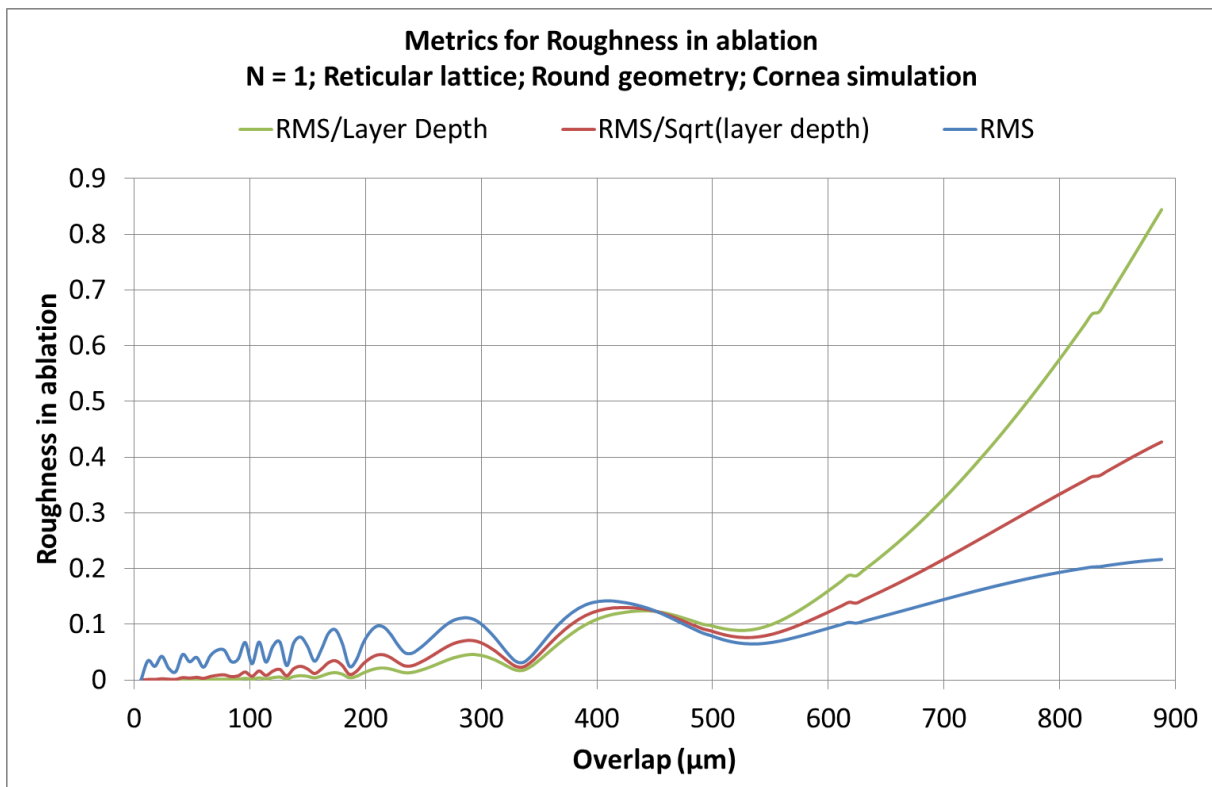
Figure 49. Comparison of different metrics for estimating the roughness in ablation with respect to the varying overlap distances, for the standard test settings presented in Table 7. The metric $RMS/\sqrt{LayerDepth}$ shows good stability for the entire range of overlap distances.

Further to the stability for the entire range of overlap distances, we consider that the variance could well be linear with ablation depth (Layer Depth), so RMS would be linear with the square root of (Layer Depth). In the light of the non-normalized RMS roughness, and provided that different overlaps produce different layer depths, there would exist an optimum overlap for different depths. Therefore, our methods can be implied to optimize the overlap distances in the laser systems used in refractive surgery, based on, a.) The typical depth of refractive surgery treatments, b) dynamically adapted to the particular maximum depth in every refractive surgery treatment, c) dynamically adapted to the local depth of each position in every refractive surgery treatment.

The oscillating nature observed in our results from the simulation model to find the optimum laser beam characteristics, can be explained with an analogy to the Gauss's circle problem for the reticular lattice. The solution of the Gauss's circle problem determines the number of lattice nodes inside the boundary of a circle with center at the origin. Assuming that the ablation matrix is based on an equidistant grid, where a circle defines the boundary of one ablative spot and the center of this circle represents a lattice node on this grid (like *Figure 16*, top left). The overlap distance can be assumed as the distance between two consecutive nodes (i.e. the centers of two such circles in the ablation matrix). When this distance is too small, there would be larger number of overlapping pulses (larger number of lattice nodes within the perimeter of a single spot). As this distance increases the number of overlapping pulses will decrease. For a laser ablation process, this also affects the layer depth (*Figure 32*).

Correspondingly, the increment/decrement of lattice nodes within the perimeter of a single spot occurs in discrete steps (and for a reticular lattice this is a multiple of 4, for a triangular lattice a multiple of 6). Therefore, for some overlap distances, some lattice nodes appear exactly at the boundary of a circle, increasing the resulting roughness (RMS) to its peak. As this lattice node comes within the circle, the roughness gradually decreases to its minimum, and again peaks as the next group of lattice nodes appears at the boundary of the circle. The frequency of this oscillation depends on the overlap distance, changing rapidly (smaller period) for smaller overlap distances and slowly (larger period) for larger overlap distances. This suggests that the amplitude of RMS in the ablation matrix shall remain constant with increasing overlap distances, however the frequency would change. The RMS in ablation obtained in our simulations (*Figure 49*) shows good correspondence with this model, with oscillations of increasing frequency and barely increasing amplitude (0-0.2µm) seen as the overlap distance increases. The other metrics (RMS/$\sqrt{(\text{Layer depth})}$ and RMS/Layer depth) however increase in amplitude (but follow similar frequency as the RMS) as the layer depth decreases with increasing overlap distances. Furthermore, this analogous model may also explain the abrupt changes seen at some overlap distances in our results (*Figure 33* and *Figure 34*), as the discretization due to the overlap distance, affects the roughness (amplitude and frequency) differently for different beam profiles (due to truncation, super Gaussian order etc.). A similar model can be designed to explain the results with the Triangular lattice.

It should be also noted that in the real case, having the theoretical optimum as proposed here does not suffice to reach the optimum real world performance, since there are several factors like spot positioning errors, energy fluctuations[247], drifts of the divergence and thermal drifts involved. We have simulated and evaluated the impact of these factors under the perturbation analysis. A wide range (+/-10%) was chosen for changing the input parameters of the standard test setting (*Table 7*), allowing testing the methods under extreme conditions of variability/technical error. The result of this analysis shows an optimum that lies close to the real world conditions. Therefore, concerning the spot positioning errors, the theoretical results should be modified to account for these fluctuations, for eg. A local minimum of the roughness shall be taken, such that the typical spot positioning errors would not be much detrimental to roughness. Alternatively, for the input standard test setting, any spot overlap below 300µm can be considered as optimum, based on the outcomes of the perturbation analysis.

Plastic models have been used to study the changes in the shape of the flat or spherical surfaces, after refractive surgery[248,249]. Ablating plastic model corneas not affected by biomechanical or other biological effects with clinical lasers, allows to directly measure the actual ablation pattern provided by the laser, avoiding the approximations and assumptions used in theoretical models. However, plastic models are not intended to mimic the response of the cornea but rather used to characterize the laser systems. The differences in ablation process between collagen and PMMA is well documented in the literature. Although purely based on our simulations (and not mimicking the corneal response), the differences in the surface quality and ablation depths in PMMA and human cornea were still evident in our results (*Figure 38*). This is of clinical relevance if PMMA materials are used for initial testing or calibration of the laser system preceding treatment procedures performed in humans. The results suggest a window of overlap distances (<90-150μm), where the correspondence in terms roughness, between PMMA and cornea was better (indicated with a green window in *Figure 38*). Additionally, unlike other groups who found more roughness for deeper ablations in plastic models[134], our theoretical model is consistent with constant roughness for deeper ablations, if one could dynamically adapt the overlap to the particular ablation.

The local ablation frequency and spot overlap has also shown to affect the surface roughness in PMMA[250,251]. Bende et al.[252] used a 1.0 mm Gaussian beam flying spot excimer laser to study the impact of spot overlap and ablation frequency on surface roughness in PMMA flat ablations (like PTK). They found that the surface roughness varies as a function of ablation depth, where the surface roughness for a PTK ablation in PMMA plates varied between 0.26 and 0.49 μm for a 50 μm deep ablation and 0.65 to 1.12 μm for a 250 μm deep ablation. In PMMA the minimal surface roughness was found for an overlap of 72.5%. Although we simulated only sequential spot placement in our methods, we also used a similarly defined spot (~0.9mm spot diameter Gaussian spot). Their findings for optimum overlap correspond well with the optimum 300μm overlap distance we found with the perturbation analysis. Similarly, they found that increased fluence was associated with decreased surface roughness as well as decreased surface waviness, as suggested in our results for the optimum spot energy (*Figure 39*).

In this work, we also performed 8 PMMA tests (each with 12 ablations from -12D to +6D, accounting for a total of 96 ablations on PMMA) in a non-sequential settings procedure to avoid/reduce model bias; time drifts, hysteresis effects. The results obtained in the PMMA ablations tests, are not surprising and confirm the theoretical and simulated predictions[208]. Beyond the confirmation, this work also provides a quantification of the effects (for the described settings) through empirical means.

The empirical tests confirmed that cutting off the intensity (truncation through e.g. a pinhole) introduces a sharp edge that cannot be compensated otherwise and hence roughness is increased. It could be expected that gradual intensity absorption to achieve a smooth laser spot profile would overcome this problem. The pinhole in the AMARIS system lies in a meta-focus, in a position/plane conjugated to the ablation plane, but the pinhole is not the focus. So that the Gaussian focusing optics may actually create a flank out of the pinhole.

Jitter adds random noise while partially reducing the residual. This is equivalent to increase the variance and hence increases roughness. This may not be the theoretical

case for jitter applied to pinhole/truncated beams (as the history shows).[219] Jitter would then smoothen the sharp truncation into a (Gaussian) progressive flank.

Dithering is constructed so that there is very high frequency contribution on one hand side but also a near optimal compromise to achieve the desired ablation profile. The latter is responsible for minimizing the variance. It could be that the roughness is not reduced but only sent to frequencies out of our measurement spectrum.

To increase robustness not only 8x8 analyses, but 4 vs. 4 cumulative analyses, as well as pairwise analyses have been included. Similar to other groups we found more roughness for deeper ablations in plastic models[134], unlike the results of our simulation model. In the PMMA ablations, the effect of dithering was the largest, followed by truncation, and jitter had the lowest impact on results. So that: Dithering approaches help to further minimize residual roughness after ablation; minimum (or no) truncation of the beam is essential to minimize residual roughness after ablation; and jitter shall be avoided to minimize residual roughness after ablation. Interestingly the different test conditions not only affected roughness, but performance as well. The absence of pinhole; the use of ordered dithering; and the absence of jitter all enhanced performance. This can be explained by the fact that the best fit of a rougher shape runs somewhere between the peaks and the valleys of the rough surface. For smoother surfaces the difference from peak to valley reduces, so that the best fit line runs closer to the maximum envelop (peaks).

We found one "anomaly" in PMMA ablation results: The best condition derived from *Figure 43* and *Figure 44* (and *Table 18*) should have been test setting 5 (without pinhole, with dithering, without jitter), but the actual empirical best condition was Test setting 4 (with pinhole, with dithering, without jitter). However, there was no statistically significant difference in roughness between test settings 4 and 5 (empirical best vs. predicted best) (difference in roughness 0.1%; p=.5).

Of the best 4 conditions (*Table 18*): 3 are without pinhole, 3 are with Dithering, and 3 are without Jitter. Pairwise comparisons confirm: the presence of pinholes is systematically worse than no truncation, Dithering is systematically better than without Dithering, and Jitter is systematically worse than without Jitter. Once again confirming the robustness of the findings.

There are few limitations associated with our methods. The simulation methods for optimizing laser beam characteristics were developed for a normal incidence, but did not include the angular dependence of ablation efficiency and the increase in corneal asphericity due to ablation. The impact of beam characteristics on the surface roughness and ablation efficiency were analyzed considering a flat ablation surface. For the PMMA experiments, only 1 AMARIS was involved in the test, the truncation (Pinhole) was tested for a single value (700µm), only ordered pre-dithering was tested, and Jitter was tested for a single value (20µm in X/Y). Further to that no true Gaussian beam was tested, but a close-to-Gaussian beam profile was used for the various test settings. Similarly, PMMA Performance was assessed, and not directly the corneal roughness.

In summary, in our simulations of the polychromatic vision, image quality metrics deteriorated dramatically with increasing roughness. The results also showed that the beam characteristics used in a corneal laser procedure have a major impact on the

surface quality. Low overlap distances result in higher surface roughness compared to high overlap distances. From the simulations, a theoretical proper optimum configuration for minimizing the roughness in ablation for defined input parameters (*Table 7*) have been found specifically, round spot geometry; no spot truncation (truncation fraction = 100%); super Gaussian order N = 1, triangular lattice, with overlap distances corresponding to the valleys in *Figure 36*, that is, 96μm, 120 μm, 132μm. The obtained theoretical results should be modified to account for the fluctuations seen in the real world. For the input standard test setting used in the simulation model, an overlap distance below 300μm shall not detrimentally affect the roughness in ablation, given the perturbations observed in the real world. The PMMA experiments confirmed the theoretical proper optimum settings in real world conditions (limited to the defined input parameters in *Table 12*), specifically no spot truncation (no pinhole); and using dithering strategies without jitter helps minimize the roughness in PMMA ablations.

4.2.1 Outlook

Several factors are associated with the epithelial response in refractive surgery[253,239],[254,255,256]. An important aspect for consideration in post-operative refractive outcomes, is the epithelial masking that will finish the smoothing process after the corneal ablation[240,257]. An optimum topography of the stroma facilitates re-epithelialisation[243,244]. Additionally, it is known that stromal topography affects overlying epithelial function including the differential expression of both cellular and extracellular substances[258]. For a re-growing epithelium affected by laser cuts, the balance between the pressure exerted by the superficial cell layer under tension and the epithelial growth pressure might be the factor determining the thickness of the epithelium at any point of the cornea in steady state conditions[258]. Several other factors have also been identified to be associated with an increase in epithelial thickness, like small ablation zones, greater attempted corrections, and a greater rate of change in power at the edge of the ablation zone. Larger, smoother ablation profiles may result in less epithelial hyperplasia[253]. Although the corneal wound healing response is exceedingly complex, attempts have been made in the past to develop mathematical models used as the basis to design ablation patterns that compensate in advance for the expected corneal surface smoothing response[259,260,261]. However, the mathematical models presented here does not take the above mentioned aspects into account in order to determine the final effect upon the overall refracting surface and level of corneal clarity. An investigation in corneal remodeling should be considered to further explore the benefits of the presented mathematical approaches, closer to the real world conditions.

Based on the presented theoretical results, it can be foreseen that smoother surfaces would be achieved immediately after the ablation, using the proposed laser beam characteristics. This means at least two related potential advantages: 1) Short term outcomes may be better in the time period where the epithelium remodeling/smoothing/masking takes place, 2) Time for surface recovery may be shorter; since the surface is smoother to start with, epithelium may need less remodeling, which means less time for remodeling. Some other advantages of this model can be speculated or at least subjected to clinical assessment, namely, improving the smoothness seems a no risk condition, improvement in short term outcomes (without compromising long term ones), shorter recovery time to reach final

Visual Acuity goal, higher levels of final Visual Acuity, shorter reepithelization time, reduced levels of induced Higher Order Aberrations, and less haze response.

The surface roughness is influenced by the formation of random or almost periodic holes with a depth of several µm. For high quality surface ablation, the formation of periodic structures and random holes should be avoided. This can be achieved by optimizing the lattice arrangement. We applied pre-dithering (anticipating errors) in our methods, but also post-dithering approaches (error diffusion), and other spot sequences and lattice geometries (radial lattices) may be explored. Furthermore, repeating the tests with multiple values of the parameters and with multiple laser systems will provide even more robust evidence for the conclusions.

5 SUMMARY

This thesis aimed to answer two question researched in a scientific manner.

"Can we quantify and compensate for the influence of environment conditions on refractive procedures?"

The large scale retrospective cross sectional study presented here, demonstrated a cyclic winter-summer variation in PMMA ablation using the SCHWIND AMARIS lasers. The season winter and summer showed statistical significant variations with respect to the global values for all the tested parameters except the nominal number of laser pulses for high and low fluence setting. The metric technical performance of the analyzed systems showed a stronger PMMA ablation performance in summer time compared to a weaker performance in the winter time, with the maximum seasonal deviation of 6%. The results were consistently confirmed in seasonal as well as monthly analyses.

These seasonal variations were further substantiated with the experiments conducted in the climate chamber, over a wide range of temperature and humidity. Temperature changes did not affect laser pulse energy, pulse fluence, and ablation efficiency (on PMMA or porcine corneal tissue) significantly. However, changes in relative humidity were more critical and significantly affected laser pulse energy, high fluence and low fluence. For extremely low humidity and high temperatures (30°C with 20%RH, dry and hot conditions), higher refractive change (106%) was recorded, compared to reduced efficiency (93%) at low temperatures and high humidity (18°C with 80%RH, cold and dry conditions). In our results, an opposite trend in performance of PMMA and tissue was confirmed through two independent analysis methods.

We believe this work does not merely represents a calibration study but a comprehensive laboratory science from basic source of energy to corneas of porcine origin as ex Vivo model, including all regular calibration check-ups in the chain. Hence, its value goes well beyond a simple calibration analysis and provides information on how outcomes may vary under different environments. This aspect is relevant for the final users and is not covered by the technical calibration of the systems; and also renders a direct clinical application related aspect to the study. In summary, the proposed well-fitting multi-linear model can be utilized for compensation of temperature and humidity changes on ablation efficiency. The relationship between calibration materials like PMMA and corneal tissue shall be analyzed cautiously before designing the calibration routine, in order to obtain optimum outcomes with minimum deviations.

 "Can we quantify the influence of post-ablation roughness on vision and perception, and optimize refractive procedures for a minimum post-operative roughness?"

The surface quality of the cornea after ablation is important for the clinical outcomes. Smoother corneal surface after ablation is synonymous to more efficient refractive correction. Lower levels of roughness in the cornea, will induce less scatter and present a more regular optical surface to start healing. As the healing process begins with a more regular optical surface, it potentially improves the optical surface further, achieving even higher than natural levels of optical quality. Stromal roughness can be

simply expressed as sequences of stromal peaks and troughs. In the natural healing process of the cornea, the epithelium would need to fill up the troughs to the level of the peaks to eliminate roughness and regularize the corneal surface. Thus, for lower roughness, a lower volume of reepithelization is required. Roughness can be seen as aberrations of very high orders; the healing process smoothens out this roughness reducing the aberrations post-operatively.

The development of Smart Pulse Technology was the harbinger for the research group, to explore these clinical benefits. The research presented here further those efforts. Despite its limitations, the proposed simple and robust method for quantifying the influence of post-ablation roughness on vision and perception, can be utilized in different applications. This method can be applied clinically to different laser platforms based on their associated roughness for choosing a better treatment plan for the patient. Furthermore, it can be used for computing realistic image quality metrics for the patient's postoperative vision at a relatively low cost. Since normally laser ablation is an integral process divided on a defined grid, the impact of spatially characterized noise represents a more realistic simulation condition. This method can help comparing different refractive laser platforms in terms of their associated roughness in ablation, indirectly improving the quality of results after Laser vision correction surgery.

We presented here a rigorous simulation model for simulating shot-by-shot ablation process. From the simulations, a theoretical proper optimum configuration was found for minimizing the roughness in ablation for defined input parameters. The PMMA experiments confirmed the theoretical proper optimum settings in real world conditions, specifically no spot truncation (no pinhole); and using dithering strategies without jitter helps minimize the roughness in PMMA ablations. The proposed model can be used for optimization of laser systems used for ablation processes at relatively low cost and would directly improve the quality of results.

The current popularity of excimer Laser refractive surgery suggests a need for continued research and refinements to further improve clinical outcomes.[138] A fundamental limitation of current clinical systems is the lack of real-time feedback specifically addressing the Laser-tissue interactions as directly related to Laser ablation rates. Furthermore, defining proper test patterns for the routine check of ablative systems is not an easy task. There are many different components to be tested, and a single system test can only show a qualitative overall status of a system, but, in general, cannot identify the specific sources of error when the PASS criteria are not met. For that reason, it is necessary to develop a comprehensive test for checking the overall status, including the spot roundness, scanner symmetry, scanning amplitude, scanner relative and absolute orientation, spot size and shape, calibration of centration, calibration of rotational orientation, and calibration of perpendicular orientation. Simple yet comprehensive set of patterns shall be designed, which are fast to perform and quick and easy to analyze and calibrate the overall status of a system.

We believe that implying the findings of this work will help reduce the complications and occurrence of adverse events during and after refractive surgery, improving the short term and long term postoperative quality of vision, reduce the time of postoperative recovery, as well as reduce the ratio of retreatments and reoperations. Any potential risks of the aforementioned methods and results need to be evaluated in clinical studies before they could be implemented in commercial medical devices.

....

6   REFERENCES

1. Kaluzny, B.J., Piotrowiak-Slupska, I., Kaszuba-Modrzejewska, M., Stachura, J., Arba-Mosquera, S., and Verma, S. (2019). Three-year outcomes after high hyperopia correction using photorefractive keratectomy with a large ablation zone. Br. J. Ophthalmol. *103*, 849–854.

2. Luger, M.H.A., McAlinden, C., Buckhurst, P.J., Wolffsohn, J.S., Verma, S., and Arba Mosquera, S. (2015). Presbyopic LASIK using hybrid bi-aspheric micro-monovision ablation profile for presbyopic corneal treatments. Am. J. Ophthalmol. *160*, 493–505.

3. Gould, G. (1959). Laser. US patent: US19590804539 19590406.

4. Schawlow, A.L., and Townes, C.H. (1958). Infrared and optical masers. Phys. Rev. *112*, 1940–1949.

5. Swinger, C.A. (1981). Refractive surgery for the correction of myopia. Trans. Ophthalmol. Soc. U. K. *101 (Pt 4)*, 434–439.

6. Munnerlyn, C.R., Koons, S.J., and Marshall, J. (1988). Photorefractive keratectomy: a technique for laser refractive surgery. J. Cataract Refract. Surg. *14*, 46–52.

7. Krueger, R.R., and Trokel, S.L. (1985). Quantitation of corneal ablation by ultraviolet laser light. Arch. Ophthalmol. (Chicago, Ill. 1960) *103*, 1741–1742.

8. Pettit, G.H., Ediger, M.N., and Weiblinger, R.P. (1991). Excimer laser corneal ablation: absence of a significant "incubation" effect. Lasers Surg. Med. *11*, 411–418.

9. Steiner, R. (2011). Laser-Tissue Interactions. In Laser and IPL Technology in Dermatology and Aesthetic Medicine, (Berlin, Heidelberg: Springer Berlin Heidelberg), pp. 23–36.

10. Boulnois, J.L. (1986). Photophysical processes in recent medical laser developments: A review. Lasers Med. Sci. *1*, 47–66.

11. Anderson, R.R., and Parrish, J.A. (1983). Selective photothermolysis: precise microsurgery by selective absorption of pulsed radiation. Science *220*, 524–527.

12. Ibm.com. (2019). *IBM100 - Excimer Laser Surgery*. [online] Available at: https://www.ibm.com/ibm/history/ibm100/us/en/icons/excimer/ [Accessed 02 Jan. 2019].

13. Trokel, S.L., Srinivasan, R., and Braren, B. (1983). Excimer laser surgery of the cornea. Am. J. Ophthalmol. *96*, 710–715.

14. McDonnell, P.J., Moreira, H., Garbus, J., Clapham, T.N., D'Arcy, J., and Munnerlyn, C.R. (1991). Photorefractive keratectomy to create toric ablations for correction of astigmatism. Arch. Ophthalmol. (Chicago, Ill. 1960) *109*, 710–713.

15. Buratto, L., Ferrari, M., and Rama, P. (1992). Excimer laser intrastromal keratomileusis. Am. J. Ophthalmol. *113*, 291–295.

16. Pallikaris, I.G., and Siganos, D.S. (1994). Excimer laser in situ keratomileusis and photorefractive keratectomy for correction of high myopia. J. Refract. Corneal Surg. *10*, 498–510.

17. Ren, Q., Simon, G., Legeais, J.M., Parel, J.M., Culbertson, W., Shen, J., Takesue, Y., and Savoldelli, M. (1994). Ultraviolet solid-state laser (213-nm) photorefractive keratectomy. In vivo study. Ophthalmology *101*, 883–889.

18. Gobbi, P.G., Carones, F., Brancato, R., Carena, M., Fortini, A., Scagliotti, F., Morico, A., and Venturi, E. (1995). Automatic eye tracker for excimer laser photorefractive keratectomy. J. Refract. Surg. *11*, S337-42.

19. Camellin, M. (2003). Laser epithelial keratomileusis for myopia. J. Refract. Surg. *19*, 666–670.

20. SIMON, G., and HUANG, C.-H. (1997). LASER BEAM OPHTHALMOLOGICAL SURGERY METHOD AND APPARATUS. WO9717903

21. Antón, A., Andrada, M.T., Mayo, A., Portela, J., and Merayo, J. (2009). Epidemiology of refractive errors in an adult European population: the Segovia study. Ophthalmic Epidemiol. *16*, 231–237.

22. Cotliar, A.M., Schubert, H.D., Mandel, E.R., and Trokel, S.L. (1985). Excimer laser radial keratotomy. Ophthalmology *92*, 206–208.

23. Campos, M., Lee, M., and McDonnell, P.J. (1992). Ocular integrity after refractive surgery: effects of photorefractive keratectomy, phototherapeutic keratectomy, and radial keratotomy. Ophthalmic Surg. *23*, 598–602.

24. Buratto, L., Ferrari, M., and Genisi, C. (1993). Myopic keratomileusis with the excimer laser: one-year follow up. Refract. Corneal Surg. *9*, 12–19.

25. Kim, W.J., Shah, S., and Wilson, S.E. (1998). Differences in keratocyte apoptosis following transepithelial and laser-scrape photorefractive keratectomy in rabbits. J. Refract. Surg. *14*, 526–533.

26. Krueger, R.R., Juhasz, T., Gualano, A., and Marchi, V. (1998). The picosecond laser for nonmechanical laser in situ keratomileusis. J. Refract. Surg. *14*, 467–469.

27. Pallikaris, I.G., Katsanevaki, V.J., Kalyvianaki, M.I., and Naoumidi, I.I. (2003). Advances in subepithelial excimer refractive surgery techniques: Epi-LASIK. Curr. Opin. Ophthalmol. *14*, 207–212.

28. Durrie, D.S., Slade, S.G., and Marshall, J. (2008). Wavefront-guided excimer laser ablation using photorefractive keratectomy and sub-Bowman's keratomileusis: a contralateral eye study. J. Refract. Surg. *24*, S77-84.

29. Camellin, M., and Wyler, D. (2008). Epi-LASIK versus epi-LASEK. J. Refract. Surg. *24*, S57-63.

30. Nielsen, R., Christiansen, M.K., Kristensen, M.S., Møller, C., Hedegaard, C., Aagaard, N., Sejersen, H., Hjortdal, J., and Ivarsen, A. (2019). Reproducibility of subjective refraction before and after small incision lenticule extraction (SMILE) for myopia. Acta Ophthalmol.

31. Salmon, T.M.F. (1999). Corneal contribution to the wavefront aberration of the eye.

32. Mrochen, M., Jankov, M., Bueeler, M., and Seiler, T. (2003). Correlation between corneal and total wavefront abe. J Refract. *19*, 104–112.

33. Burns, S.A. (2000). The spatially resolved refractometer. J. Refract. Surg. *16*, S566-9.

34. Tscherning, M. (1894). Die monochromatischen Aberratoinen des menschlichen. Auges Z Psychol Physiol Sinn. *6*, 456-471.

35. Mrochen, M., Kaemmerer, M., Mierdel, P., Krinke, H.E., and Seiler, T. (2000). Principles of Tscherning aberrometry. J. Refract. Surg. *16*, S570-1.

36. Hartmann, J. (1900). Bemerkungen ueber den Bau und die Justierung von Spktrographen. Zeitschrift fuer Instrumentenkunde. *1900*, 20:47.

37. Shack, R.B., and Platt, B.C. (1971). Production and use of a lenticular Hartmann screen. J Opt Soc Am. 61, 656.

38. MacRae, S., and Fujieda, M. (2000). Slit skiascopic-guided ablation using the Nidek laser. J. Refract. Surg. *16*, S576-80.

39. Liang, J., Grimm, B., Goelz, S., and Bille, J.F. (1994). Objective measurement of wave aberrations of the human eye with the use of a Hartmann-Shack wave-front sensor. J. Opt. Soc. Am. A. Opt. Image Sci. Vis. *11*, 1949–1957.

40. Babcock, H.W. (1990). Roddier wavefront sensor. Science *250*, 192.

41. Moreno-Barriuso, E., Marcos, S., Navarro, R., and Burns, S.A. (2001). Comparing laser ray tracing, the spatially resolved refractometer, and the Hartmann-Shack sensor to measure the ocular wave aberration. Optom. Vis. Sci. *78*, 152–156.

42. Canals, M., Elies, D., Costa-Vila, J., and Coret, A. (2004). Comparative Study of Ablation Profiles of Six Different Excimer Lasers. J. Refract. Surg. *20*, 106–109.

43. Arba-Mosquera, S., and Verma, S. (2013). Analytical optimization of the ablation efficiency at normal and non-normal incidence for generic super Gaussian beam profiles. Biomed. Opt. Express *4*, 1422–1433.

44. Pettit, G.H., and Ediger, M.N. (1996). Corneal-tissue absorption coefficients for 193- and 213-nm ultraviolet radiation. Appl. Opt. *35*, 3386–3391.

45. Nikogosyan, D.N., and Görner, H. (1999). Laser-induced photodecomposition of amino acids and peptides: extrapolation to corneal collagen. IEEE J. Sel. Top. Quantum Electron. *5*, 1107–1115.

46. Mrochen, M., Kaemmerer, M., and Seiler, T. (2001). Clinical results of wavefront-guided laser in situ keratomileusis 3 months after surgery. J. Cataract Refract. Surg. *27*, 201–207.

47. Levy, Y., Segal, O., Avni, I., and Zadok, D. (2005). Ocular higher-order aberrations in eyes with supernormal vision. Am. J. Ophthalmol. *139*, 225–228.

48. Applegate, R.A., and Howland, H.C. (1997). Refractive surgery, optical aberrations, and visual performance. J. Refract. Surg. *13*, 295–299.

49. Gambra, E., Sawides, L., Dorronsoro, C., and Marcos, S. (2009). Accommodative lag and fluctuations when optical aberrations are manipulated. J. Vis. *9*, 4.1-15.

50. Awwad, S.T., Arba Mosquera, S., and Verma, S. (2018). Corneal Wavefront-Guided Ablation. In Customized Laser Vision Correction, (Springer International Publishing), pp. 167–184.

51. Blake, R. (1982). Binocular vision in normal and stereoblind subjects. Am. J. Optom. Physiol. Opt. *59*, 969–975.

52. Wheatstone, C. (1850). Contributions to the Physiology of Vision.Part II. On Some Remarkable, and Hitherto Unobserved, Phaenomena of Binocular Vision,(Continued). Proc. R. Soc. London *6*, 138–141.

53. Vishwanath, D. (2014). Toward a new theory of stereopsis. Psychol. Rev. *121*, 151–178.

54. Blake, R., and Cormack, R.H. (1979). On utrocular discrimination. Percept. Psychophys. *26*, 53–68.

55. Miles, W.R. (1930). Ocular dominance in human adults. J. Gen. Psychol. *3*, 412–430.

56. Hariharan-Vilupuru, S., and Bedell, H.E. (2009). The perceived visual direction of monocular objects in random-dot stereograms is influenced by perceived depth and allelotropia. Vision Res. *49*, 190–201.

57. Wheatstone, C. (1838). Contributions to the Physiology of Vision. Part the First. On Some Remarkable, and Hitherto Unobserved, Phenomena of Binocular Vision : Wheatstone, C. : Free Download & Streaming : Internet Archive. Phil. Trans. R. Soc. Lond. *128*, 371–394.

58. Arba Mosquera, S., and Verma, S. (2016). Bilateral symmetry in vision and influence of ocular surgical procedures on binocular vision: A topical review. J. Optom. *9*, 219–230.

59. Li, Y., and Bao, F.J. (2014). Interocular symmetry analysis of bilateral eyes. J. Med. Eng. Technol. *38*, 179–187.

60. Henriquez, M.A., Izquierdo, L., and Mannis, M.J. (2013). Intereye asymmetry detected by Scheimpflug imaging in subjects with normal corneas and keratoconus. Cornea *32*, 779–782.

61. Dienes, L., Kránitz, K., Juhász, E., Gyenes, A., Takács, A., Miháltz, K., Nagy, Z.Z., and Kovács, I. (2014). Evaluation of intereye corneal asymmetry in patients with keratoconus. A scheimpflug imaging study. PLoS One *9*, e108882.

62. Smadja, D., Santhiago, M.R., Mello, G.R., Krueger, R.R., Colin, J., and Touboul, D. (2013). Influence of the reference surface shape for discriminating between normal corneas, subclinical keratoconus, and keratoconus. J. Refract. Surg. *29*, 274–281.

63. Pflugfelder, S.C., Liu, Z., Feuer, W., and Verm, A. (2002). Corneal thickness indices discriminate between keratoconus and contact lens-induced corneal thinning. Ophthalmology *109*, 2336–2341.

64. Ambrósio, R., Alonso, R.S., Luz, A., and Coca Velarde, L.G. (2006). Corneal-thickness spatial profile and corneal-volume distribution: tomographic indices to detect keratoconus. J. Cataract Refract. Surg. *32*, 1851–1859.

65. Thibos, L.N., Hong, X., Bradley, A., and Cheng, X. (2002). Statistical variation of aberration structure and image quality in a normal population of healthy eyes. J. Opt. Soc. Am. A. Opt. Image Sci. Vis. *19*, 2329–2348.

66. Arba Mosquera, S., de Ortueta, D., and Verma, S. (2018). Corneal functional optical zone under monocular and binocular assessment. Eye Vis. (London, England) *5*, 3.

67. Marcos, S., and Burns, S.A. (2000). On the symmetry between eyes of wavefront aberration and cone directionality. Vision Res. *40*, 2437–2447.

68. Jiménez, J.R., Villa, C., Anera, R.G., Gutiérrez, R., and del Barco, L.J. (2006). Binocular visual performance after LASIK. J. Refract. Surg. *22*, 679–688.

69. Pineles, S.L., Velez, F.G., Yu, F., Demer, J.L., and Birch, E. (2014). Normative Reference Ranges for Binocular Summation as a Function of Age for Low Contrast Letter Charts. Strabismus *22*, 167–175.

70. Pointer, J.S. (2008). Influence of selected variables on monocular, interocular, and binocular visual acuity. Optom. Vis. Sci. *85*, 135–142.

71. Pineles, S.L., Velez, F.G., Isenberg, S.J., Fenoglio, Z., Birch, E., Nusinowitz, S., and Demer, J.L. (2013). Functional burden of strabismus: decreased binocular summation and binocular inhibition. JAMA Ophthalmol. *131*, 1413–1419.

72. Mansouri, B., Thompson, B., and Hess, R.F. (2008). Measurement of suprathreshold binocular interactions in amblyopia. Vision Res. *48*, 2775–2784.

73. Pardhan, S., and Gilchrist, J. (1992). Binocular contrast summation and inhibition in amblyopia. The influence of the interocular difference on binocular contrast sensitivity. Doc. Ophthalmol. *82*, 239–248.

74. Schor, C.M., and Levi, D.M. (1980). Disturbances of small-field horizontal and vertical optokinetic nystagmus in amblyopia. Invest. Ophthalmol. Vis. Sci. *19*, 668–683.

75. Huurneman, B., and Boonstra, F.N. (2013). Monocular and binocular development in children with albinism, infantile nystagmus syndrome, and normal vision. Strabismus *21*, 216–224.

76. Villa, C., Jiménez, J.R., Anera, R.G., Gutiérrez, R., and Hita, E. (2009). Visual performance after LASIK for a Q-optimized and a standard ablation algorithm. Appl. Opt. *48*, 5741–5747.

77. Zhang, Y., Chen, Y.-G., and Xia, Y.-J. (2013). Comparison of corneal flap morphology using AS-OCT in LASIK with the WaveLight FS200 femtosecond laser versus a mechanical microkeratome. J. Refract. Surg. *29*, 320–324.

78. Montés-Micó, R., Rodríguez-Galietero, A., and Alió, J.L. (2007). Femtosecond laser versus mechanical keratome LASIK for myopia. Ophthalmology *114*, 62–68.

79. Arbelaez, M.C., Vidal, C., and Arba-Mosquera, S. (2010). Bilateral symmetry before and six months after aberration-freeTM correction with the schwind amaris totaltech laser: Clinical outcomes. J. Optom. *3*, 20–28.

80. Azen, S.P., Varma, R., Preston-Martin, S., Ying-Lai, M., Globe, D., and Hahn, S. (2002). Binocular visual acuity summation and inhibition in an ocular epidemiological study: the Los Angeles Latino Eye Study. Invest. Ophthalmol. Vis. Sci. *43*, 1742–1748.

81. Arba Mosquera, S., Verma, S., and McAlinden, C. (2015). Centration axis in refractive surgery. Eye Vis. (London, England) *2*, 4.

82. Mcalinden, C. (2012). Corneal refractive surgery: Past to present GOD OPSUMMERINGS ARTIKEL. Clin. Exp. Optom. *95*, 386–398.

83. Thibos, L. N. (1995). How to Measure Chromatic Aberration and Locate Useful Reference Axes of the Human Eye, (Portland, OSA conference)

84. Arba Mosquera, S. (2010). *Optimization of the ablation profiles in customized treatments for laser corneal refractive surgery*. Ph. D. Universidad de Vallodlid.

85. De Ortueta, D., and Arba Mosquera, S. (2007). Centration during hyperopic LASIK using the coaxial light reflex. J. Refract. Surg. *23*, 11; author reply 11.

86. Reinstein, D.Z., Gobbe, M., and Archer, T.J. (2013). Coaxially sighted corneal light reflex versus entrance pupil center centration of moderate to high hyperopic corneal ablations in eyes with small and large angle kappa. J. Refract. Surg. *29*, 518–525.

87. Schruender, S.A., Fuchs, H., Spasovski, S., and Dankert, A. (2002). Intraoperative corneal topography for image registration. J. Refract. Surg. *18,* S624-9.

88. Arba Mosquera, S., and Ewering, T. (2012). New asymmetric centration strategy combining pupil and corneal vertex information for ablation procedures in refractive surgery: theoretical background. J. Refract. Surg. *28,* 567–573.

89. Bará, S., Arines, J., Ares, J., and Prado, P. (2006). Direct transformation of Zernike eye aberration coefficients between scaled, rotated, and/or displaced pupils. J. Opt. Soc. Am. A. Opt. Image Sci. Vis. *23*, 2061–2066.

90. Lundström, L., and Unsbo, P. (2007). Transformation of Zernike coefficients: scaled, translated, and rotated wavefronts with circular and elliptical pupils. J. Opt. Soc. Am. A. Opt. Image Sci. Vis. *24*, 569–577.

91. Comastri, S.A., Perez, L.I., Pérez, G.D., Bastida, K., and Martin, G. (2008). Wavefront aberrations: Analytical method to convert Zernike coefficients from a pupil to a scaled arbitrarily decentered one. In AIP Conference Proceedings, pp. 69–74.

92. Tsai, Y.Y., and Lin, J.M. (2000). Ablation centration after active eye-tracker-assisted photorefractive keratectomy and laser in situ keratomileusis. J. Cataract Refract. Surg. *26*, 28–34.

93. Smith, E.M., and Talamo, J.H. (1995). Cyclotorsion in the seated and supine patient. J. Cataract Refract. Surg. *21*, 402–403.

94. Arba Mosquera, S., and Verma, S. (2015). Effects of torsional movements in refractive procedures. J. Cataract Refract. Surg. *41*, 1752–1766.

95. Arba-Mosquera, S., De Ortueta, D., and Verma, S. (2016). Minimising residual aberration in the presence of cyclotorsion uncertainty in refractive surgery. J Emmetropia *3*, 139–144.

96. Shi, Y., Queener, H.M., Marsack, J.D., Ravikumar, A., Bedell, H.E., and Applegate, R.A. (2013). Optimizing wavefront-guided corrections for highly aberrated eyes in the presence of registration uncertainty. J. Vis. *13*.

97. Arba Mosquera, S. and Ortueta, D. (2011). Theoretical influence of decentred ablations on induced Coma aberrations. Journal of Emmetropia. *2*. 153-158.

98. Arba Mosquera, S., and Verma, S. (2014). Numerical nonwavefront-guided algorithm for expansion or recentration of the optical zone. J. Biomed. Opt. *19*, 088001.

99. Charman, W.N., and Atchison, D.A. (2009). Decentred optical axes and aberrations along principal visual field meridians. Vision Res. *49*, 1869–1876.

100. Arbelaez, M.C., Ewering, T., and Arba Mosquera, S. (2010). Decision Assistant Wizard to standardize optimal outcomes in excimer laser refractive corneal surgery. J. Refract. Surg. *26*, 980–990.Alpins, N.A. (1997). New method of targeting vectors to treat astigmatism. J. Cataract Refract. Surg. *23*, 65–75.

101.   Alpins, N.A. (1997). New method of targeting vectors to treat

astigmatism. J. Cataract Refract. Surg. *23*, 65–75.

102.   Alpins, N. (2001). Astigmatism analysis by the Alpins method. J.

Cataract Refract. Surg. *27*, 31–49.

103.   Alpins, N., and Stamatelatos, G. (2007). Customized photoastigmatic

refractive keratectomy using combined topographic and refractive data for

myopia and astigmatism in eyes with forme fruste and mild keratoconus. J.

Cataract Refract. Surg. *33*, 591–602.

104.   Piñero, D.P., Pérez-Cambrodí, R.J., Soto-Negro, R., Ruiz-Fortes, P.,

and Artola, A. (2015). Clinical utility of ocular residual astigmatism and

topographic disparity vector indexes in subclinical and clinical keratoconus.

Graefes Arch. Clin. Exp. Ophthalmol. *253*, 2229–2237.

105.   Martínez-Abad, A., Piñero, D.P., Ruiz-Fortes, P., and Artola, A. (2017).

Evaluation of the diagnostic ability of vector parameters characterizing the

corneal astigmatism and regularity in clinical and subclinical keratoconus.

Cont. Lens Anterior Eye *40*, 88–96.

106.   Alpins, N. (2007). Combined wavefront and Topography Approaches to

Refractive Surgery treatments.

107.   Alpins, N., and Stamatelatos, G. (2008). Clinical outcomes of laser in

situ keratomileusis using combined topography and refractive wavefront

treatments for myopic astigmatism. J. Cataract Refract. Surg. *34*, 1250–1259.

108.   Arbelaez, M.C., Alpins, N., Verma, S., Stamatelatos, G., Arbelaez, J.G.,

and Arba-Mosquera, S. (2017). Clinical outcomes of laser in situ

keratomileusis with an aberration-neutral profile centered on the corneal vertex

comparing vector planning with manifest refraction planning for the treatment

of myopic astigmatism. J. Cataract Refract. Surg. *43*, 1504–1514.

109.   Arba-Mosquera, S., Vinciguerra, P., and Verma, S. (2018). Review of

technological advancements in calibration systems for laser vision correction.

J. Biomed. Opt. *23*, 1.

110.   Arba-Mosquera, S., and Triefenbach, N. (2012). Analysis of the cornea-

to-PMMA ablation efficiency rate. J. Mod. Opt. *59*, 930–941.

111.   Wernli, J., Schumacher, S., Wuellner, C., Donitzky, C., and Mrochen, M.

(2012). Initial surface temperature of PMMA plates used for daily laser

calibration affects the predictability of corneal refractive surgery. J. Refract.

Surg. *28*, 639–644.

112.   Thomas, J.W., Mitra, S., Chuang, A.Z., and Yee, R.W. (2003). Electron

microscopy of surface smoothness of porcine corneas and acrylic plates with

four brands of excimer laser. J. Refract. Surg. *19*, 623–628.

113.   Watson, A.B., and Ahumada, A.J. (2012). Modeling acuity for optotypes

varying in complexity. J. Vis. *12*.

114.   Watson, A.B., and Ahumada, A.J. (2008). Predicting visual acuity from

wavefront aberrations. J. Vis. *8*.

115.   Thibos, L.N., Applegate, R.A., Schwiegerling, J.T., Webb, R., and VSIA

Standards Taskforce Members. Vision science and its applications (2002).

Standards for reporting the optical aberrations of eyes. J. Refract. Surg. *18*,

S652-60.

116.   Watson, A.B., and Ahumada, A.J. (2015). Letter identification and the

neural image classifier. J. Vis. *15*.

117.   Marsack, J.D., Thibos, L.N., and Applegate, R.A. (2004). Metrics of

optical quality derived from wave aberrations predict visual performance. J.

Vis. *4*, 322–328.

118.   Marcos, S., Barbero, S., Llorente, L., and Merayo-Lloves, J. (2001).
Optical response to LASIK surgery for myopia from total and corneal
aberration measurements. Invest. Ophthalmol. Vis. Sci. *42*, 3349–3356.

119.   Applegate, R.A., Marsack, J.D., and Thibos, L.N. (2006). Metrics of
retinal image quality predict visual performance in eyes with 20/17 or better
visual acuity. Optom. Vis. Sci. *83*, 635–640.

120.   Cheng, X., Bradley, A., and Thibos, L.N. (2004). Predicting subjective
judgment of best focus with objective image quality metrics. J. Vis. *4*, 310–
321.

121.   Chen, L., Singer, B., Guirao, A., Porter, J., and Williams, D.R. (2005).
Image metrics for predicting subjective image quality. Optom. Vis. Sci. *82*,
358–369.

122.   Marcos, S., Burns, S.A., Moreno-Barriusop, E., and Navarro, R. (1999).
A new approach to the study of ocular chromatic aberrations. Vision Res. *39*,
4309–4323.

123.   Ravikumar, S., Bradley, A., Thibos, L.N. (2006). Do Monochromatic
Aberrations Protect The Eye Against Chromatic Blur? . *Invest. Ophthalmol.
Vis. Sci. 47*(13):1505.

124.   Van Meeteren, A. (1974). Calculations on the optical modulation
transfer function of the human eye for white light. Opt. Acta (Lond). *21*, 395–
412.

125.   Ravikumar, S., Thibos, L.N., and Bradley, A. (2008). Calculation of
retinal image quality for polychromatic light. J. Opt. Soc. Am. A. Opt. Image
Sci. Vis. *25*, 2395–2407.

126. McNeely, R.N., Moutari, S., Arba-Mosquera, S., Verma, S., and Moore, J.E. (2018). An alternative application of Rasch analysis to assess data from ophthalmic patient-reported outcome instruments. PLoS One *13*.

127. Pettit, G.H. (2006). The ideal excimer beam for refractive surgery. J. Refract. Surg. *22*, S969-72.

128. Arba Mosquera, S., and Verma, S. (2015). Analysis of the change in peak corneal temperature during excimer laser ablation in porcine eyes. J. Biomed. Opt. *20*, 78001.

129. Shealy, D.L., and Hoffnagle, J.A. (2006). Laser beam shaping profiles and propagation. Appl. Opt. *45*, 5118–5131.

130. Meister, J., Franzen, R., Apel, C., and Gutknecht, N. (2004). Influence of the spatial beam profile on hard tissue ablation, Part II: Pulse energy and energy density distribution in simple beams. Lasers Med. Sci. *19*, 112–118.

131. Meister, J., Apel, C., Franzen, R., and Gutknecht, N. (2003). Influence of the spatial beam profile on hard tissue ablation. Part I: Multimode emitting Er:YAG lasers. Lasers Med. Sci. *18*, 112–118.

132. Arba-Mosquera, S., and Klinner, T. (2014). Improving the ablation efficiency of excimer laser systems with higher repetition rates through enhanced debris removal and optimized spot pattern. J. Cataract Refract. Surg. *40*, 477–484.

133. Mrochen, M., Schelling, U., Wuellner, C., and Donitzky, C. (2009). Influence of spatial and temporal spot distribution on the ocular surface quality and maximum ablation depth after photoablation with a 1050 Hz excimer laser system. J. Cataract Refract. Surg. *35*, 363–373.

134.   O'Donnell, C.B., Kemner, J., and O'Donnell, F.E. (1996). Surface roughness in PMMA is linearly related to the amount of excimer laser ablation. J. Refract. Surg. *12*, 171–174.

135.   Bhushan, B. (2000). Surface Roughness Analysis and Measurement Techniques. CRC Press.

136.   Lombardo, M., De Santo, M.P., Lombardo, G., Barberi, R., and Serrao, S. (2005). Roughness of excimer laser ablated corneas with and without smoothing measured with atomic force microscopy. J. Refract. Surg. *21*, 469–475.

137.   Jiménez, J.R., Rodríguez-Marín, F., Anera, R.G., and Jiménez Del Barco, L. (2006). Deviations of Lambert-Beer's law affect corneal refractive parameters after refractive surgery. Opt. Express *14*, 5411–5417.

138.   Fisher, B.T., and Hahn, D.W. (2011). Real-time measurement of ArF excimer laser corneal tissue ablation rates using cross-correlation of laser waveforms. Opt. Express *19*, 4231.

139.   Shanyfelt, L.M., Dickrell, P.L., Edelhauser, H.F., and Hahn, D.W. (2008). Effects of laser repetition rate on corneal tissue ablation for 193-nm excimer laser light. Lasers Surg. Med. *40*, 483–493.

140.   Fisher, B.T., and Hahn, D.W. (2007). Development and numerical solution of a mechanistic model for corneal tissue ablation with the 193 nm argon fluoride excimer laser. J. Opt. Soc. Am. A. Opt. Image Sci. Vis. *24*, 265–277.

141.   Shraiki, M., and Arba-Mosquera, S. (2011). Simulation of the impact of refractive surgery ablative laser pulses with a flying-spot laser beam on intrasurgery corneal temperature. Invest. Ophthalmol. Vis. Sci. *52*, 3713–3722.

142. Fisher, B.T., and Hahn, D.W. (2004). Determination of excimer laser ablation rates of corneal tissue using wax impressions of ablation craters and white-light interferometry. Ophthalmic Surg. Lasers Imaging *35*, 41–51.

143. Ediger, M.N., Pettit, G.H., and Hahn, D.W. (1994). Enhanced ArF laser absorption in a collagen target under ablative conditions. Lasers Surg. Med. *15*, 107–111.

144. Dorronsoro, C., and Marcos, S. (2007). Experiments on PMMA model to predict the impact of corneal refractive surgery on corneal shape: Reply. Opt. Express *15*, 7245–7246.

145. Anera, R.G., Villa, C., Jiménez, J.R., Gutiérrez, R., and Del Barco, L.J. (2005). Differences between real and predicted corneal shapes after aspherical corneal ablation. Appl. Opt. *44*, 4528–4532.

146. Jiménez, J.R., Castro, J.J., Ortiz, C., and Anera, R.G. (2010). Testing a model for excimer laser-ablation rates on corneal shape after refractive surgery. Opt. Lett. *35*, 1789.

147. Abitan, H., Bohr, H., and Buchhave, P. (2008). Correction to the Beer-Lambert-Bouguer law for optical absorption. Appl. Opt. *47*, 5354–5357.

148. Cano, D., Barbero, S., and Marcos, S. (2004). Comparison of real and computer-simulated outcomes of LASIK refractive surgery. J. Opt. Soc. Am. A. Opt. Image Sci. Vis. *21*, 926–936.

149. Arba-Mosquera, S., and de Ortueta, D. (2008). Geometrical analysis of the loss of ablation efficiency at non-normal incidence. Opt. Express *16*, 3877.

150. Arba-Mosquera, S., and Hollerbach, T. (2010). Ablation resolution in laser corneal refractive surgery: The dual fluence concept of the AMARIS platform. Adv. Opt. Technol.(1995).

151.   Frey, R. W., Burkhalter, J. H. and Gray G. P. (1998). Laser Sculpting System US Patent 5,849,006.

152.   Guirao, A., Williams, D.R., and MacRae, S.M. (2003). Effect of Beam Size on the Expected Benefit of Customized Laser Refractive Surgery. J. Refract. Surg. *19*, 15–23.

153.   Huang, D., and Arif, M. (2002). Spot size and quality of scanning laser correction of higher-order wavefront aberrations. J. Cataract Refract. Surg. *28*, 407–416.

154.   Huang, D., and Arif, M. (2001). Spot size and quality of scanning laser correction of higher order wavefront aberrations. J. Refract. Surg. *17*, S588-91.

155.   Aslanides, I.M., and Kymionis, G.D. (2017). Trans advanced surface laser ablation (TransPRK) outcomes using SmartPulseTechnology. Cont. Lens Anterior Eye *40*, 42–46.

156.   Vinciguerra, P., Camesasca, F.I., Vinciguerra, R., Arba-Mosquera, S., Torres, I., Morenghi, E., and Randleman, J.B. (2017). Advanced Surface Ablation With a New Software for the Reduction of Ablation Irregularities. J. Refract. Surg. *33*, 89–95.

157.   Lin, D.T.C., Holland, S.P., Verma, S., Hogden, J., and Arba-Mosquera, S. (2017). Postoperative Corneal Asphericity in Low, Moderate, and High Myopic Eyes After Transepithelial PRK Using a New Pulse Allocation. J. Refract. Surg. *33*, 820–826.

158.   Lin, D.T.C., Holland, S.P., Verma, S., Hogden, J., and Arba-Mosquera, S. (2019). Immediate and short term visual recovery after SmartSurfACE photorefractive keratectomy. J. Optom. *8*.

159. Jiménez, J.R., Anera, R.G., Jiménez Del Barco, L., and Hita, E. (2002). Effect on laser-ablation algorithms of reflection losses and nonnormal incidence on the anterior cornea. Appl. Phys. Lett. *81*, 1521–1523.

160. Morelli, J., Kibbi, A.G., Farinelli, W., Boll, J., and Tan, O.T. (1987). Ultraviolet excimer laser ablation: The effect of wavelength and repetition rate on in vivo guinea pig skin. J. Invest. Dermatol. *88*, 769–773.

161. Ishihara, M., Arai, T., Sato, S., Morimoto, Y., Obara, M., and Kikuchi, M. (2001). Temperature measurement for energy-efficient ablation by thermal radiation with a microsecond time constant from the corneal surface during ArF excimer laser ablation. Front. Med. Biol. Eng. *11*, 167–175.

162. Ishihara, M., Arai, T., Sato, S., Morimoto, Y., Obara, M., and Kikuchi, M. (2002). Measurement of the surface temperature of the cornea during ArF excimer laser ablation by thermal radiometry with a 15-nanosecond time response. Lasers Surg. Med. *30*, 54–59.

163. Ishihara, M., Sato, M., Sato, S., Arai, T., Obara, M., and Kikuchi, M. (2004). Assessment of expressions of heat shock protein (HSP 72) and apoptosis after ArF excimer laser ablation of the cornea. J. Biomed. Opt. *9*, 187.

164. de Ortueta, D., Magnago, T., Triefenbach, N., Arba Mosquera, S., Sauer, U., and Brunsmann, U. (2012). In vivo measurements of thermal load during ablation in high-speed laser corneal refractive surgery. J. Refract. Surg. *28*, 53–58.

165. Brygo, F., Semerok, A., Oltra, R., Weulersse, J.M., and Fomichev, S. (2006). Laser heating and ablation at high repetition rate in thermal confinement regime. Appl. Surf. Sci. *252*, 8314–8318.

166.   Mrochen, M., Schelling, U., Wuellner, C., and Donitzky, C. (2009). Effect of time sequences in scanning algorithms on the surface temperature during corneal laser surgery with high-repetition-rate excimer laser. J. Cataract Refract. Surg. *35*, 738–746.

167.   Probst, L. (2004). Environmental factors and LASIK. J. Cataract Refract. Surg. *30,* 1817–1818; author reply 1818.

168.   Neuhaus-Richard, I., Frings, A., Ament, F., Görsch, I.C., Druchkiv, V., Katz, T., Linke, S.J., and Richard, G. (2014). Variation in the effectiveness of refractive surgery during the year: results from the Hamburg Weather Study. J. Cataract Refract. Surg. *40*, 1139–1146.

169.   Luger, M.H.A., Ewering, T., and Arba-Mosquera, S. (2014). Analysis of seasonal changes in residual refraction 1-year after corneal laser refractive surgery: a retrospective study. J. Optom. *7*, 138–146.

170.   De Ortueta, D., Magnago, T., and Arba-Mosquera, S. (2015). Thermodynamic measurement after cooling the cornea with intact epithelium and lid manipulation. J. Optom. *8*, 170–173.

171.   Adib-Moghaddam, S., Arba-Mosquera, S., Salmanian, B., Omidvari, A.-H., and Noorizadeh, F. (2014). On-line pachymetry outcome of ablation in aberration free mode TransPRK. Eur. J. Ophthalmol. *24*, 483–489.

172.   De Ortueta, D., Von Rüden, D., Magnago, T., and Mosquera, S.A. (2014). Influence of stromal refractive index and hydration on corneal laser refractive surgery. J. Cataract Refract. Surg. *40*, 897–904.

173.   Aurich, H., Wirbelauer, C., Jaroszewski, J., Hartmann, C., and Pham, D.T. (2006). Continuous measurement of corneal dehydration with online optical coherence pachymetry. Cornea *25,* 182–184.

174. Fisher, B.T., Masiello, K.A., Goldstein, M.H., and Hahn, D.W. (2003). Assessment of transient changes in corneal hydration using confocal Raman spectroscopy. Cornea *22*, 363–370.

175. Dougherty, P.J., Wellish, K.L., and Maloney, R.K. (1994). Excimer laser ablation rate and corneal hydration. Am. J. Ophthalmol. *118*, 169–176.

176. Gottsch, J.D., Rencs, E. V, Cambier, J.L., Hall, D., Azar, D.T., and Stark, W.J. (1996). Excimer laser calibration system. J. Refract. Surg. *12*, 401–411.

177. Anschutz, T., and Pieger, S. (1999). Correlation of laser profilometry scans with clinical results. J. Refract. Surg. *15*, S252-6.

178. Soya, K., Obata, H., Amano, S., Miyata, K., and Tsuru, T. (1995). Effects of blowing or aspiration on ablation rate by excimer laser. Nihon. Ganka Gakkai Zasshi *99*, 1242–1247.

179. Jha, K.N. (2012). High Altitude and the Eye. Asia-Pacific J. Ophthalmol. (Philadelphia, Pa.) *1*, 166–169.

180. Morris, D.S., Somner, J., Donald, M.J., McCormick, I.J.C., Bourne, R.R.A., Huang, S.S., Aspinall, P., and Dhillon, B. (2006). The eye at altitude. Adv. Exp. Med. Biol. *588*, 249–270.

181. Morris, D.S., Somner, J.E.A., Scott, K.M., McCormick, I.J.C., Aspinall, P., and Dhillon, B. (2007). Corneal thickness at high altitude. Cornea *26*, 308–311.

182. Adhikari, S. (2013). Myopia in school children from high mountain region of Nepal. Nepal J. Ophthalmol. *5*, 246–249.

183. Miranda, M.N. (1979). The geographic factor in the onset of presbyopia. Trans. Am. Ophthalmol. Soc. *77*, 603–621.

184. Patyal, S., Arora, A., Yadav, A., and Sharma, V.K. (2017). Corneal Thickness in Highlanders. High Alt. Med. Biol. *18*, 56–60.

185. Argento, C., Valenzuela, G., Huck, H., Cremona, G., Cosentino, M.J., and Gale, M.F. (2001). Smoothness of ablation on acrylic by four different excimer lasers. J. Refract. Surg. *17*, 43–45.

186. Doga, A. V, Shpak, A.A., and Sugrobov, V.A. (2004). Smoothness of ablation on polymethylmethacrylate plates with four scanning excimer lasers. J. Refract. Surg. *20*, S730-3.

187. Vinciguerra, P., Azzolini, M., Radice, P., Sborgia, M., and De Molfetta, V. (1998). A method for examining surface and interface irregularities after photorefractive keratectomy and laser in situ keratomileusis: predictor of optical and functional outcomes. J. Refract. Surg. *14*, S204-6.

188. Walker, M.B., and Wilson, S.E. (2001). Recovery of uncorrected visual acuity after laser in situ keratomileusis or photorefractive keratectomy for low myopia. Cornea *20*, 153–155.

189. Hersh, P.S., Brint, S.F., Maloney, R.K., Durrie, D.S., Gordon, M., Michelson, M.A., Thompson, V.M., Berkeley, R.B., Schein, O.D., and Steinert, R.F. (1998). Photorefractive keratectomy versus laser in situ keratomileusis for moderate to high myopia. A randomized prospective study. Ophthalmology *105*, 1512–1522, discussion 1522-3.

190. Vinciguerra, P., Azzolini, M., Airaghi, P., Radice, P., and De Molfetta, V. (1998). Effect of decreasing surface and interface irregularities after photorefractive keratectomy and laser in situ keratomileusis on optical and functional outcomes. J. Refract. Surg. *14*, S199-203.

191. Pérez-Merino, P., Martinez-Garcia, M.C., Mar-Sardaña, S., Pérez-Escudero, A., Blanco-Mezquita, T., Mayo-Iscar, A., and Merayo-Lloves, J.

(2010). Corneal light transmission and roughness after refractive surgery. Optom. Vis. Sci. *87*.

192. Perez-Merino, P., Martinez-Garcia, C., Mar-Sardaña, S., Perez-Escudero, A., Merayo-Lloves, J., Blanco-Mezquita, T., Garrido-Calvo, E. (2008). Relationship Between the Roughness of Corneal Epithelium and the Transmission of Light. Invest. Ophthalmol. Vis. Sci. *49*(13):3910.

193. Liang, F.Q., Geasey, S.D., Cerro, M. del, and Aquavella, J. V (1992). A New Procedure for Evaluating Smoothness of Corneal Surface Following 193-Nanometer Excimer Laser Ablation. J. Refract. Surg. *8*, 459–465.

194. Hauge, E., Naroo, S.A., and Charman, W.N. (2001). Poly(methyl methacrylate) model study of optical surface quality after excimer laser photorefractive keratectomy. J. Cataract Refract. Surg. *27*, 2026–2035.

195. Fantes, F.E., and Waring, G.O. (1989). Effect of excimer laser radiant exposure on uniformity of ablated corneal surface. Lasers Surg. Med. *9*, 533–542.

196. Naroo, S.A., and Charman, W.N. (2005). Surface Roughness After Excimer Laser Ablation Using a PMMA Model: Profilometry and Effects on Vision. J. Refract. Surg. *21*, 260–268.

197. McCafferty, S.J., Schwiegerling, J.T., and Enikov, E.T. (2012). Corneal surface asphericity, roughness, and transverse contraction after uniform scanning excimer laser ablation. Invest. Ophthalmol. Vis. Sci. *53*, 1296–1305.

198. Arba Mosquera, S., de Ortueta, D., and Verma, S. (2018). The art of nomograms. Eye Vis. *5*.

199. Feltham, M.H., and Wolfe, R.J. (2000). Some variables to consider to avoid the need for LASIK surgical enhancements. Clin. Exp. Optom. *83*, 76–81.

200.   Moniz, N., and Fernandes, S.T. (2002). Nomogram for treatment of astigmatism with laser in situ keratomileusis. J. Refract. Surg. *18*, S323-6.

201.   Alpins, N.A., and Goggin, M. (2004). Practical astigmatism analysis for refractive outcomes in cataract and refractive surgery. Surv. Ophthalmol. *49*, 109–122.

202.   Gailitis, R.P. (2005). Comparison of LASIK outcomes with the Alcon LADARVision4000 and the VISX STAR S2 excimer lasers using optimized nomograms. J. Refract. Surg. *21*, 683–690.

203.   Arnalich-Montiel, F., Wilson, C.M., Morton, S.J., and Allan, B.D. (2009). Back-calculation to model strategies for pretreatment adjustment of the ablation sphere in myopic wavefront laser in situ keratomileusis. J. Cataract Refract. Surg. *35*, 1174–1180.

204.   Verma, S., Hesser, J., and Arba-Mosquera, S. (2019). Cross sectional analysis of Impact of seasonal changes on Excimer Laser Ablation performance on PMMA. (Being prepared for submission- see annexure)

205.   Verma, S., Kehrer, T., Hesser, J., and Arba-Mosquera, S. (2019). Analysis of Impact of Humidity and Temperature on Excimer Laser Ablation of polyethylene terephthalate, PMMA and Porcine Corneal Tissue. (Under review in Lasers Surg Med. - See annexure)

206.   Verma, S., Hesser, J., and Arba-Mosquera, S. (2017). Method for assessing the impact of residual roughness after corneal ablation in perception and vision. Acta Ophthalmol. *95*.

207.   Verma, S., Hesser, J., and Mosquera, S.A. (2018). Method for assessing the impact of residual roughness after corneal ablation in polychromatic vision. Invest Ophthalmol Vis Sci*, 59*, 5806-5806.

208.   Verma, S., Hesser, J., and Arba-Mosquera, S. (2017). Optimum Laser
Beam Characteristics for Achieving Smoother Ablations in Laser Vision
Correction. Invest. Ophthalmol. Vis. Sci. *58*, 2021–2037.

209.   Arba-Mosquera, S., and Verma, S. (2016). Optimum laser beam
characteristics for achieving smoother ablations in laser based vision
correction. Invest. Ophthalmol. Vis. Sci *57* (12), 4866-4866

210.   Verma, S., Hesser, J., and Arba-Mosquera, S. (2017). Optimum Laser
Beam Characteristics for Achieving Smoother Ablations in Laser Vision
Correction. Invest. Ophthalmol. Vis. Sci. *58*, 2021–2037.

211.   Verma, S., Hesser, J., and Arba-Mosquera, S. (2019). Effect of LASER
Beam Truncation (Pinhole), (Ordered) Dithering, and Jitter on residual
smoothness after PMMA ablations, using a close-to-Gaussian beam profile.
(Being prepared for submission- see annexure)

212.   Brunsmann, U., Sauer, U., Dressler, K., Triefenbach, N., and Mosquera,
S.A. (2010). Minimisation of the thermal load of the ablation in high-speed
laser corneal refractive surgeryThe "intelligent thermal effect control" of the
AMARIS platform. J. Mod. Opt. *57*, 466–479.

213.   Arba-mosquera, S., Triefenbach, N. (2010). Method for setting
calibration data to control unit of laser ablation device, involves deriving new
calibration data, and automatically storing new calibration data for control unit
in laser ablation device. DE102009016008.

214.   Howarth, P.A., Zhang, X.X., Bradley, A., Still, D.L., and Thibos, L.N.
(1988). Does the chromatic aberration of the eye vary with age? J. Opt. Soc.
Am. A. *5*, 2087–2092.

215.   Salmon, T.O., West, R.W., Gasser, W., and Kenmore, T. (2003). Measurement of refractive errors in young myopes using the COAS Shack-Hartmann aberrometer. Optom. Vis. Sci. *80*, 6–14.

216.   Thibos, L.N., Hong, X., Bradley, A., and Applegate, R.A. (2004). Accuracy and precision of objective refraction from wavefront aberrations. J. Vis. *4*, 329–351.

217.   Dorronsoro, C., Siegel, J., Remon, L., and Marcos, S. (2008). Suitability of Filofocon A and PMMA for experimental models in excimer laser ablation refractive surgery. Opt. Express *16*, 20955–20967.

218.   Bayer, B.E. (1973). An optimum method for two-level rendition of continuous-tone pictures.

219.   Herald Community Newspapers. (2019). *Lynbrook eye doctor recalls conducting first laser surgery*. [online] Available at: http://liherald.com/stories/30-years-later-lynbrook-eye-doctor-recalls-first-laser-surgery,101790 [Accessed 15 Jan. 2019].

220.   Kohnen, T. (2012). Effects of refractive surgery in extreme altitude or space. J. Cataract Refract. Surg. *38*, 1307–1308.

221.   Aaron, M., Wright, S., Gooch, J., Harvey, R., Davis, R., and Reilly, C. (2012). Stability of laser-assisted in situ keratomileusis (LASIK) at altitude. Aviat. Sp. Environ. Med. *83*, 958–961.

222.   Yaşar, T., and Ylmaz, Ö.F. (2001). The refractive changes and long-term (3 years) results of radial keratotomy performed at high altitude. Jpn. J. Ophthalmol. *45*, 156–159.

223.   Dantas, P.E.C., Martins, C.L., de Souza, L.B., and Dantas, M.C.N. (2007). Do environmental factors influence excimer laser pulse fluence and efficacy? J. Refract. Surg. *23*, 307–309.

224.　Seider, M.I., McLeod, S.D., Porco, T.C., and Schallhorn, S.C. (2013). The effect of procedure room temperature and humidity on LASIK outcomes. Ophthalmology *120*, 2204–2208.

225.　Walter, K.A., and Stevenson, A.W. (2004). Effect of environmental factors on myopic LASIK enhancement rates. J. Cataract Refract. Surg. *30*, 798–803.

226.　Kim, W.S., and Jo, J.M. (2001). Corneal hydration affects ablation during laser in situ keratomileusis surgery. Cornea *20*, 394–397.

227.　Chatterjee, A., and Shah, S. (1997). Seasonal variations in refractive results following excimer laser photorefractive keratectomy. J. Refract. Surg. *13*, S447-9.

228.　Schena, E., Silvestri, S., Franzesi, G.T., Cupo, G., Carito, P., and Ghinelli, E. (2006). Theoretical model and design of a device to reduce the influence of environmental factors on refractive surgery outcomes. In Annual International Conference of the IEEE Engineering in Medicine and Biology - Proceedings, pp. 343–346.

229.　Souza, I.R.U. de, Souza, A.P. de Q.U. de, Souza, A.P. de Q.U. de, Figueiredo, P., Jesus, R.S., and Kara-José, N. (2001). Influence of Temperature and Humidity on Laser in situ Keratomileusis Outcomes. J. Refract. Surg. *17*, S202–S204.

230.　Lee, H., Yong Kang, D.S., Reinstein, D.Z., Arba-Mosquera, S., Kim, E.K., Seo, K.Y., and Kim, T.-I. (2018). Comparing corneal higher-order aberrations in corneal wavefront-guided transepithelial photorefractive keratectomy versus small-incision lenticule extraction. J. Cataract Refract. Surg. *44*, 725–733.

231.   Arines, J., Almaguer, C., and Acosta, E. (2017). Potential use of cubic

phase masks for extending the range of clear vision in presbyopes: initial

calculation and simulation studies. Ophthalmic Physiol. Opt. *37*, 141–150.

232.   Águila-Carrasco, A.J. Del, Read, S.A., Montés-Micó, R., and Iskander,

D.R. (2017). The effect of aberrations on objectively assessed image quality

and depth of focus. J. Vis. *17*, 2.

233.   Young, L.K., Love, G.D., and Smithson, H.E. (2013). Accounting for the

phase, spatial frequency and orientation demands of the task improves

metrics based on the visual Strehl ratio. Vision Res. *90*, 57–67.

234.   Csoitalia.it. (2019). [online] Available at:

http://www.csoitalia.it/app/public/files/prodotto/Osiris_ENG_LD.pdf [Accessed

25 Jan. 2019].

235.   Zhao, P.-F., Li, S.-M., Lu, J., Song, H.-M., Zhang, J., Zhou, Y.-H., and

Wang, N.-L. (2017). Effects of higher-order aberrations on contrast sensitivity

in normal eyes of a large myopic population. Int. J. Ophthalmol. *10*, 1407–

1411.

236.   Domínguez-Vicent, A., Pérez-Vives, C., Ferrer-Blasco, T., García-

Lázaro, S., and Montés-Micó, R. (2013). The effect of simulated normal and

amblyopic higher-order aberrations on visual performance. J. AAPOS *17*,

269–275.

237.   Shetty, N., Kochar, S., Paritekar, P., Artal, P., Shetty, R., Nuijts,

R.M.M.A., Webers, C.A.B., and Sinha Roy, A. (2019). Patient-specific

determination of change in ocular spherical aberration to improve near and

intermediate visual acuity of presbyopic eyes. J. Biophotonics *12*,

e201800259.

238.   Mosquera, S.A., and De Ortueta, D. (2011). Correlation among ocular spherical aberration, corneal spherical aberration, and corneal asphericity before and after LASIK for myopic astigmatism with the SCHWIND amaris platform. J. Refract. Surg. *27*, 434–443.

239.   Lohmann, C.P., and Güell, J.L. (1998). Regression after LASIK for the treatment of myopia: the role of the corneal epithelium. Semin. Ophthalmol. *13*, 79–82.

240.   Moilanen, J.A.O., Holopainen, J.M., Vesaluoma, M.H., and Tervo, T.M.T. (2008). Corneal recovery after lasik for high myopia: a 2-year prospective confocal microscopic study. Br. J. Ophthalmol. *92*, 1397–1402.

241.   Kanellopoulos, A.J., and Asimellis, G. (2014). Longitudinal postoperative lasik epithelial thickness profile changes in correlation with degree of myopia correction. J. Refract. Surg. *30*, 166–171.

242.   Reinstein, D.Z., Archer, T.J., and Gobbe, M. (2014). Rate of change of curvature of the corneal stromal surface drives epithelial compensatory changes and remodeling. J. Refract. Surg. *30*, 799–802.

243.   Vinciguerra, P., Azzolini, C., and Vinciguerra, R. (2015). Corneal curvature gradient determines corneal healing process and epithelial behavior. J. Refract. Surg. *31*, 281–282.

244.   Vinciguerra, P., Roberts, C.J., Albé, E., Romano, M.R., Mahmoud, A., Trazza, S., and Vinciguerra, R. (2014). Corneal curvature gradient map: a new corneal topography map to predict the corneal healing process. J. Refract. Surg. *30*, 202–207.

245.   Kwon, Y., Choi, M., and Bott, S. (2008). Impact of ablation efficiency reduction on post-surgery corneal asphericity: simulation of the laser refractive surgery with a flying spot laser beam. Opt. Express *16*, 11808–11821.

246.   Dorronsoro, C., Remon, L., Merayo-Lloves, J., and Marcos, S. (2009). Experimental evaluation of optimized ablation patterns for laser refractive surgery. Opt. Express *17*, 15292.

247.   Dyer, P.E., Walton, C.D., and Akeel, K.A. (2005). Coherence effects in surface roughness induced by vacuum ultraviolet F2 laser ablation. Opt. Lett. *30*, 1336–1338.

248.   Marcos, S., Dorronsoro, C., Cano, D. (2005). Spherical aberration prevention method in e.g. laser refractive surgery system. Patent WO 2005/122873 A1.

249.   Dorronsoro, C., Cano, D., Merayo-Lloves, J., and Marcos, S. (2006). Experiments on PMMA models to predict the impact of corneal refractive surgery on corneal shape. Opt. Express *14*, 6142–6156.

250.   Hafiz, A.M.K., Bordatchev, E. V., and Tutunea-Fatan, R.O. (2012). Influence of overlap between the laser beam tracks on surface quality in laser polishing of AISI H13 tool steel. In Journal of Manufacturing Processes, pp. 425–434.

251.   Gardner, A.K., Staninec, M., and Fried, D. (2005). The influence of surface roughness on the bond strength of composite to dental hard tissues after Er:YAG laser irradiation. In Lasers in Dentistry XI, (SPIE), p. 144.

252.   Bende, T., Becker, S., Oltrup, T., Berret, R., Jean, B. (2003). Influence of the Overlap of a 1.0 mm Gaussian Beam Flying Spot Excimer Laser on Surface Roughness. Invest. Ophthalmol. Vis. Sci. *44*(13):2660.

253.   Gauthier, C.A., Holden, B.A., Epstein, D., Tengroth, B., Fagerholm, P., and Hamberg-Nyström, H. (1997). Factors affecting epithelial hyperplasia after photorefractive keratectomy. J. Cataract Refract. Surg. *23*, 1042–1050.

254. Wilson, S.E., Mohan, R.R., Hong, J.W., Lee, J.S., Choi, R., and Mohan, R.R. (2001). The wound healing response after laser in situ keratomileusis and photorefractive keratectomy. Elusive control of biological variability and effect on custom laser vision correction. Arch. Ophthalmol. *119*, 889–896.

255. Qazi, M.A., Roberts, C.J., Mahmoud, A.M., and Pepose, J.S. (2005). Topographic and biomechanical differences between hyperopic and myopic laser in situ keratomileusis. J. Cataract Refract. Surg. *31*, 48–60.

256. Woo, H.M., Kim, M.S., Kweon, O.K., Kim, D.Y., Nam, T.C., and Kim, J.H. (2001). Effects of amniotic membrane on epithelial wound healing and stromal remodelling after excimer laser keratectomy in rabbit cornea. Br. J. Ophthalmol. *85*, 345–349.

257. Mulholland, B., Tuft, S.J., and Khaw, P.T. (2005). Matrix metalloproteinase distribution during early corneal wound healing. Eye (Lond). *19*, 584–588.

258. Dierick, H.G., and Missotten, L. (1992). Is the Corneal Contour Influenced by a Tension in the Superficial Epithelial Cells? A New Hypothesis/Comment: Theo Seller, MD, PhD, Berlin, Germany/Response: Dierick and Missotten. J. Refract. Surg. *8*, 54–60.

259. Tang, M. (2004). *Corneal Mean Curvature Mapping: Application in Laser Refractive Surgery*. Ohio State University.

260. Huang, D., Tang, M., and Shekhar, R. (2003). Mathematical model of corneal surface smoothing after laser refractive surgery. Am. J. Ophthalmol. *135*, 267–278.

261. Lieberman, D.M., and Grierson, J.W. (2000). A mathematical model for laser in situ keratomileusis and photorefractive keratectomy. J. Refract. Surg. *16*, 177–186.

7 ANNEXURE

List of Publications

<u>Before the tenure of this thesis</u>

1) Arba-Mosquera S, Verma S. Analytical optimization of the ablation efficiency at normal and non-normal incidence for generic super Gaussian beam profiles. Biomed Opt. Express; 2013; 4: 1422-1433

2) Arba Mosquera S, Verma S. Numerical nonwavefront-guided algorithm for expansion or recentration of the optical zone. J Biomed Opt. 2014 Aug;19(8):088001. doi: 10.1117/1.JBO.19.8.088001

3) Arba-Mosquera S, Verma S, McAlinden C. Centration axis in refractive surgery. Eye and Vision 2015 2:4

4) Arba Mosquera S, Verma S. Analysis of the change in peak corneal temperature during excimer laser ablation in porcine eyes. J Biomed Opt. 2015 Jul;20(7):78001. doi: 10.1117/1.JBO.20.7.078001

5) Luger MH, McAlinden C, Buckhurst PJ, Wolffsohn JS, Verma S, Arba Mosquera S. Presbyopic LASIK Using Hybrid Bi-Aspheric Micro-Monovision Ablation Profile for Presbyopic Corneal Treatments. Am J Ophthalmol. 2015 Sep;160(3):493-505

6) Arba Mosquera S, Verma S. Effects of torsional movements in refractive procedures. J Cataract Refract Surg 2015; 41:1752–1766

7) Kaluzny BJ, Cieslinska I, Mosquera SA, Verma S. Single-Step Transepithelial PRK vs Alcohol-Assisted PRK in Myopia and Compound Myopic Astigmatism Correction. Medicine (Baltimore). 2016 Feb;95(6):e1993

<u>During the tenure of this thesis (Published)</u>

8) Arba Mosquera S, Verma S. Bilateral symmetry in vision and influence of ocular surgical procedures on binocular vision: A topical review. J Optom. 2016 Oct - Dec;9(4):219-30

9) Arba-Mosquera S, de Ortueta D, Verma S. Minimising residual aberration in the presence of cyclotorsion uncertainty in refractive surgery. J Emmetropia 2016; 3: 139-144

10) SA Mosquera, S Verma. Optimum laser beam characteristics for achieving smoother ablations in laser based vision correction. Investigative Ophthalmology & Visual Science, 2016

11) Verma S, Hesser J, Arba-Mosquera S. Optimum Laser Beam Characteristics for Achieving Smoother Ablations in Laser Vision Correction. Invest Ophthalmol Vis Sci. 2017 Apr 1;58(4):2021-2037

12) S Verma, J Hesser, S Arba-Mosquera. Method for assessing the impact of residual roughness after corneal ablation in perception and vision. Acta Ophthalmologica, 2017

13) Lin DTC, Holland SP, Verma S, Hogden J, Arba-Mosquera S. Postoperative Corneal Asphericity in Low, Moderate, and High Myopic Eyes After Transepithelial PRK Using a New Pulse Allocation. J Refract Surg. 2017;33(12):820-826

14) Arbelaez MC, Alpins N, Verma S, Stamatelatos G, Arbelaez JG, Arba-Mosquera S. Clinical outcomes of laser in situ keratomileusis with an aberration-neutral profile centered on the corneal vertex comparing vector planning with manifest refraction planning for the treatment of myopic astigmatism. J Cataract Refract Surg. 2017 Dec;43(12):1504-1514

15) Arba Mosquera S, de Ortueta D, Verma S. The art of nomograms. Eye and Vision (2018) 5:2 DOI 10.1186/s40662-018-0096-z

16) Arba-Mosquera S, Vinciguerra P, Verma S. Review of technological advancements in calibration systems for laser vision correction. J Biomed Opt. 2018 Feb;23(2):1-8

17) Shady T. Awwad, Sam Arba Mosquera, and Shweetabh Verma. Corneal Wavefront-Guided Ablation. Customized laser vision correction Springer 2018

18) Arba Mosquera S, de Ortueta D, Verma S. Corneal functional optical zone under monocular and binocular assessment. Eye Vis (Lond). 2018 Feb 7;5:3.

19) McNeely RN, Moutari S, Arba-Mosquera S, Verma S, Moore JE. An alternative application of Rasch analysis to assess data from ophthalmic patient-reported outcome instruments. PLoS One. 2018 Jun 21;13(6):e0197503. doi: 10.1371/journal.pone.0197503. eCollection 2018.

20) de Ortueta D, von Rüden D, Verma S, Magnago T, Arba-Mosquera S. Transepithelial Photorefractive Keratectomy in Moderate to High

Astigmatism With a Non-wavefront–Guided Aberration-Neutral Ablation Profile. Journal of Refractive Surgery2018;34(7):466-474

21) S Verma, J Hesser, SA Mosquera. Method for assessing the impact of residual roughness after corneal ablation in polychromatic vision. Investigative Ophthalmology & Visual Science, 2018

22) Kaluzny BJ, Piotrowiak-Slupska I, Kaszuba-Modrzejewska M, Stachura J, Arba-Mosquera S, Verma S. Three-year outcomes after high hyperopia correction using photorefractive keratectomy with a large ablation zone. Br J Ophthalmol. 2018 Aug 9. pii: bjophthalmol-2017-311694. doi: 10.1136/bjophthalmol-2017-311694.

23) Taneri S, Kiessler S, Rost A, Verma S, Arba-Mosquera S, Dick HB. Varifocal Versus Monofocal LASIK in Presbyopic Hyperopic Eyes. J Refract Surg. 2019 Jul 1;35(7):459-466. doi: 10.3928/1081597X-20190528-01.

<u>During the tenure of this thesis (Accepted for publication)</u>

24) Immediate and short term visual recovery after SmartSurf[ACE] photorefractive keratectomy
(Journal of Optometry: https://doi.org/10.1016/j.optom.2019.04.003)

<u>During the tenure of this thesis (Under review)</u>

25) Immediate visual recovery after SmartSurf[ACE] compared to standard transepithelial photorefractive keratectomy

26) Long-term outcomes after LASIK using hybrid bi-aspheric micro-monovision ablation profile for the surgical compensation of presbyopia: 6-year results.

27) Analysis of Impact of Humidity and Temperature on Excimer Laser Ablation of polyethylene terephthalate, PMMA and Porcine Corneal Tissue

28) Effect of LASER Beam Truncation (Pinhole), (Ordered) Dithering, and Jitter on residual smoothness after PMMA ablations, using a close-to-Gaussian beam profile

During the tenure of this thesis (Being prepared for submission)

29) Theoretical Effect of Coma and Spherical Aberrations Translation on Refractive Error and Higher Order Aberrations

30) Analysis of the impact of the gain of ablation efficiency due to hydration changes during cornea refractive surgery

31) Two-Years Follow-up for LASIK on Moderate to High Astigmatism with a Non-Wavefront-Guided Aberration-Free Ablation Profile

32) Comparison of the theoretical impact of decentration and cyclotorsion on residual aberrations in refractive surgery

33) Cross sectional analysis of Impact of seasonal changes on Excimer Laser Ablation performance on PMMA

8   CURRICULUM VITAE

Name	Shwetabh Verma
Address	Badergasse 16 63739 Aschaffenburg Germany
Telephone	0049 / 176 / 2483 6882
E-mail	Shwetabh.verma@yahoo.com
Birthday/place	19.01.1988 in Delhi, India
Nationality	Indian
Residency	Germany
Marital Status	Married

Professional Experience

10/2012 to current	R&D Project Manager & Biomedical engineer at SCHWIND eye-tech-solutions GmbH Kleinostheim, Germany
9/2009 to 7/2010	Servicing and sales engineer for medical devices at S.M. Health Care Products Pvt. Ltd. Delhi, India

Current responsibilities	Research and develop innovative mathematical models and algorithms for new hardware and software products
	In synergy with a team of engineers, develop new software modules based on novel algorithms
	Statistical analysis and support in clinical researches and trials
	Hardware development
	Generate new ideas and bring innovations
	Mathematical modeling
	Scientific writing
	Representing the company in research congresses (disseminate company research and collect new ideas)
	Test planning for new products and components
	Clinically testing new products and components
	Scientific data analysis
	Documentation of scientific results
	Development of nomograms in refractive surgery
	Manage small teams of specialists for clinical/laboratory testing and research
	R&D Project Management (Activity and resource planning, Organizing and motivating a project team, Controlling time management, Cost estimating and developing the budget, Analyzing and managing project risk, Monitoring progress, Managing reports and necessary documentation)

Education/Dissertation/ Research /Projects	
11/2016 to current	**Doctoral research in Medical Physics** Mannheimer Institut für Intelligente Systeme in der Medizin (MIISM) der Medizinischen Fakultät Mannheim Ruprecht-Karls-Universität Heidelberg
08/2010 to 08/2012	**Master of Science in Biomedical Engineering** Specialization in Biomedical Optics from Ruprecht-Karls-Universität Heidelberg, Medizinische Fakultät Mannheim , Germany (Gut)
08/2012	**Dissertation** Two Photon microscope technique to develop a same day procedure to diagnose Keratitis infection
03/2012 to 06/2012	**Lab project at Laser Lab, Universitätsmedizin Mannheim, Germany** Optical lab technique for Single Photon Microscopy to image the retina in porcine eyes
11/2011 to 02/2012	**Lab project at Laser Lab, Universitätsmedizin Mannheim, Germany** Study of Two Photon and Confocal Microscopy on Trabecular Meshwork with safety limits analysis in porcine eyes
03/2011 to 08/2012	**Master thesis at Shiley eye center, University of California, San Diego** Two Photon Microscopy technique to develop a same day procedure to diagnose Keratitis infection.
08/2005 to 08/2009	**Bachelor of Technology in Electronics and Communication Engineering** From Punjab Technical University, India (First class with distinction)
Till 03/2005	**Central Board of Secondary Education, India** From D.A.V Public School, Delhi, India (Merit)
Publications	
2013 – Current	Please refer to my Google Scholar link
Research talks and posters	
2018	Method for assessing the impact of residual roughness after corneal ablation in polychromatic vision at The Association for Research in Vision and Ophthalmology
2017	Method for assessing the impact of residual roughness after corneal ablation in perception and vision at European Association for Vision and Eye Research Conference
2015	Impact of Cyclotorsion movements in refractive surgery at Wavefront & Presbyopic Refractive Corrections Congress
2015	Analytical optimization of the ablation efficiency at normal and non-normal incidence for generic truncated super Gaussian beam profiles at European Optical Society Conference

2012	Two-Photon Imaging of the Trabecular Meshwork on mechanisms of selective Trabeculoplasty surgery at The Association for Research in Vision and Ophthalmology
Skills	Thinking differently Innovation Open mindedness and adaptability MATLAB/SCILAB/PYTHON Mathematical modeling Research of mathematical and physical models Clinical and laboratory research Vision sciences Statistical data analysis Laser/Medical physics Basic and adaptive optics C++ Zemax Computer Aided Design Labview Image J Microscopy Microsoft office Quality Management Project Management
Trainings	
2015	AMARIS advanced service training, SCHWIND eye-tech-solutions GmbH & Co. KG
2015	Advanced application training for SCHWIND refractive package, SCHWIND eye-tech-solutions GmbH & Co. KG
2012	AMARIS basic service training, SCHWIND eye-tech-solutions GmbH & Co. KG
2012	Basic application training for SCHWIND refractive package, SCHWIND eye-tech-solutions GmbH & Co. KG
2010	International workshop on Basic & Advanced Techniques of PCNL, Delhi, India
2010	Image Guided and Robotic Radiotherapy, Medical University Mannheim, Germany
Research scholarships and awards	
Doctoral Research, 11/2016 to current	Research partly funded by the "Zentrales Innovationsprogramm Mittelstand (ZIM)" (Förderkennzeichen: ZF4340402AK7)
Master thesis, 03/2011 to 08/2012	Technical and financial support awarded by Heidelberg Engineering GmbH, Germany
Languages	English (Native, TOEFL 109, GRE 1320) German (B1) Hindi (Native) Punjabi (Native)

Passport and Visas	Nationality – Indian Permanent right to residency-Germany Long term business visa-USA
References	Upon request
Personal interests	Travel, cooking, hiking, sports, literature, music

9   ACKNOWLEDGEMENTS

Shwetabh Verma
October' 2019